UNIVERSITY OF CALIFORNIA, SAN DIEGO

Understanding the Role of Organic Aerosol in the Coastal and Remote Pacific Marine Boundary Layer

A dissertation submitted in partial satisfaction of the
requirements for the degree
Doctor of Philosophy

in

Oceanography

by

Lelia Nahid Hawkins

Committee in charge:

> Professor Lynn M. Russell, Chair
> Professor Jan Kleissl
> Professor Joel Norris
> Professor Kimberly Prather
> Professor Mark Thiemens

2010

UMI Number: 3403095

UMI®

Dissertation Publishing

ProQuest®

The dissertation of Lelia Nahid Hawkins is approved, and it is acceptable in quality and form for publication on microfilm and electronically:

_____

_____

_____

_____

_____
Chair

University of California, San Diego

2010

DEDICATION

This doctoral dissertation is dedicated to my parents, Jan and Hashem, for their unwavering support during the long process of my education. It is also dedicated to my husband, Blaise, who endured many missed vacations and many working weekends without any complaints or regrets. This degree would not have been possible without your support and therefore belongs, in part, to you.

EPIGRAPH

"I say!" murmured Horton. "I've never heard tell
Of a small speck of dust that is able to yell.
So you know what I think?Why, I think that there must
Be someone on top of that small speck of dust!
Some sort of a creature of very small size,
too small to be seen by an elephants eyes"

—From *Horton Hears A Who* by Dr. Seuss

TABLE OF CONTENTS

xiii

LIST OF TABLES

ACKNOWLEDGEMENTS

VITA

2005	B. S. in Chemistry *cum laude*, University of California, San Diego
2005	B. S. in Environmental Systems *cum laude*, University of California, San Diego
2007-2008	Graduate Teaching Assistant, University of California, San Diego
2010	Ph. D. in Oceanography, University of California, San Diego

PUBLICATIONS

Hawkins, L. N., L. M. Russell, C. H. Twohy, and J. R. Anderson (2008), Uniform particle-droplet partitioning of 18 organic and elemental components measured in and below DYCOMS-II stratocumulus clouds, Journal of Geophysical Research, 113, D14201, doi:10.1029/2007JD009150.

Russell, L. M., S. Takahama, S. Liu, L. N. Hawkins, D. S. Covert, P. K. Quinn, and T. S. Bates (2009), Oxygenated fraction and mass of organic aerosol from direct emission and atmospheric processing measured on the R/V Ronald Brown during TEXAQS/ GoMACCS 2006, Journal of Geophysical Research, 114, doi:10.1029/2008JD011275.

Russell, L. M. and Bahadur, R. and Hawkins, L. N. and Allan, J. and Baumgardner, D. and Quinn, P. K. and Bates, T. S. (2009), Organic aerosol characterization by complementary measurements of chemical bonds and molecular fragments, Atmospheric Environment, 43, 6100-6105.

Hawkins, L. N., L.M. Russell, D. S. Covert, P. K. Quinn, and T. S. Bates (2010), Carboxylic acids, sulfates, and organosulfates in processed continental organic aerosol over the southeast Pacific ocean during VOCALS-REx 2008, Journal of Geophysical Research, doi:10.1029/2009JD013276, *in press.*

Russell, L. M., Hawkins, L. N., Frossard, A. A., Quinn, P. K., Bates, T. S. (2010), Carbohydrate-Like Composition of Submicron Atmospheric Particles and their Production from Ocean Bubble Bursting, Proceedings of the National Academy of Sciences, doi:10.1073/pnas.0908905107, *in press.*

Hawkins, L. N. and Russell, L. M. (2010), Oxidation of ketone groups in transported biomass burning aerosol from the 2008 Northern California Lightning Series fires, *submitted.*

Hawkins, L. N. and Russell, L. M. (2010), Polysaccharides, Proteins, and Phytoplankton Fragments: Four Chemically Distinct Types of Marine Primary Organic Aerosol Classified by Single Particle Spectromicroscopy, *submitted.*

ABSTRACT OF THE DISSERTATION

**Understanding the Role of Organic Aerosol in the Coastal and Remote
Pacific Marine Boundary Layer**

by

Lelia Nahid Hawkins

Doctor of Philosophy in Oceanography

University of California, San Diego, 2010

Professor Lynn M. Russell, Chair

Atmospheric aerosol particles were collected over three field experiments in
the remote and coastal marine boundary layer of the eastern Pacific Ocean from
aircraft, ship, and stationary platforms and were analyzed using Fourier Trans-
form Infrared (FTIR) spectroscopy, Aerosol Mass Spectrometry (AMS), and Scan-
ning Transmission X-ray Microscopy with Near-Edge Absorption Fine Structure
(STXM-NEXAFS) for organic functional groups and organic mass fragments. X-
ray fluorescence (XRF) and Scanning Electron Microscopy with Energy Dispersive
X-rays (SEM-EDX) analyses were used to investigate the elemental composition
of the analyzed particles. The aim of these studies was to better characterize par-
ticle sources and composition in the stratocumulus-topped marine boundary layer
(MBL), where aerosol-cloud interactions play an important role in controlling the
reflectivity of the large cloud decks. Particle composition was linked to distinct
particle sources including primary marine emissions, biomass burning, and fossil
fuel combustion. Fossil fuel combustion particles were characterized by large con-
tributions from saturated alkane and carboxylic acid groups. Biomass burning

aerosol particles were characterized as mixtures of alkane, carboxylic acid, and ketone groups, consistent with biogenic secondary organic aerosol particles observed in chamber studies. Photochemical aging of the transported smoke particles was observed on diurnal and multi-day timescales as an increase in the relative amount of oxygenated groups and oxygen-containing molecular fragments. Marine primary organic aerosol (POA) particles were observed in shipboard samples and were characterized by large contributions from organic hydroxyl groups, suggesting a carbohydrate-containing source in the ocean surface emitted during bubble bursting. Marine particles were also identified in single particle STXM-NEXAFS and were classified into four distinct categories including soluble and insoluble polysaccharides, proteins, and calcareous phytoplankton fragments. The presence of oxidized (polar) organic components–ketone, organic hydroxyl, and carboxylic acid groups–in submicron particles suggests that many of the measured particles could contribute to cloud condensation nuclei number concentration and mass in both open ocean and coastal regions. Together, these measurements show that marine POA provides a significant contribution to submicron particle mass in the clean MBL, whereas fossil fuel combustion and biomass burning emissions contribute the majority of the organic mass in coastal regions.

Introduction

Atmospheric aerosol is a suspension of liquid and solid particles in air, originating either as intact particles (primary) or as semi-volatile compounds that later condense to form particles (secondary), which are emitted from both natural and anthropogenic sources. A recent summary of non-refractory submicron particles from the Northern Hemisphere mid-latitudes has shown that anywhere between 18% and 70% of particle mass can be attributed to organic components (Zhang et al., 2007). Natural sources of organic aerosol include wave breaking (Blanchard, 1964) and condensation of biogenic volatile organic compounds (BVOCs) emitted from terrestrial and marine plants (Calogirou et al., 1999). Anthropogenic primary and secondary organic particle sources overlap significantly and include fossil fuel combustion, industrial operations, and meat cooking. Biomass burning is an extremely important source of atmospheric organic particles, responsible for emitting 31-45 Tg C yr^{-1} (Bond et al., 2004), but includes naturally occurring wildfires and prescribed burns for land clearing; therefore, it is not attributed strictly to natural or anthropogenic actions.

Particles from these sources interact with incoming solar radiation directly, by absorption and scattering, and indirectly, as cloud condensation nuclei (CCN) resulting in either net warming or cooling depending on particle composition, size, and location within Earth's atmosphere. Currently, the indirect effect of aerosol particles on cloud radiative properties (e.g. albedo) is the largest source of uncertainty in understanding the Earth's natural and anthropogenic radiative forcing and predicting its future trends (IPCC, 2007). The first indirect effect, described in Twomey (1974), is the increase in cloud droplet number concentration and decrease in cloud droplet size–driven by increased CCN concentration–resulting in

increased cloud albedo. Some of this uncertainty may result from the fact that organic compounds compose a significant fraction of atmospheric particulate mass (Kanakidou et al., 2005; Zhang et al., 2007) and that many of these compounds are unknown. Observed organic functional groups include non-polar (e.g. saturated aliphatic or alkane) and polar (e.g. carboxylic acid) components as well as those falling somewhere in between (e.g. organic hydroxyl and ketone groups) (Maria et al., 2002, 2003; Russell et al., 2009; Gilardoni et al., 2007; Hawkins et al., 2010) in varying proportions. These organic components can reduce or increase CCN concentrations by lowering solubility, increasing molecular weight, and suppressing surface tension (Ervens et al., 2005; Chan et al., 2008). During particle formation and subsequent atmospheric processing, individual organic particles often become mixtures of components from multiple organic and inorganic sources. This mixing contributes an added layer of complexity to predicting CCN concentrations from organic aerosol composition, since even small amounts of soluble material can drastically alter the CCN activity of organic particles (Roberts et al., 2002). For low supersaturations, when composition varies with size, or when particles are small, both particle size and composition are relevant to determining whether or not particles will be CCN active (Nenes et al., 2002; Roberts et al., 2002). The effect of aerosol particles on cloud albedo (Twomey, 1974, 1977; Charlson et al., 1992; Durkee et al., 2000; Twohy et al., 2005) means that changes to the global particle population may have strong local and global effects on the Earth's radiative balance.

Recently, more attention has been directed towards the indirect effect of aerosol particles on marine stratocumulus clouds, in particular, because of their large spatial coverage, sensitivity of cloud droplet number to CCN concentrations, and large, negative radiative forcing (Stevens et al., 2003; Bretherton et al., 2004; Twohy et al., 2005; Huneeus et al., 2006; Brioude et al., 2009). Two expansive, persistent marine stratocumulus cloud decks are found in the eastern Pacific Ocean, one off the California coast and one off the Chilean coast. Both regions are characterized by strong upwelling of cold, nutrient rich water driven by equatorward coastal currents. Coastal sites are especially relevant for marine aerosol generation

because of increased wave action (de Leeuw et al., 2000; Flanagan et al., 2006; Sellegri et al., 2005; Clarke et al., 2006) and elevated concentrations of surface organics in upwelling zones. In addition, some coastal sites offer the opportunity to measure anthropogenic and natural, terrestrial particle production and their effect on background particle concentrations and composition.

In coastal environments, continental outflow of biogenic and anthropogenic organic particles can alter the number and composition of particles, making conditions less like the typical clean, background MBL (particle concentration < 300 cm^{-3}) and more like a rural, continental atmosphere (> 500 cm^{-3}) (Hegg et al., 2008; Brioude et al., 2009; Hawkins et al., 2010; Hawkins and Russell, 2010). In remote marine locations, CCN concentrations are controlled by natural marine aerosol particles whose production includes primary and secondary mechanisms. Primary marine aerosol particles are generated by wave action. Bubble bursting produces submicron sea salt and organic particles (O'Dowd and de Leeuw, 2007; Facchini et al., 2008; Russell et al., 2010). Although the mechanism of primary submicron sea salt aerosol formation is well-studied, much of the recent work has been focused on characterizing the non-salt composition, specifically the amount and speciation of organic compounds, in various marine atmospheres (Pósfai et al., 1995; Middlebrook et al., 1998; Mochida et al., 2002; Maria et al., 2002; Cavalli et al., 2004; Quinn et al., 2006; Facchini et al., 2008; Russell et al., 2010).

To investigate the composition and sources of organic aerosol to the stratocumulus-topped MBL, measurements of atmospheric aerosol were collected over three field campaigns. Aircraft-based measurements of cloud interstitial aerosol and cloud droplet residual particles provided chemically-resolved scavenging coefficients for organic and inorganic components. Stationary coastal measurements of fossil fuel combustion and biomass burning emissions provided key compositional differences between these two, dominant sources of organic aerosol and their susceptibility to photochemical oxidation. Shipboard measurements of coastal and remote marine air masses in the southeastern Pacific provided evidence for anthropogenic alteration of cloud albedo near shore. These measurements are divided into four chapters as 1) a study of the role of aerosol chemical composition on cloud

droplet composition, 2) a study of the contribution of biomass burning particles to oxygenated organic components in a coastal environment, 3) a study of organic particles from natural and anthropogenic sources in the southeastern Pacific coastal and open ocean regions, 4) an exploratory study on the theoretical effect of organic components on CCN concentration at low supersaturations, and 5) an overview of four types of observed primary marine particles from the perspective of single particle measurements of organic components.

References

Blanchard, D., 1964. Sea-to-Air Transport of Surface Active Material. Science 146 (3642), 396.

Bond, T. C., Streets, D. G., Yarber, K. F., Nelson, S. M., Woo, J. H., Klimont, Z., 2004. A technology-based global inventory of black and organic carbon emissions from combustion. Journal of Geophysical Research–Atmospheres 109 (D14), 14203–14203.

Bretherton, C. S., Uttal, T., Fairall, C. W., Yuter, S. E., Weller, R. A., Baumgardner, D., Comstock, K., Wood, R., Raga, G. B., 2004. The EPIC 2001 stratocumulus study. Bulletin of the American Meteorological Society 85 (7), 967–977.

Brioude, J., Cooper, O. R., Feingold, G., Trainer, M., Freitas, S. R., Kowal, D., Ayers, J. K., Prins, E., Minnis, P., McKeen, S. A., et al., 2009. Effect of biomass burning on marine stratocumulus clouds off the California coast. Atmospheric Chemistry and Physics 9, 8841–8856.

Calogirou, A., Larsen, B. R., Kotzias, D., 1999. Gas-phase terpene oxidation products: a review. Atmospheric Environment 33 (9), 1423–1439.

Cavalli, F., Facchini, M. C., Decesari, S., Mircea, M., Emblico, L., Fuzzi, S., Ceburnis, D., Yoon, Y. J., ODowd, C. D., Putaud, J. P., et al., 2004. Advances in characterization of size-resolved organic matter in marine aerosol over the North Atlantic. Journal of Geophysical Research 109, 1–14.

Chan, M., Kreidenweis, S., Chan, C., 2008. Measurements of the hygroscopic and deliquescence properties of organic compounds of different solubilities in water and their relationship with cloud condensation nuclei activities. Environ. Sci. Technol 42 (10), 3602–3608.

Charlson, R., Schwartz, S., Hales, J., Cess, R., Coakley Jr, J., Hansen, J., Hofmann, D., 1992. Climate forcing by anthropogenic aerosols. Science 255 (5043), 423–430.

Clarke, A. D., Owens, S. R., Zhou, J., 2006. An ultrafine sea-salt flux from breaking waves: Implications for cloud condensation nuclei in the remote marine atmosphere. J. Geophys. Res 111, 1–2.

de Leeuw, G., Neele, F., Hill, M., Smith, M., Vignati, E., 2000. Production of sea spray aerosol in the surf zone. Journal of Geophysical Research 105, 29.

Durkee, P., Noone, K., Ferek, R., Johnson, D., Taylor, J., Garrett, T., Hobbs, P., Hudson, J., Bretherton, C., Innis, G., et al., 2000. The impact of ship-produced aerosols on the microstructure and albedo of warm marine stratocumulus clouds: A test of MAST hypotheses 1i and 1ii. Journal of the Atmospheric Sciences 57 (16), 2554–2569.

Ervens, B., Feingold, G., Kreidenweis, S. M., 2005. Influence of water-soluble organic carbon on cloud drop number concentration. Journal of Geophysical Research–Atmospheres 110, doi:10.1029/2004JD005634.

Facchini, M. C., Rinaldi, M., Decesari, S., Carbone, C., Finessi, E., Mircea, M., Fuzzi, S., Ceburnis, D., Flanagan, R., Nilsson, E. D., et al., 2008. Primary submicron marine aerosol dominated by insoluble organic colloids and aggregates. Geophysical Research Letters 35 (17), doi:10.1029/2008GL034210.

Flanagan, R., Geever, M., O Dowd, C., 2006. Direct measurements of new-particle fluxes in the coastal environment. Environmental Chemistry 3 (1), 256–259.

Gilardoni, S., Russell, L. M., Sorooshian, A., Flagan, R. C., Seinfeld, J. H., Bates, T. S., Quinn, P. K., Allan, J. D., Williams, B., Goldstein, A. H., et al., 2007. Regional variation of organic functional groups in aerosol particles on four US east coast platforms during the International Consortium for Atmospheric Research on Transport and Transformation 2004 campaign. Journal of Geophysical Research–Atmospheres 112, doi:10.1029/2006JD007737.

Hawkins, L. N., Russell, L. M., 2010. Oxidation of ketone groups in transported biomass burning aerosol from the 2008 Northern California Lightning Series fires. *submitted*.

Hawkins, L. N., Russell, L. M., Covert, D. S., Quinn, P. K., Bates, T. S., 2010. Carboxylic Acids, Sulfates, and Organosulfates in Processed Continental Organic Aerosol over the Southeast Pacific Ocean during VOCALS-REx 2008. Journal of Geophysical Research in press., doi:10.1029/2009JD013276.

Hegg, D. A., Covert, D. S., Jonsson, H. H., 2008. Measurements of size-resolved hygroscopicity in the California coastal zone. Atmospheric Chemistry and Physics 8, 7193–7203.

Huneeus, N., Gallardo, L., Rutllant, J. A., 2006. Offshore transport episodes of anthropogenic sulfur in northern Chile: Potential impact on the stratocumulus cloud deck. Geophysical Research Letters 33 (19), doi:10.1029/2006GL026921.

IPCC, C., 2007. IPCC Fourth Assessment Report (AR4). Geneva, Intergovernmental Panel on Climate Change.

Kanakidou, M., Seinfeld, J. H., Pandis, S. N., Barnes, I., Dentener, F., Facchini, M. C., Van Dingenen, R., Ervens, B., Nenes, A., Nielsen, C. J., et al., 2005. Organic aerosol and global climate modelling: a review. Atmospheric Chemistry and Physics 5 (4), 1053–1123.

Maria, S. F., Russell, L. M., Turpin, B. J., Porcja, R. J., 2002. FTIR measurements of functional groups and organic mass in aerosol samples over the Caribbean. Atmospheric Environment 36 (33), 5185–5196.

Maria, S. F., Russell, L. M., Turpin, B. J., Porcja, R. J., Campos, T. L., Weber, R. J., Huebert, B. J., 2003. Source signatures of carbon monoxide and organic functional groups in Asian Pacific Regional Aerosol Characterization Experiment (ACE-Asia) submicron aerosol types. Journal of Geophysical Research–Atmospheres 108, 8637.

Middlebrook, A. M., Murphy, D. M., Thomson, D. S., 1998. Observations of organic material in individual marine particles at Cape Grim during the First Aerosol Characterization Experiment (ACE 1). Journal of Geophysical Research 103, 16475–16484.

Mochida, M., Kitamori, Y., Kawamura, K., Nojiri, Y., Suzuki, K., 2002. Fatty acids in the marine atmosphere: Factors governing their concentrations and evaluation of organic films on sea-salt particles. Journal of Geophysical Research–Atmospheres 107 (D17), 4325.

Nenes, A., Charlson, R. J., Facchini, M. C., Kulmala, M., Laaksonen, A., Seinfeld, J. H., 2002. Can chemical effects on cloud droplet number rival the first indirect effect? Geophysical Research Letters 29 (17), 29–1.

O'Dowd, C., de Leeuw, G., 2007. Marine aerosol production: a review of the current knowledge. Philosophical Transactions A 365 (1856), 1753.

Pósfai, M., Anderson, J., Buseck, P., Sievering, H., 1995. Compositional variations of sea-salt-mode aerosol particles from the North Atlantic. Journal of Geophysical Research 100, 23–23.

Quinn, P. K., Bates, T. S., Coffman, D., Onasch, T. B., Worsnop, D., Baynard, T., De Gouw, J. A., Goldan, P. D., Kuster, W. C., Williams, E., et al., 2006. Impacts of sources and aging on submicrometer aerosol properties in the marine boundary layer across the Gulf of Maine. Journal of Geophysical Research–Atmospheres 111, doi:10.1029/2006JD007582.

Roberts, G. C., Artaxo, P., Zhou, J., Swietlicki, E., Andreae, M. O., 2002. Sensitivity of CCN spectra on chemical and physical properties of aerosol: A case study from the Amazon Basin. Journal of Geophysical Research 107, 8070.

Russell, L. M., Hawkins, L. N., Frossard, A. A., Quinn, P. K., Bates, T. S., 2010. Carbohydrate-Like Composition of Submicron Atmospheric Particles and their Production from Ocean Bubble Bursting. Proceedings of the National Academy of Sciences, doi:10.1073/pnas.0908905107.

Russell, L. M., Takahama, S., Liu, S., Hawkins, L. N., Covert, D. S., Quinn, P. K., Bates, T. S., 2009. Oxygenated fraction and mass of organic aerosol from direct emission and atmospheric processing measured on the R/V Ronald Brown during TEXAQS/GoMACCS 2006. Journal of Geophysical Research–Atmospheres 114, doi:10.1029/2008JD011275.

Sellegri, K., Yoon, Y., Jennings, S., O Dowd, C., Pirjola, L., Cautenet, S., Chen, H., Hoffmann, T., 2005. Quantification of coastal new ultra-fine particles formation from in situ and chamber measurements during the BIOFLUX campaign. Environmental Chemistry 2 (4), 260.

Stevens, B., Lenschow, D., Vali, G., Gerber, H., Bandy, A., Blomquist, B., Brenguier, J., Bretherton, C., Burnet, F., Campos, T., et al., 2003. Dynamics and chemistry of marine stratocumulus-DYCOMS-II. Bulletin of the American Meteorological Society 84 (5), 579–594.

Twohy, C. H., Petters, M. D., Snider, J. R., Stevens, B., Tahnk, W., Wetzel, M., Russell, L., Burnet, F., 2005. Evaluation of the aerosol indirect effect in marine stratocumulus clouds: Droplet number, size, liquid water path, and radiative impact. Journal of Geophysical Research–Atmospheres 110, doi:10.1029/2004JD005116.

Twomey, S., 1974. Pollution and the planetary albedo. Atmospheric Environment (1967) 8 (12), 1251–1256.

Twomey, S., 1977. The influence of pollution on the shortwave albedo of clouds. Journal of the atmospheric sciences 34 (7), 1149–1152.

Zhang, Q., Jimenez, J. L., Canagaratna, M. R., Allan, J. D., Coe, H., Ulbrich, I., Alfarra, M. R., Takami, A., Middlebrook, A. M., Sun, Y. L., et al., 2007. Ubiquity and dominance of oxygenated species in organic aerosols in anthropogenically-influenced Northern Hemisphere midlatitudes. Geophysical Research Letters 34, doi:10.1029/2007GL029979.

Chapter 1

Uniform particle-droplet partitioning of 18 organic and elemental components measured in and below DYCOMS-II stratocumulus clouds

Abstract. Microphysical and chemical aerosol measurements collected during DYCOMS-II research flights in marine stratocumulus clouds near San Diego in 2001 were used to evaluate the partitioning of 18 organic and elemental components between droplet residuals and unactivated particles. Bulk submicron particle (between 0.2 and 1.3 μm dry diameter) and droplet residual (above 9 μm ambient diameter) filter samples analyzed by Fourier Transform Infrared (FTIR) spectroscopy and X-ray Fluorescence (XRF) were dominated by sea salt, ammonium, sulfate, and organic compounds. For the four nighttime and two daytime flights

studied, the mass concentration of unactivated particles and droplet residuals were correlated ($R^2 > 0.8$) with consistent linear relationships for mass scavenging of all 18 components on each flight, meaning that the measured particle population partitions between droplet residuals and unactivated particles as if the particles contain internal mixtures of the measured components. Scanning electron microscopy (SEM) for flights 3, 5, and 7 support some degree of internal mixing since more than 90% of measured submicron particles larger than 0.26 μm included sea salt-derived components. The observed range of 0.26 to 0.40 of mass scavenging coefficients for the four nighttime flights results from the small variations in temperature profile, updraft velocity, and mixed layer depth among the flights. The uniformity of scavenging coefficients for multiple chemical components is consistent with the aged or processed internal mixtures of sea salt, sulfate, and organic compounds expected at long distances downwind from major particle sources.

1.1 Introduction

Aerosol particles affect the Earth′s radiation budget directly by scattering light and indirectly by changing cloud properties (Charlson et al., 1992). Increasing the number of aerosol particles that act as cloud condensation nuclei (CCN) increases the number concentration and decreases the size of droplets in a cloud (Twomey, 1977). The ability of an aerosol particle to act as a CCN is determined by its composition and size (Hegg et al., 1993; Twohy et al., 2001; Levin et al., 2003; Dusek et al., 2006), although composition and size are not independent and both change with location and season. Organic compounds also contribute to the CCN behavior of particles by adding components of limited solubility and reduced surface tension (Corrigan and Novakov, 1999; Facchini et al., 1999; Ming and Russell, 2004; Kondo et al., 2007; Ervens et al., 2007). Overall the population of aerosol particles may consist of external mixtures of multiple types of pure components, where the components may include sulfate, nitrate, black carbon, dust, semi- and low-volatility organics, fly ash, and sea salt. Individual particles that include multiple components are known as internal mixtures of those components. For internally-mixed particles to imply the same CCN-forming properties in the atmosphere, the internal mixture in each particle must contain the same ratio of soluble to insoluble material (Hansson et al., 1998).

Direct measurements of aerosol particles in a range of locations have shown particle populations with external mixtures of qualitatively different compositions (Pósfai et al., 1995; Anderson et al., 1996; Väkevä et al., 2002; Li et al., 2003; Brock et al., 2004; Cziczo et al., 2004; Twohy et al., 2005a). Many of these studies show clean marine particles externally mixed with combustion products or mineral components when particles from two or more air masses and different source regions are present. Particles that have several similar components mixed together have been frequently observed in marine-influenced environments (Middlebrook et al., 1998; Murphy et al., 1998; O'Dowd et al., 1999; Lee et al., 2002; Sugimoto et al., 2002; Allan et al., 2004). Internally mixed sea salt and organic particles were observed in three of these studies (Middlebrook et al., 1998; Murphy et al., 1998; Lee et al., 2002). At Trinidad Head, California, Allan et al. (2004) observed

qualitatively-similar mixtures of sulfate and organics in some particles that were separate from other particles containing sea salt components.

The components of particles observed by single particle microscopy and mass spectrometry techniques include a range of ratios of components with each particle type (Murphy and Thomson, 1997; Gao and Anderson, 2001; Allan et al., 2004). For example, particles with varying fractions of sulfate, and hence varying CCN activity, will be grouped together in a single type by some single particle techniques. Since different ratios of components will have different properties, particles classified by qualitative single particle techniques as internally mixed may have different properties even though they contain the same components. By measuring the solubility, water uptake, surface tension, and scavenging of ambient aerosol, particles can be classified by their properties rather than (or in addition to) their composition. For assessing aerosol-cloud interactions, these two approaches have been used to measure differences in particle properties and behavior. The first uses solubility, hygroscopicity, or surface tension of particles to predict the activation of particles to droplets. The second approach uses mass scavenging coefficients to quantify the partitioning of droplets and particles, by both activation of CCN and scavenging of interstitial particles within the cloud. The second approach can be extended to provide additional information on both composition and mixing by measuring mass scavenging for multiple chemical components simultaneously.

The mass scavenging coefficient (F) quantifies the tendency of a particular chemical component to be incorporated into cloud droplets (Baltensperger et al., 1998) and has been used to differentiate particle types that partition into cloud droplets and interstitial particles with different efficiencies (Hallberg et al., 1992; Mertes et al., 2001; Sellegri et al., 2003). While the measured differences in mass scavenged fraction are useful to describe some aspects of particle composition, there is insufficient information in this measurement to quantify the composition of each particle. For any chemical component,

$$F = \frac{M_{\text{residual}}}{M_{\text{total}}} \tag{1.1}$$

where M_{residual} is the droplet residual mass and M_{total} is the total mass of the

component in both the particle and droplet phases. For external mixtures, each component could have a unique mass scavenging coefficient depending on its hygroscopicity. Baltensperger et al. (1998) found sulfate near $F = 1$ for submicron particles at a high-alpine site in the Bernese Alps. A similar study at a remote marine site found the sulfate activation fraction to be closer to 0.8, where sulfate concentrations were between 0.2 and 2 μg m^{-3} (Heintzenberg and Leck, 1994). For an internal mixture with the same fraction of each component, mass scavenging coefficients will be constant for all components even if the components have different hygroscopic properties.

Hallberg et al. (1992) found sulfate externally mixed with elemental carbon on the basis of the observed scavenged fraction (0.18 and 0.06, respectively). Similarly, Sellegri et al. (2003) identified particles as internal mixtures of elemental carbon and sulfate, ammonium, or nitrate based on the higher mass scavenging coefficient obtained for elemental carbon ($F = 0.33$) than organic carbon ($F = 0.14$). In addition, they determined the organic aerosols to be externally mixed from those inorganic species ($F = 0.76$). Mertes et al. (2001) report similar mass scavenging values for organic carbon, sulfate, sodium, and ammonium (from 0.49 to 0.55) and smaller scavenging coefficients for both black carbon (0.17) and graphitic carbon (0.14), indicating that black carbon and graphitic carbon were in separate particles from those that contained a mixture of organic carbon, sulfate, sodium, and ammonium. Heintzenberg and Leck (1994) show that sulfate and elemental carbon have similar scavenging efficiencies for polluted and remote marine regions, but they have very different scavenging efficiencies over continental regions, illustrating that different particle-droplet partitioning may be caused by source-based differences such as varying the fractions of sulfate and elemental carbon or including other components.

Here we present the measured chemical composition of particles and droplet residuals during the Dynamics and Chemistry of Marine Stratocumulus-II (DYCOMS-II) experiment from 2001. The meteorological characteristics of the stratocumulus layers (including entrainment and drizzle) observed for the seven nighttime and two daytime research flights are described in Stevens et al. (2003). Twohy et al.

(2005b) showed that DYCOMS-II below-cloud particle number concentrations (0.1 to 3.0 μm diameter) were correlated positively with droplet number concentrations and negatively with droplet size. This work reports the mass scavenging coefficients for a series of chemical components measured in and below cloud. These component-specific mass scavenging coefficients are used to evaluate if the partitioning of those components between unactivated particles and droplet residuals is consistent with that expected for particles with the same internal mixtures of components at fixed ratios. Both below-cloud and interstitial unactivated particles were measured to compare their partitioning behavior and the spatial homogeneity of the sampled air masses.

1.2 Method

Aerosol and cloud properties were measured during the DYCOMS-II experiment off the coast of San Diego in July 2001. The aim was to characterize the chemistry and microphysics of marine stratocumulus clouds lying within a well-mixed boundary layer. Most flights in the NCAR C-130 aircraft consisted of a ferry leg to approximately 300 km offshore, followed by a series of circles in, above, and below cloud. The research flights each attempted to follow the advection of a single air mass, however, wind shear and flight pattern restrictions prevented the flight paths from being strictly Lagrangian (Stevens et al., 2003). Six flights are analyzed here: flights 3, 4, 5, and 7 measured between 2200 and 0600 local time, and flights 8 and 9 measured between 1100 and 2200 local time. Samples from flights 3, 4, and 5 were collected during circles which were constant within 20 m, and samples from flights 7 and 8 were constant within 50 m. Flight 9 did not contain constant altitude circles, so samples spanned 200 to 400 m vertically, reducing the accuracy of the reported concentrations. Flights 1 and 2 did not collect cloud droplet residuals and are omitted from this analysis. Stratocumulus decks were dense and generally uniform, and drizzle was common with an average 0.5 mm day^{-1}. More detailed information on flight patterns and meteorological conditions is provided in Stevens et al. (2003).

Five aerosol instruments and inlets on the C-130 aircraft were used to measure particle and droplet size and to collect samples for the size ranges in Table 1.1. Particle size distributions were recorded by the wing-mounted Particle Measuring Systems Passive Cavity Aerosol Spectrometer Probe (PCASP-100x). The PCASP measures number concentrations across nominal size bins ranging from 0.1 to 3.0 μm with 1 s resolution, where the size measured is assumed to be dry (Strapp et al., 1992). Spikes and negative values were removed prior to analysis. Cloud droplet (2 to 47 μm) size distributions were measured during flights 3, 4, 7, 8, and 9 with the Forward Scattering Spectrometer Probe (FSSP-100) [`http://www.eol.ucar.edu/raf/Bulletins/B24/fssp100.html`]. The FSSP optical particle counter uses Mie theory to calculate the size of each particle based on the intensity of the scattered light. Flight 5 droplet concentrations were calculated from the "fast-FSSP" (Brenguier et al., 1998) because the FSSP-100 instrument data were not available (VanZanten et al., 2005). The two instruments provide comparable measurements for the drop size and number concentration ranges measured here (Burnet and Brenguier, 2002).

Cloud droplet residual composition was determined using a counterflow virtual impactor (CVI) inlet, which isolates cloud droplets larger than approximately 9 μm at aircraft speeds of 100 m s^{-1} in a stream of nitrogen gas flowing out through the CVI tip (Twohy et al., 2001). The droplets are dried and the non-volatile residual mass is collected on 37 mm stretched Teflon filters (Teflo Membrane, Pall Corp., Ann Arbor, MI). A small impactor (0.55 μm cut dried diameter) was installed upstream of the filters to provide an equivalent upper size cut to the impactor used in the solid diffuser inlet (SDI) sampling system (1.3 μm cut ambient diameter). The 0.55 μm cut size was used to correct for the expected difference in relative humidity between the ambient humidity SDI and dried CVI samples (assuming growth factors for NaCl). The filters were analyzed by Fourier Transform Infrared (FTIR) spectroscopy (Maria et al., 2003) and X-ray Fluorescence (XRF) to provide mass concentrations for (organic and inorganic) functional groups and elements, respectively. XRF analysis was performed by Chester Labs (Maria and Russell, 2005). All concentrations that were less than or equal to the

detection limit were removed. Elevated levels of chloride and sulfur in the CVI at lower relative humidity were associated with bouncing of dried supermicron sea salt particles, which artificially enhanced the mass collected on the Teflon filters. This artifact was measured in the laboratory as a function of dry size by comparison of NaCl to ammonium sulfate particles, and the resulting calibration curve was used to correct the chloride and sea salt sulfur, sulfate, potassium, and calcium concentrations. The correction factor R was applied as in Eq. 1.2,

$$Cl_{\text{m,submicron}} = Cl_{\text{m,tot}} - \frac{Cl_{\text{c,tot}} - Cl_{\text{c,submicron}}}{R} \tag{1.2}$$

where m and c denote measured and calculated values, respectively. Chloride is used as a marker for unreacted sea salt (NaCl), which may underestimate total sea salt concentrations due to loss of some chloride mass as HCl gas (Seinfeld and Pandis, 1998). SEM measurements indicate that a majority of supermicron particles were sea salt for flights 3, 5, and 7. Bouncing of the reacted supermicron sea salt particles (which account for between 19% and 55% of supermicron particles) is less likely than unreacted sea salt particles (which account for between 34% and 87% of supermicron particles) (Boskovic et al., 2005; Brach et al., 2000; Li et al., 2003), making chloride an appropriate surrogate for the unreacted sea salt particles which represent the bounced fraction of supermicron particles.

Sea salt stoichiometric ratios (Warneck, 1988) were used to determine and correct the sea salt contributions of sulfur, sulfate, potassium and calcium concentrations. The uncertainty associated with this correction scales with the fraction of the component that is from sea salt, which is a large fraction of the chloride and a smaller fraction of the sulfur, sulfate, potassium, and calcium. Correction factors for chloride are on the order of 0.04 while those for sulfur, sulfate, potassium, and calcium are between 0.5 and 0.7.

DYCOMS-II particles between 0.2 and 1.3 μm were collected using the solid diffuser inlet (SDI) (Huebert et al., 2004). The SDI was followed by a three-stage particle concentrator (3SPC) consisting of three slit virtual impactors, which concentrated the volume of particles collected on the Teflon filters by up to a factor of 19 (Maria et al., 2002). These Teflon filters were analyzed by FTIR spectroscopy

and XRF. Both particles and cloud droplets were sampled to provide below and in-cloud concentrations (μg m^{-3} of air sampled) for each chemical component.

A porous diffuser low turbulence inlet (LTI) following the design of Huebert et al. (2004) was used to collect single particles less than 6 μm on polycarbonate membrane filters with a Streaker (PIXE International) for SEM (> 0.26 μm). Smaller particles (< 0.26 μm) were collected by a 3-stage impactor following the LTI for transmission electron microscopy (TEM). The four different types of samples collected were designated as "below-cloud particles" (sampled through the SDI, discussed in section 3.2.1), "in-cloud or interstitial particles" (sampled through the SDI, discussed in section 3.2.2), "droplet residuals" (sampled through the CVI, discussed in section 3.3), and "single particles" (sampled through the LTI and analyzed by SEM and TEM, discussed in section 4.2).

1.3   Results

During each flight aerosols and clouds were characterized by particle size distribution, vertical concentration profile, and mass scavenging efficiency. Flights 4, 7, and 8 were clean relative to marine conditions, with less than 250 cm^{-3} (where we have identified flights as clean based on low below-cloud condensation nuclei (CN) number concentration) while flight 9 was closer to shore and relatively polluted, with greater than 400 cm^{-3}. The concentrations during flights 3 and 5 fall between 250 and 300 cm^{-3}.

1.3.1   Meteorological conditions

Figures 1.1 and 1.2 show vertical profiles of virtual potential temperature (θ_v), vertical velocity (w), horizontal wind speed (WS), ozone mixing ratio, water mixing ratio (MR), and liquid water content (LWC) for each research flight. Profiles were measured near the beginning and end of each 9 hour flight. Comparing the profiles for each flight shows few changes in temperature, updraft, water vapor, and ozone mixing ratio profiles between the start and end of sampling. The depth of the mixed layer obtained from virtual potential temperature, liquid water con-

tent, or water mixing ratio varies between 560 m and 1020 m and marks the cloud top altitude (Table 1.2): flights 8 and 9 have shallow mixed layers (less than 600 m). Vertical velocity and wind speed profiles are consistent with other markers of mixed layer depth and show reduced updrafts in and shear at the boundary between the mixed layer and the free troposphere. The average liquid water content in cloud ranges from 0.19 to 0.43 g m^{-3} and was the highest in flight 7, which had the thickest cloud layer observed during vertical profile measurements. The standard deviations of vertical velocity during these sample periods range from 0.11 to 0.73 m s^{-1} (Table 1.2).

1.3.2   SDI particle (0.2 to 1.3 μm) size and composition

Figures 1.3a and 1.3b show below-cloud and interstitial particle composition, respectively. Compounds are divided into categories based on their reactive properties and origin. Metals and mineral components include aluminum, titanium, chromium, manganese, iron, copper, vanadium, cobalt, nickel, potassium, calcium, silicon, and silicate ions. The ammonium and sulfate category also includes elemental sulfur since the latter is dominated by sulfate (Seinfeld and Pandis, 1998). The organic category reflects the total measured amounts of saturated aliphatic C-C-H, carbonyl C=O, and organosulfur C-O-S; the latter two were above detection limit in less than 5% and 12% of the samples, respectively, and provide insufficient data for comparison of droplet and particle composition. Chloride is measured by XRF and reflects the unreacted sea salt fraction [Seinfeld and Pandis, 1998].

Panels in Figure 2.7 show the interstitial and below-cloud particle size distributions measured by the PCASP, averaged for the SDI sampling periods. The PCASP measured continuously for the duration of the flight (approximately 9 hours); the SDI was only used to collect particles during constant altitude circles lasting 30 min to 1 h. The below-cloud distributions are characterized by a broad peak near 0.2 μm of varying concentration (Table 1.3). Mass-mean ($\bar{D}_{m,SDI}$) and number-mean ($\bar{D}_{SDI}$) diameters of particles within the SDI cutoff size range of 0.2 to 1.3 μm for the six flights range from 0.89 to 1.1 μm and from 0.28 to 0.36 μm,
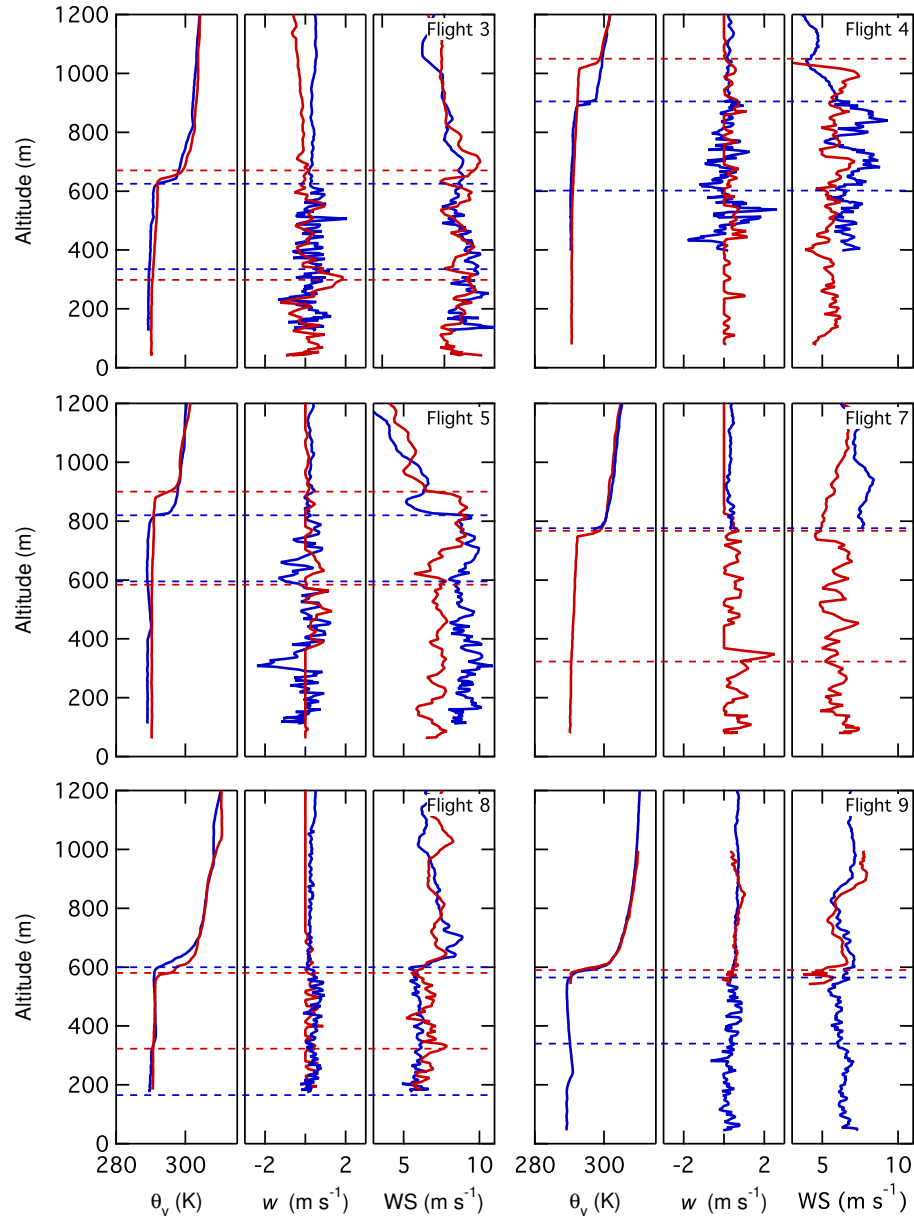
Figure 1.1: Altitude profiles of virtual potential temperature (θ_v), vertical velocity (w) and horizontal wind speed (WS) for the six research flights. Multiple lines indicate multiple measured profiles within each flight and are differentiated by line color with blue lines at the beginning of the flight and red lines at the end. Horizontal dashed lines mark cloud top and bottom, and are derived from LWC. Virtual potential temperature is used to mark cloud top for profiles in flights 4, 7, and 9 where LWC is not available.
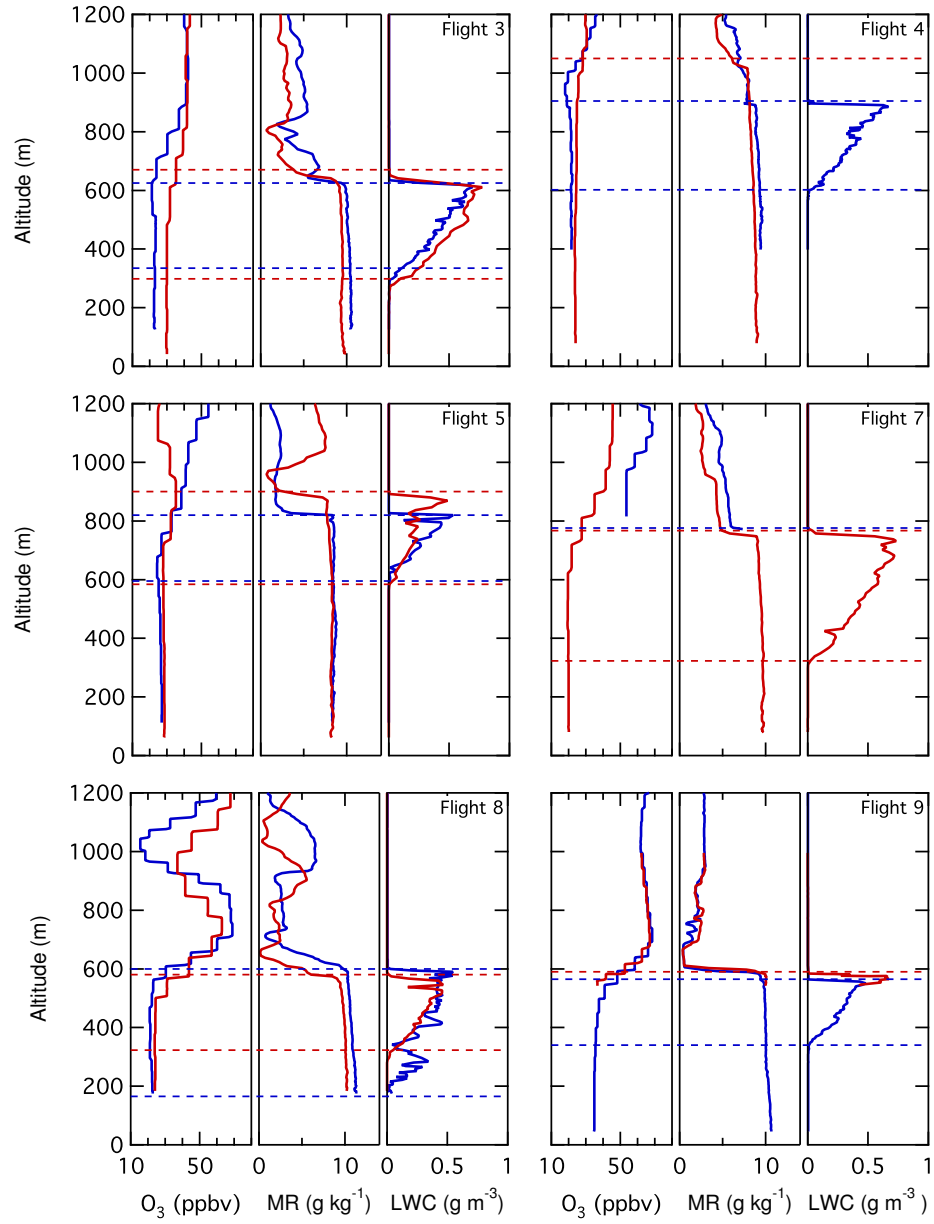
Figure 1.2: Altitude profiles of ozone (O_3), water mixing ratio (MR), and liquid water content (LWC) for flights 3, 4, 5, 7, 8, and 9. Line colors are the same as Figure 2.

respectively (Table 1.4). Size distributions in all flights show higher concentrations of smaller particles ($< 0.5 \; \mu$m) in below-cloud than in interstitial samples. Flights 3, 4, 5, 7, and 8 show smaller below-cloud $\bar{D}_{m,SDI}$ (0.48 to 0.66 μm) than interstitial $\bar{D}_{m,SDI}$ (0.84 to 1.12 μm) (Fig. 4).
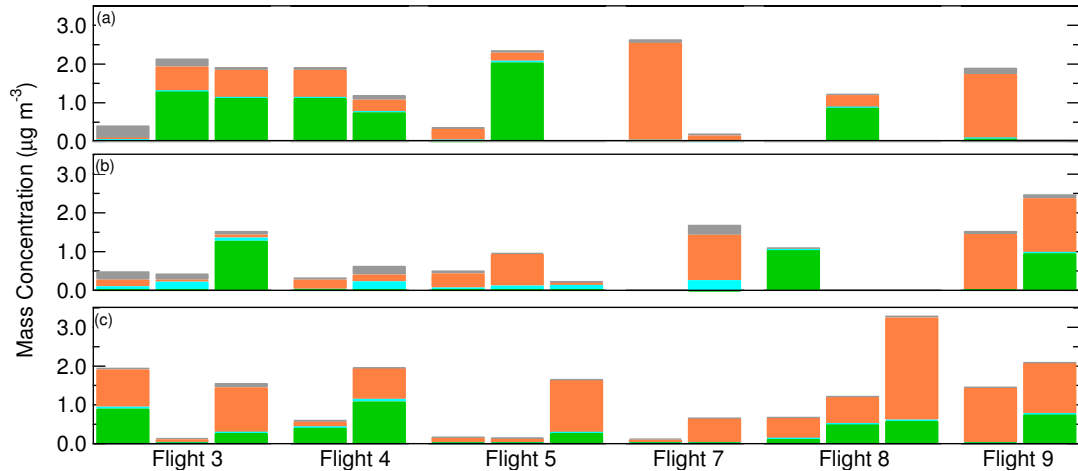
Figure 1.3: Mass concentration of (a) SDI particles below-cloud, (b) SDI particles in-cloud, and (c) CVI droplet residual particles. Metals and mineral components (grey) include aluminum, titanium, chromium, manganese, iron, copper, vanadium, cobalt, nickel, potassium, calcium, silicon, and silicate ions. The ammonium and sulfate category (orange) also includes elemental sulfur. Organic compounds (green) include saturated aliphatic C-C-H, carbonyl C=O, and organosulfur C-O-S although only 5% of samples had carbonyl above detection limit and 12% of samples had organosulfur above detection limit. Chloride is grouped alone (turquoise). Individual bars represent 30 min or 1 h continuous sampling periods. The number of samples taken varies by flight and by sample type.

Vertical profiles of concentrations of the chemical components collected by the SDI during each flight are illustrated in Figure 1.5. The two interstitial samples for flight 9 were collected at altitudes that varied by ± 200 m including cloud top and bottom within each circle. Within each flight the relative proportions of most chemical components are consistent at the sampling altitudes, indicative of well-mixed air masses, although there are some minor differences. All components show similar concentration profiles for the 6 flights.

Below-Cloud Particles

All below-cloud sample particle number distributions have a mode centered between 0.18 and 0.25 μm, which we will refer to as the 0.2 μm mode (Fig. 2.7), with a shoulder or second mode at a smaller diameter. The 0.2 μm number mode corresponds to a mean mass diameter of about 0.55 μm. Below-cloud distributions
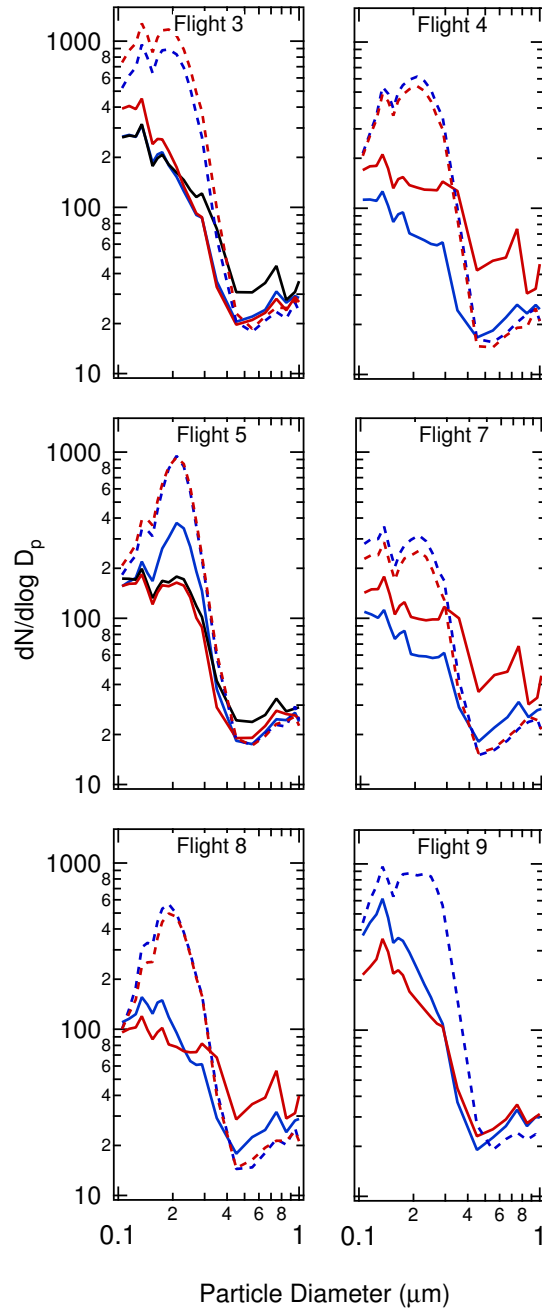
Figure 1.4: Panels contain the PCASP particle size distributions for the SDI size range and sampling intervals (between 30 min and 1 h) during each flight. $dN/dlogD_p$ values are plotted against particle diameter. Solid lines represent interstitial particle measurements averaged over a constant altitude sampling circle. Dashed lines represent below-cloud measurements averaged over a constant altitude sampling circle. Blue, black, and red lines mark samples collected at the beginning, middle, and end of the flights, respectively.
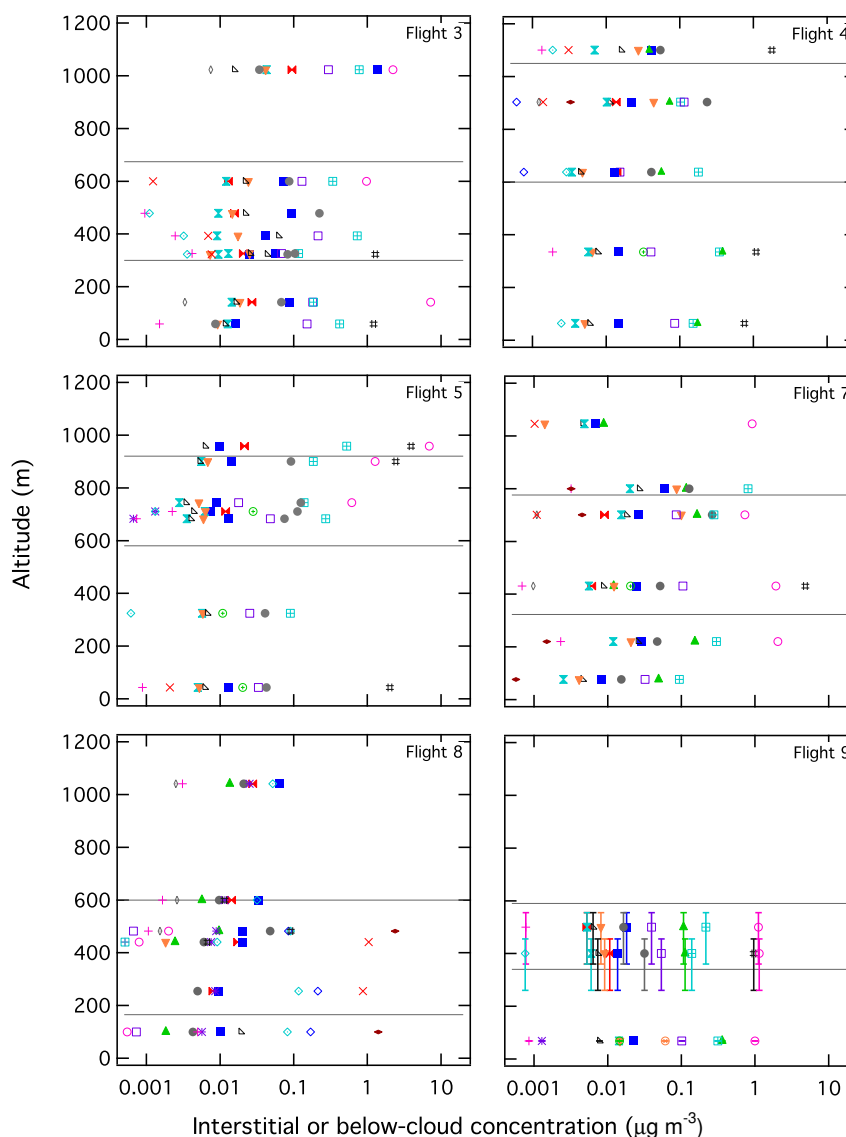
Figure 1.5: Panels contain the vertical distribution of species collected by the SDI in, above and below the cloud level. Grey lines mark the greatest vertical extent of cloud layer from Figures 1 and 2. Markers show: aluminum (solid red bowtie), silicon (solid blue square), sulfur (solid green upward triangle), potassium (solid turquoise vertical bowtie), calcium (solid orange downward triangle), vanadium (purple asterisk), iron (open black triangle), ammonium (open turquoise quartered square), sulfate (open pink circle), titanium (open grey narrow diamond), manganese (red x-cross), cobalt (open blue diamond), organosulfur C-O-S (open green circle with plus), nickel (solid dark red wide diamond), carbonyl C=O (open orange circle with x-cross), silicate (open purple square), aliphatic C-C-H (black pound), copper (open turquoise diamond), chromium (pink plus), and chlorine (solid grey circle). Vertical error bars indicate the altitude range of the sample when it exceeds ± 20 m, which is only for flight 9.

have a very small number of particles in a mode centered between 0.76 and 0.83 μm. In the 0.13 to 0.14 μm size bin, flight 9 had 47 cm^{-3}, the highest dN/dlogD_p peak concentration for the project. The below-cloud particle peak number concentrations are uniform within each of the six research flights, with little variation in mode diameter between samples or flights (Table 1.3).

Ammonium and sulfate make up the largest identified portion of the below-cloud particle mass for most flights, with an average mass concentration of 1.5 μg m^{-3} and mass fractions that range from less than 1% to 95% (Fig. 3a). Below-cloud organic mass concentrations range from below the detection limit to 2.0 μg m^{-3} and the organic mass fraction ranges from less than 1% to 87%. Below-cloud chloride was present in the largest concentration in flight 3 at 0.07 μg m^{-3}.

Interstitial Particles

The interstitial number distributions in Figure 2.7 show a smaller peak in the 0.2 μm mode (corresponding to a mass-mean diameter of about 1.1 μm) than is present in the below-cloud distributions, with between 63% and 73% of the particles having been removed or grown to droplets (Table 1.3). Flight 9 has the highest concentration of interstitial submicron particles, as well as a broad peak at 0.2 μm. The 0.8 μm interstitial mode has between 2 and 4 times higher concentrations than below-cloud, with significant variability both between and within the flights. Flights 4, 7, and 8 are relatively clean and have larger variations in interstitial particle size distributions between the sampling intervals than flights 3, 5, and 9, which have higher CN concentrations on average (Fig. 4). Flights 4, 7, and 8 also have higher drizzle rates (0.08 to 0.60 mm day^{-1}) than flights 3, 5, and 9 (below detection limit to 0.05 mm day^{-1}) (Table 1.2) and have heavy drizzle events contributing to between 20% and 64% of the total drizzle (Table 1 in VanZanten et al. (2005)). The differences in the in-cloud interstitial particle distributions, despite very similar ozone mixing ratios during flights 4, 7, and 8, probably result from these heavy drizzle events.

Ammonium and sulfate dominate the interstitial particle mass, with an average mass concentration of 1.0 μg m^{-3} (Fig. 1.3b). The interstitial organic

mass concentration varied the most between flights, ranging from below detection limit to 1.28 μg m^{-3}. Elevated chloride concentrations in interstitial particles relative to below-cloud particles and droplets may be attributed to the increased partitioning of semi-volatile chloride into unactivated particles in-cloud relative to below-cloud because of their larger water uptake. Interstitial chloride was highest in flight 7 at 0.26 μg m^{-3} .

1.3.3   Droplet mode size and droplet residual composition

Droplet size and concentration were measured by the FSSP-100 and fast-FSSP probes, with the mean diameter for each flight ranging from 6.6 to 11.3 μm. Figure 1.6 is similar to Figure 3 from Twohy et al. (2005b), where we have modified the data on the abscissa. Droplet number concentration measured by the FSSP and fast-FSSP shows a strong dependence on particle number concentration (0.2 to 1.3 μm only) measured by the PCASP ($R^2 = 0.76$), in agreement with the correlation of droplet number concentration and particle number concentration of the PCASP size range (0.1 to 3 μm) used by Twohy et al. (2005b). Drop size is also correlated (inversely) with particle number concentration ($R^2 = 0.69$). The most polluted flight (9) has the highest droplet concentration and the lowest mean droplet diameter (Twohy et al., 2005b). The two cleanest flights 7 and 8 have the largest drops and lowest droplet concentrations, respectively.

Chemical composition of droplet residual mass is shown in Figure 3c, with multiple samples acquired during each flight. Ammonium and sulfate constitute the bulk of the mass collected (above 0.5 μg m^{-3} in 10 of 15 samples) and from 22% to 95% of measured residual mass. Organic compounds also contribute significantly to residual mass (below detection limit to 1.1 μg m^{-3}), from less than 1% to 56%. Chloride is observed at lower concentrations in the droplet residuals than in interstitial particles, perhaps resulting from increased loss of chloride as HCl during cloud processing in aqueous cloud droplets (which are less acidic than interstitial particles) or during sampling and evaporation in the CVI.
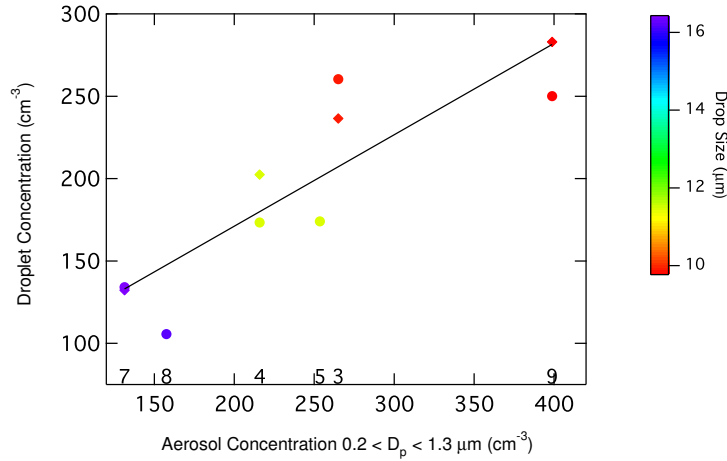
Figure 1.6: Droplet concentration as a function of particle number concentration for 0.2 to 1.3 um diameter particles. Color indicates droplet size as measured by the FSSP-100 for flights 3, 4, 7, 8, and 9 and fast-FSSP for flight 5. Droplets are defined by the two FSSP probes as cloud particles above 2 μm. Values along the y=0 line are flight number, and correspond to the markers above them. Shaded diamonds and shaded circles correspond to cloud bottom and cloud top, respectively. The best fit line (y = 0.55x + 60) has an R^2 = 0.76. Drop size correlates to particle number concentration (R^2 = 0.69).

1.3.4 Mass scavenging coefficients and cutoff diameter

Following Eq. 1.1, flight-averaged droplet residual concentrations M_{residual} for each component measured are shown to depend on the total concentration of that component M_{total}, which is the sum of the flight-averaged in-cloud particle (interstitial) concentration $M_{\text{interstitial}}$ and the droplet residual concentration M_{residual} (Fig. 1.7). This plot yields the mass scavenging coefficient F_{in} (Eq. 1.3) as the slope of the line.

$$F_{\text{in}} = \frac{M_{\text{residual}}}{M_{\text{residual}} + M_{\text{interstitial}}} \tag{1.3}$$

For below-cloud samples, M_{total} is $M_{\text{below−cloud}}$ and we can rewrite Eq. 1.3 as,

$$F_{\text{below}} = \frac{M_{\text{residual}}}{M_{\text{below−cloud}}} \tag{1.4}$$
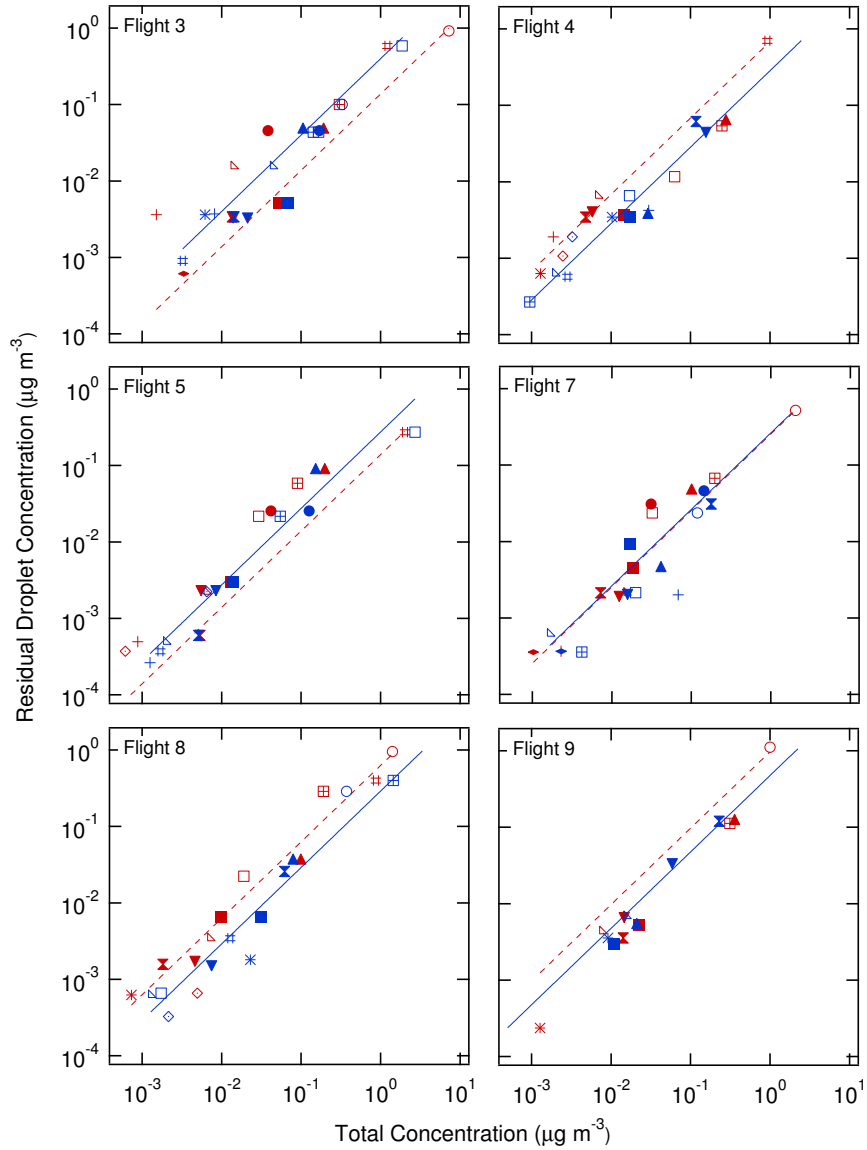
Figure 1.7: Panels contain the mass scavenging coefficient plots. Concentrations of components in droplet residuals are plotted on the ordinate (CVI); total concentrations in and below-cloud level are plotted on the abscissa. Marker shape is consistent with Figure 1.6. Blue markers and the blue solid fit line represent flight-averaged concentrations within the cloud, the red markers and the red dashed fit line represent below cloud samples. Scavenging coefficients (F) range from 0.14 to 0.97 below cloud and 0.26 to 0.40 in cloud. Best fit values for each panel are given in Table 1.6.

Here the slope of the line generated by plotting cloud droplet residual concentration against below-cloud particle concentration yields F_{below}.

Mass scavenging coefficients for each sampling interval were used with PCASP number distributions to calculate the cutoff diameter $D_p{}^*$ below which particles form droplets smaller than the lower size cut of the CVI (9 μm). First the total mass (M_{SDI}) of particles in the SDI size range was determined (Eq. 1.5).

$$M_{SDI} = \int_{D_p=0.2 \ \mu m}^{D_p=1.3 \ \mu m} \frac{D_p^3}{6} \pi \rho N_p \ dD_p \tag{1.5}$$

where ρ is the density of water and N_p is the number of particles in each size bin. From the mass scavenging fraction (F) and the total particle mass (M_{SDI}), $D_p{}^*$ is defined implicitly as

$$(1-F)M_{SDI} = \int_{D_p=0.2 \ \mu m}^{D_p=D_p^*} \frac{D_p^3}{6} \pi \rho N_p \ dD_p \tag{1.6}$$

The values for particle number (N_p) are binned such that $D_p{}^*$ precision is limited by the width of the measured size bins.

1.4 Discussion

1.4.1 Uniform particle-droplet partitioning of 18 chemical components

For spatially well-mixed, clean, low SO_2 air masses the bulk below-cloud and total (particle plus droplet) in-cloud composition of non-volatile components will be comparable and will result in similar F_{in} and F_{below} values. For less homogeneous regions, the below-cloud samples and interstitial samples collected in spatially and temporally separated air masses will be more variable. Flights 4 and 7 were chemically homogeneous in space and time, showing little change in mean ozone mixing ratio between sampling circles (1-3 ppbv) and small standard deviations within each circle (0.6-2.1 ppbv, as in Table 1.5). For flight 7 the mass scavenging coefficients were also consistent between the below and in-cloud measurements (Table 1.6). Flight 4 had homogeneous ozone mixing ratios and particle

compositions, but the mass scavenging coefficients in and below-cloud differed by a factor of 2. This difference may result from the missing (below detection limit) measurements of concentration of saturated aliphatic C-C-H in interstitial particles for both in-cloud circles during flight 4, since the organic mass scavenging coefficient has a significant influence on the line fit for the average mass scavenging coefficient. Chemical variability was higher in the more polluted flights (3 and 5, with 8-16 ppbv differences in mean ozone mixing ratios between sampling circles) and the day flights 8 and 9. The poor correlation between below-cloud particle and in-cloud droplet composition for these four flights (in Figure 1.3) suggests that the more polluted flights had more chemical variability associated with pollution plumes and the daytime flights had more changes in supersaturation and mixing associated with diurnal heating.

Figure 1.7 shows the droplet residual mass for each component plotted against the total mass of that component in-cloud (particle plus droplet) or below-cloud (particle only). Aliphatic C-C-H functional groups and sulfate ions dominate the composition, while mineral components constitute most of the remaining mass. Trace metals (vanadium, nickel, manganese, chromium, titanium, cobald, iron, and copper) have the lowest mass concentrations, typically with 1 to 10 ng m^{-3}. Table 1.6 summarizes the mass scavenging coefficients (F_{in} and F_{below}) and correlation coefficients for all six flights. The mean mass scavenging coefficients for the night flights in the DYCOMS-II study lie between 0.26 and 0.40 for interstitial particle concentrations (F_{in}, in-cloud mass scavenging coefficients) and between 0.14 and 0.68 for below-cloud particle concentrations (F_{below}, below-cloud mass scavenging coefficients), with each averaged over 18 chemical components. Droplet composition and particle composition within each flight and sample type (below-cloud versus in-cloud) are well correlated with slope uncertainties within $\pm$ 0.06 in night flights and within $\pm$ 0.11 in day flights. There is considerably more variation between the flights with factors of 1.5 and 4 separating the lowest and highest in-cloud and below-cloud average mass scavenging coefficients. One reason for this may be the variation in cloud supersaturation for different flights, which is inferred from the standard deviation of updraft velocity since supersaturation

cannot be measured (Table 1.2). Flights 4 and 7 have consistent updraft velocities with standard deviations of 0.60-0.69 m s^{-1}. Flights 3 and 5 have more variability with ranges of 0.58-0.74 m s^{-1} and 0.43-0.66 m s^{-1}, respectively.

Table 1.7 lists the day and night mass scavenging coefficients averaged over multiple flights for each component measured. Single-component F values are mostly between 0.2 and 0.4, with the least variation for nighttime in-cloud samples. Scavenging coefficients of the two most abundant components (aliphatic C-C-H and sulfate) have averages of 0.23 and 0.39, respectively. The correlation coefficients between the concentration of each compound in the particle phase and the concentration measured in the residual droplets is greater than 0.83 for 15 of the 16 comparisons and greater than or equal to 0.90 for 11 of the 16 comparisons (Table 1.6). This correlation is consistent with though not sufficient for internal mixing of the particles in the 0.2 to 1.3 μm diameter size range. The hygroscopic components had mass scavenging coefficients that were similar to less hygroscopic components, and hygroscopicity and mass scavenging were not correlated. For example, sulfate scavenging coefficients vary from 0.30 (below average efficiency) to 0.47 (above average efficiency) which is similar to sulfate mass scavenging reported in Mertes et al. (2001) where particles were mixtures of sulfate, organic carbon, sodium, and ammonium. The range of coefficients for sulfate suggests that the sulfate, organics, and other inorganic compounds may not have always been present in the same proportions or that variability in meteorological conditions and inlet efficiencies (see Section 4.3) has influenced measured mass scavenging efficiencies. These findings are consistent with the conclusions of Murphy et al. (2006), who performed single-particle analysis using laser mass spectrometry and determined that over 90% of accumluation mode particles (0.1 to 1 μm) away from local sources were internal mixtures of sulfate and organics. The consistency in F over the 18 components strongly suggests that sea salt, sulfate, organics, trace metals, and mineral components are present as mixtures within the same particle types in submicron particles but is not sufficient to show that all particles are internally mixed, especially since activation and in-cloud scavenging processes are indistinguishable. However, the similarity of mass scavenging coefficients for

multiple chemical components in the observed clouds means that the differences among the particle compositions do not have significant effects on their partitioning into droplets when cloud formation and processing mechanisms are considered together.

1.4.2 Submicron below-cloud particle mixtures with sea salt

Single particle below-cloud TEM and SEM data for individual samples from flights 3, 5, and 7 are shown in Figure 1.8. Particles in the two smallest size channels are measured by TEM; those above 0.26 μm are measured by SEM. The particles are classified by K-means cluster analysis as employed by Anderson et al. (1996), resulting in simpler categories for the cleaner marine conditions of DYCOMS-II than the Bermuda particles: organic and soot (which are unresolved by SEM), unreacted sea salt (similar to categories 31- 35, and 36 in Anderson et al. (1996)), reacted sea salt (categories 22-24, 30, 41, 43, 46, and 49), metal or mineral components (categories 1- 21, 28, 38, 42, 44, 51, and 57), and ammonium sulfate (category 25), though no particles above 0.26 μm were classified as ammonium sulfate. Other sulfate salts (categories 26, 27, and 29) include calcium, magnesium, sodium and potassium sulfate and contain smaller amounts of sodium, and potassium than is expected for sea salt. These particles appear to be a mixed-cation sulfate that is part of normal sea salt but may have been mechanically separated from sodium chloride. Similar particles were observed by Pósfai et al. (1995) and Anderson et al. (1996). Organic compounds that were internally mixed with sulfate or sea salt were not resolved by the weak carbon X-ray signal and may be underestimated or omitted. The bulk samples collected with the SDI for flights 3, 5, and 7 (Fig. 1.3a, b) are similar in composition to the sea salt single particles described in Figure 1.8. The measured submicron composition from FTIR spectroscopy and XRF is consistent with the TEM and SEM results. The size-resolved composition from the TEM and SEM illustrate that for flights 3, 5, and 7, between 71% and 91% of particles with diameters larger than 0.26 μm had similar sea salt-containing compositions (internal mixtures of sea salt with varying ratios). Particles below 0.26 μm
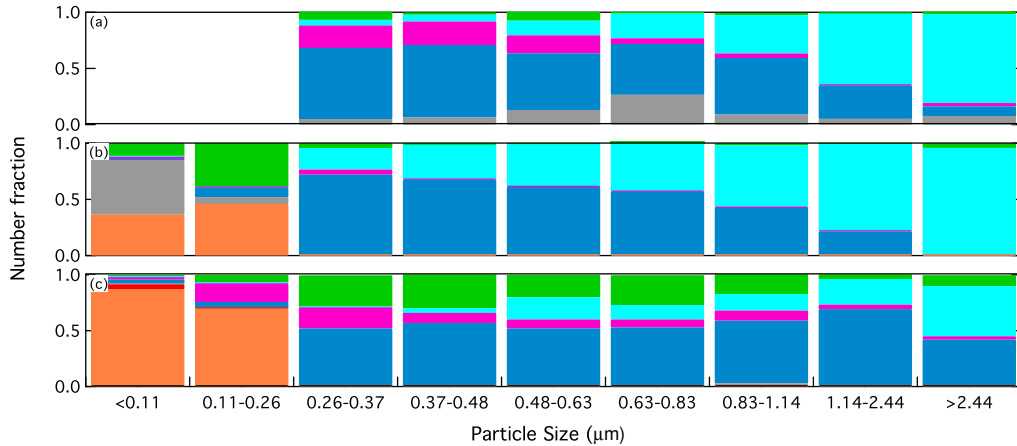
Figure 1.8: Size-resolved particle composition for the PCASP size range for flights (a) 3, (b) 5, and (c) 7. Transmission Electron Microscopy is used for $D_p < 0.26$ μm and Scanning Electron Microscopy for $D_p > 0.26$ μm. TEM measurements were not available for flight 3. Composition categories include: metals and mineral components (grey), ammonium sulfate (orange), unreacted sea salt (turquoise), partially and completely reacted sea salt (dark blue), other sulfate salts (magenta), and organics and soot (green). TEM size channels also include mixed (red) and unresolved (black) composition categories.

diameter have different and more variable compositions from the larger particles. Although these particles contribute a significant fraction to particle number the mass of these particles is too small to affect the mass-based scavenging coefficients for most chemical components.

1.4.3   Drop size effects on inlet efficiency and mass scavenging

DYCOMS-II marine stratocumulus clouds are characterized by increasing droplet size with altitude (inferred from increasing liquid water content without changes in droplet number concentration) (Straub et al., 2007), making the efficiency of the CVI for sampling drops increase with sampling altitude within clouds that contain some drops that are below this cutoff. Figure 1.9 shows that the fraction of droplets above 9 μm is correlated to normalized altitude $\bar{h}$ for each sampling interval within the cloud (with $R^2 = 0.6$), with $\bar{h}$ calculated as
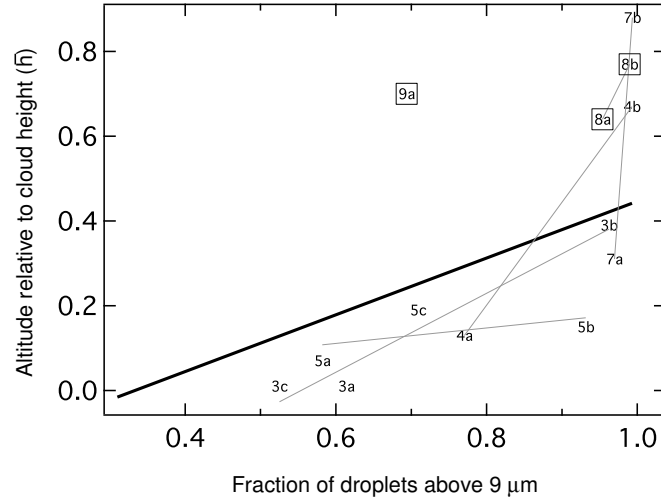
Figure 1.9: Fraction of droplets above 9 μm diameter as a function of $\bar{h}$, where $\bar{h}$ is the altitude of the sample within the cloud normalized by the cloud height (Eq. 1.7). Each flight has either two or three droplet sampling intervals. The bold line represents the best fit (y = 0.67h - 0.2) of night flights (3, 4, 5, and 7); daytime flights 8 and 9 (boxed) were not included in the fit. Grey lines show the trend for individual flights and are a guide for the eye since there are 3 or fewer points in each fit.

$$\bar{h} = \frac{z - z_{\text{base}}}{z_{\text{top}} - z_{\text{base}}} \tag{1.7}$$

(where z is the sample altitude and z_{base} and z_{top} are the cloud base and top altitudes, respectively). The samples taken closer to the cloud top contain a larger fraction of droplets above the lower CVI cutoff diameter as they coincide with the maximum liquid water content in the vertical profile (Fig. 1.2).

The calculation of mass scavenging coefficients is sensitive to the fraction of particles activated to droplets below 9 μm. The cutoff size $D_p{}^*$ (Eqns. 1.5 and 1.6) is a function of the size distribution of the particles sampled, their composition (specifically the amount of soluble material in the particles), and the supersaturation. A measure of the representativeness of the mass scavenging coefficients of the entire droplet population is provided by the ratio of below-cloud $D_p{}^*$ to $\bar{D}_{m,SDI}$. For ratios less than 1, the mean size is larger than the cutoff size, suggesting that more than 50% of below-cloud particles would activate to droplets greater

than 9 μm. From the 11 below-cloud samples analyzed, 5 samples have ratios less than 1, indicating that the measured compositions of cloud droplet residuals are representative of at least 50% of the droplet population (Table 1.8).

The mean mass PCASP diameter $\bar{D}_{m,PCASP}$ varies between 2.5 and 2.6 μm (Table 1.4). This diameter is approximately 1.5 times larger than the diameter of the particles collected through the SDI, which have $\bar{D}_m$ between 0.89 and 1.1 μm. The flights with the larger $\bar{D}_{m,SDI}$ (4, 7, and 8) are also the flights with the larger $\bar{D}_{m,PCASP}$. The SDI particle mass makes up between 3 to 4% of the 0.1 and 3.0 μm mass. Flight 7 is the cleanest flight, containing the lowest SDI number fraction and second lowest SDI mass fraction (Table 1.4).

Twohy et al. (2005b) found that between 70% and 100% of particles (by number) in the nighttime below-cloud samples (in the PCASP size range of 0.1 to 3.0 μm) were scavenged to form droplets measured by the FSSP-100 and fast-FSSP in DYCOMS-II [Figure 3, Twohy et al. (2005b)], while the nighttime mass scavenging coefficients reported here are between 14% and 68% below-cloud (Table 1.6). This difference is attributed to the missed activated mass in droplets between 2 μm (lower FSSP-100 limit) and 9 μm (lower CVI limit), which yields mass scavenging coefficients that are biased low relative to a hypothetical inlet that collects all cloud drops. This difference is larger for flights with small average drop diameters (flights 3, 5, and 9) and for samples collected near cloud bottom. The dependence of mass scavenging coefficient on drop size in Figure 1.10 shows a consistent increase in mass scavenging coefficient of night flights with an increasing fraction of drops above 9 μm. Three flights (4, 8, and 9) contained samples with more than 50% of the particle mass collected by the CVI were within the flight to flight variability of the number activation reported in Twohy et al. (2005b).

1.5   Conclusion

The 0.2 to 1.3 μm particles sampled in and below-cloud during DYCOMS-II partition to cloud droplets as if they are internally mixed, consistent with the SEM composition measurements showing that most particles between 0.26 μm and 1.14
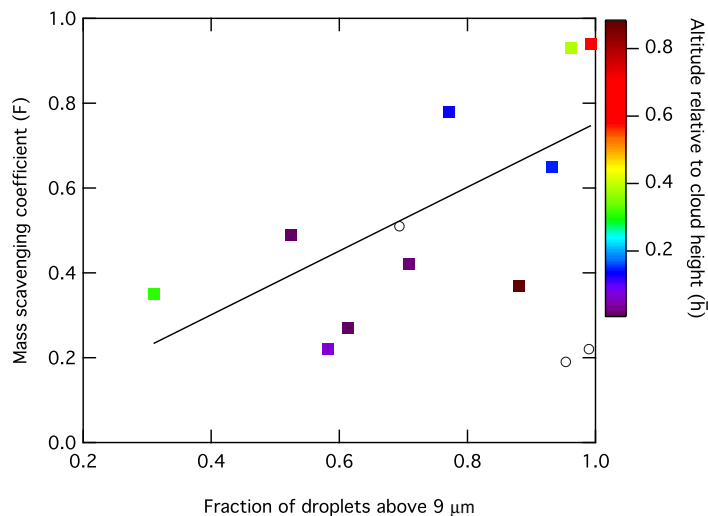
Figure 1.10: Mass scavenging fraction as a function of the fraction of droplets above 9 μm for each interstitial sample. Each flight has multiple samples. The best fit through nighttime flights 3, 4, 5, and 7 (square markers) is y = 0.75x (black line); daytime flights 8 and 9 are symbolized with open circles. Color indicates the sample altitude normalized relative to cloud height $\bar{h}$, as given in Eq. 1.7.

μm are internal mixtures with reacted and unreacted sea salt. The 18 measured organic and inorganic functional groups, mineral components, and trace metals show nighttime in-cloud mass scavenging coefficients between 26% and 47% for droplets larger than 9 μm diameter. For each flight and sample type (in-cloud or below-cloud) there is little variation between component-specific mass scavenging coefficients, even for components with different hygroscopicity. Flight 4 has clean marine conditions, well-mixed and consistent ozone mixing ratios, and very similar variations in updraft velocity throughout the flight resulting in a droplet residual composition that is very similar to the below-cloud particle composition. SEM measurements for flights 3, 5, and 7 show that greater than 90% of the number of particles above 0.26 μm are internal mixtures of sea salt, sulfate and nitrate, with XRF and FTIR measurements identifying organic compounds and trace metals in this 0.8 μm mode. For 5 of the 11 CVI samples, more than half of the below-cloud particles were larger than the CVI cutoff size for particles activating to droplets larger than 9 μm. Droplets missed below 9 μm diameter biased the scavenging coefficients low (especially for lower cloud altitudes and smaller drop sizes) but

do not affect the observed uniformity of mass scavenging coefficients for the 18 components measured.

For the particle compositions sampled during DYCOMS-II, substantial physical and chemical evidence show that the measured chemical components partition between particle and droplet phases as if they are internally mixed. The combination of SEM identification of sea salt in 90% of the 0.8 μm-mode particles with physical measurements of uniform particle-droplet partitioning means that the scavenged fraction of particles behave as if the components were internally mixed in the particles.

Extrapolating these results to other meteorological conditions, sources, and locations is not warranted, as the particles sampled here are unique in their distance from sources (300 km off shore) with substantial time for prior processing in cloud layers. The low supersaturations of Pacific marine stratocumulus also mean larger activation diameters such that the smaller, less processed particles (which are externally mixed in many of the components measured here) do not contribute substantially to activated droplet mass. Studies of particle and droplet composition in other locations are needed to provide a more complete description of the partitioning of chemical components in other aerosol-cloud interactions.

1.6 Acknowledgments

Table 1.1: Particle measurements aboard the NCAR C-130 during DYCOMS-II

Instrument	Sample Type	Quantity Measured	Size Range (μm)
Inlets			
Counterflow Virtual Impactor (CVI)	Droplet	Droplet residual chemical composition	9 to 50
Solid Diffuser Inlet (SDI)	Particle	Particle chemical composition	0.2 to 1.3
Low Turbulence Inlet (LTI)	Particle	Single particle SEM and TEM	$< 6^a$
Spectrometers			
Forward Scattering Spectrometer Probe (FSSP-100)	Droplet	Droplet size distributions	2 to 47
Passive Cavity Aerosol Spectrometer Probe (PCASP-100)	Particle	Particle size distributions	0.1 to 3

[a]Estimated from losses by impaction on plumbing walls (Fig. 1.6, *Huebert et al.* [2004]).

Table 1.2: Cloud structure and mixing for stratocumulus layers in DYCOMS-II

Flight	Cloud top[a,b] (m)	Cloud bottom[a,b] (m)	mean LWC[a] (g m^{-3})	MR[a,c] (g kg^{-1})	WS[a,c] (m s^{-1})	Standard deviation in w[d] (m s^{-1})	Avg. drizzle rate (mm day^{-1})
3	625	300	0.37	10.5	11.6	0.72, 0.70, 0.58, 0.59, 0.74	0.05±0.03
	650	270	0.42	9.5	11.1		
4	900	605	0.32	9.4	6.9	0.69, 0.69, 0.62, 0.64	0.08±0.06
	1020[e]	n/v	n/v	n/v	5.6		
5	820	630	0.25	8.5	9.1	0.43, 0.61, 0.66	BDL
	880	595	0.19	8.3	7.5		
7	770[e]	n/v	n/v	n/v	n/v	0.67, 0.69, 0.60, 0.60	0.60±0.18
	770	340	0.43	9.6	6.1		
8	595	205	0.29	11.2	5.9	0.39, 0.42, 0.49	0.12±0.03
	580	300	0.26	10.2	6.5		
9	560	350	0.25	10.3	6.3	n/v	n/v
	585	n/v	n/v	n/v	n/v		

[a]Vertical profile mean values (Fig. 1.1 and 1.2). Most flights have two vertical profiles.

[b]Cloud top and bottom altitudes as measured by cloud liquid water content (LWC).

[c]Mean value of wind speed (WS), bounded by the temperature inversion. Mean value of mixing ratio (MR) is below cloud level only.

[d]Multiple vertical velocities for each flight represent individual flight circles along a constant altitude (Fig. 1.3).

[e]Cloud top levels were based on virtual potential temperature since LWC was unavailable. Cloud bottom altitude was not available for these profiles.

Table 1.3: PCASP particle size distribution properties for 0.2 μm particle mode

Flight	BC peak diameter[a] (μm)	BC concentration[a] (dN/dlogD$_p$ in cm^{-3})	Decrease in 0.2 μm mode in-cloud[b] (%)
3	0.19	890	73
	0.19	1200	
4	0.21	620	72
	0.21	540	
5	0.21	950	63
	0.21	930	
7	0.21	320	58
	0.21	250	
8	0.19	570	66
	0.19	500	
9	0.23	880	65

[a]Diameters and concentrations are given for each below-cloud (BC) sample within a given flight. [b]The difference between the average number concentrations of below-cloud and interstitial particles smaller than 0.35 μm.

Table 1.4: Mass and number size distribution properties for particles collected by the SDI (0.2 to 1.3 μm) and PCASP (0.1 to 3 μm)

	SDI fraction[a]		Mass-mean diameter, $\bar{D}_m$ (μm)		Number-mean diameter, $\bar{D}$ (μm)	
Flight	mass %	number %	0.2 to 1.3 (SDI)	0.1 to 3.0 (PCASP)	0.2 to 1.3 (SDI)	0.1 to 3.0 (PCASP)
3	3.3	31	0.96	2.5	0.30	0.24
4	3.1	46	1.0	2.6	0.35	0.35
5	3.9	52	0.92	2.5	0.28	0.23
7	3.1	28	1.1	2.6	0.36	0.31
8	2.8	28	1.0	2.6	0.32	0.26
9	3.5	27	0.89	2.5	0.29	0.20

[a]SDI fraction is the number or mass fraction of particles between 0.2 and 1.3 μm relative to the particles between 0.1 and 3.0 μm.

Table 1.5: Mean and standard deviation of ozone mixing ratios within and between constant altitude circles

Flight 3	Flight 4	Flight 5	Flight 7	Flight 8	Flight 9
Mean and Standard deviation of O_3 in each circle (ppbv)					
26±3.9	23±0.58	26±1.5	17±1.5	23±1.4	35±0.89
27±4.2	23±0.37	34±8.9	18±1.1	23±1.5	35±0.60
26±4.1	24±0.35	27±1.1	19±1.1	23±1.3	34±0.39
26±3.9	24±0.50	28±1.1	19±1.1	23±1.4	
42±2.4	24±0.39	28±1.3	20±0.94	23±2.1	
32±1.9	24±0.37		19±1.0		
32±1.8					
Standard deviation among circles					
6.0	0.62	3.2	0.95	0.089	0.68

Table 1.6: Flight-specific mass scavenging coefficients with correlation coefficients averaged over all chemical components

Flight	Below-cloud		In-cloud	
	F_{below}[a]	R^2	F_{in}[a]	R^2
3	0.14±0.02	0.83	0.40±0.03	0.94
4	0.68±0.06	0.92	0.28±0.01	0.98
5	0.14±0.01	0.94	0.27±0.06	0.53
7	0.25±0.01	0.98	0.26±0.02	0.96
8	0.63±0.04	0.90	0.29±0.02	0.86
9	0.97±0.11	0.90	0.47±0.01	0.98
Night (3,4,5,7)	0.17±0.02	0.86	0.31±0.03	0.86
Day (8,9)	0.71±0.06	0.90	0.37±0.01	0.98

[a]Slopes and one standard deviations are calculated by a best-fit linear regression.

Table 1.7: Mean mass scavenging coefficients for each measured chemical component[a]

Species	Below-cloud		In-cloud	
	Day flights (8,9)	Night flights (3,4,5,7)	Day flights (8,9)	Night flights (3,4,5,7)
Al	n/v[b]	n/v	0.27	0.4±0.2[c]
Ca	0.30±0.03	0.3±0.1	0.3±0.2	0.3±0.1
C-C-H	0.31	0.3±0.2	0.2±0.1	0.2±0.1
Cl	n/v	0.47±0.09	0.5±0.1	0.24±0.06
Co	n/v	n/v	n/v	0.28
Cr	n/v	0.4±0.2	0.41	0.3±0.2
Cu	0.12	0.34±0.05	0.38	0.27±0.05
Fe	0.34±0.02	0.4±0.2	0.33±0.08	0.3±0.1
K	0.3±0.2	0.2±0.1	0.3±0.1	0.2±0.1
Mn	n/v	n/v	n/v	0.3±0.2
NH_4	0.4±0.2	0.27±0.09	0.6±0.6	0.23±0.09
Ni	n/v	n/v	n/v	0.2±0.1
S	0.26±0.01	0.26	0.48±0.05	0.5±0.1
Si	0.3±0.2	0.25±0.07	0.23±0.03	0.13±0.06
SiO_4	0.54	0.17±0.05	n/v	0.3±0.1
SO_4	0.47±0.09	0.3±0.1	0.4±0.2	0.4±0.1
Ti	n/v	0.16±0.06	n/v	0.38
V	0.3±0.2	0.16	0.7±0.4	0.26±0.08

[a]Carbonyl C=O and organosulfur C-O-S were not present above detection limit in enough CVI samples to report individual mass scavenging values. [b]n/v indicates no value, due to one or more components being below detection limits in the particle or droplet phase. [c]The variability shown is the standard deviation of each component with more than one measurement above detection per flight.

Table 1.8: Inferred cutoff diameter D_p* for collection of droplets in the CVI[a]

Flight	Below-cloud (μm)	In-cloud (μm)	Ratio of below-cloud D_p* to $\bar{D}_{m,SDI}$[b]
3	1.0	1.1	2.1
	1.2	1.1	1.7
		1.1	
4	0.26	1.2	0.50
	0.26	1.2	0.49
5	1.1	1.1	1.8
	1.1	1.2	1.7
		1.2	
7	0.98	1.2	1.6
	1.1	1.2	1.7
8	0.26	1.2	0.51
	0.26	1.2	0.49
9	0.22	1.1	0.33
		0.22	

[a]Values were interpolated between bin edges to give a best estimate. Bin sizes were 0.1 μm for flights 3, 5, and 7 and 0.02 μm for flights 4, 8, and 9. Multiple samples were obtained during each flight. [b]$\bar{D}_{m,SDI}$ is the mass-mean diameter of particles between 0.2 and 1.3 μm.

References

Allan, J. D., Bower, K. N., Coe, H., Boudries, H., Jayne, J. T., Canagaratna, M. R., Millet, D. B., Goldstein, A. H., Quinn, P. K., Weber, R. J., et al., 2004. Submicron aerosol composition at Trinidad Head, California, during ITCT 2K2: Its relationship with gas phase volatile organic carbon and assessment of instrument performance. Journal of Geophysical Research–Atmospheres 109, doi:10.1029/2003JD004208.

Anderson, J. R., Buseck, P. R., Patterson, T. L., Arimoto, R., 1996. Characterization of the Bermuda tropospheric aerosol by combined individual-particle and bulk-aerosol analysis. Atmospheric Environment 30 (2), 319–338.

Baltensperger, U., Schwikowski, M., Jost, D. T., Nyeki, S., Gäggeler, H. W., Poulida, O., 1998. Scavenging of atmospheric constituents in mixed phase clouds at the high-alpine site jungfraujoch part I:: Basic concept and aerosol scavenging by clouds. Atmospheric Environment 32 (23), 3975–3983.

Boskovic, L., Altman, I. S., Agranovski, I. E., Braddock, R. D., Myojo, T., Choi, M., 2005. Influence of particle shape on filtration processes. Aerosol Science and Technology 39 (12), 1184–1190.

Brach, R. M., Dunn, P. F., Li, X., 2000. Experiments and engineering models of microparticle impact and deposition. The Journal of Adhesion 74 (1), 227–282.

Brenguier, J. L., Bourrianne, T., Coelho, A. A., Isbert, J., Peytavi, R., Trevarin, D., Weschler, P., 1998. Improvements of droplet size distribution measurements with the Fast-FSSP (Forward Scattering Spectrometer Probe). Journal of Atmospheric and Oceanic Technology 15 (5), 1077–1090.

Brock, C. A., Hudson, P. K., Lovejoy, E. R., Sullivan, A., Nowak, J. B., Huey, L. G., Cooper, O. R., Cziczo, D. J., De Gouw, J., Fehsenfeld, F. C., et al., 2004. Particle characteristics following cloud-modified transport from Asia to North America. Journal of Geophysical Research 109 (D23), D23S26.

Burnet, F., Brenguier, J. L., 2002. Comparison between standard and modified forward scattering spectrometer probes during the Small Cumulus Microphysics Study. Journal of Atmospheric and Oceanic Technology 19 (10), 1516–1531.

Charlson, R. J., Schwartz, S. E., Hales, J. M., Cess, R. D., Coakley Jr, J. A., Hansen, J. E., Hofmann, D. J., 1992. Climate forcing by anthropogenic aerosols. Science 255 (5043), 423–430.

Corrigan, C. E., Novakov, T., 1999. Cloud condensation nucleus activity of organic compounds: a laboratory study. Atmospheric Environment 33 (17), 2661–2668.

Cziczo, D. J., Murphy, D. M., Hudson, P. K., Thomson, D. S., 2004. Single particle measurements of the chemical composition of cirrus ice residue during CRYSTAL-FACE. Journal of Geophysical Research 109 (D4), D04201.

Dusek, U., Frank, G. P., Hildebrandt, L., Curtius, J., Schneider, J., Walter, S., Chand, D., Drewnick, F., Hings, S., Jung, D., et al., 2006. Size matters more than chemistry for cloud-nucleating ability of aerosol particles. Science 312 (5778), 1375.

Ervens, B., Cubison, M., Andrews, E., Feingold, G., Ogren, J. A., Jimenez, J. L., DeCarlo, P., Nenes, A., 2007. Prediction of cloud condensation nucleus number concentration using measurements of aerosol size distributions and composition and light scattering enhancement due to humidity. Journal of Geophysical Research-Atmospheres 112 (D10), D10S32.

Facchini, M. C., Fuzzi, S., Zappoli, S., Andracchio, A., Gelencsér, A., Kiss, G., Krivácsy, Z., Mészáros, E., Hansson, H., Alsberg, T., et al., 1999. Partitioning of the organic aerosol component between fog droplets and interstitial air. Journal of Geophysical Research 104 (D21), 26821.

Gao, Y., Anderson, J. R., 2001. Characteristics of Chinese aerosols determined by individual-particle analysis. J. Geophys. Res 106 (18), 037–18.

Hallberg, A., Ogren, J. A., Noone, K. J., Heintzenberg, J., Berner, A., Solly, I., Kruisz, C., Reischl, G., Fuzzi, S., Facchini, M. C., 1992. Phase partitioning for different aerosol species in fog. Tellus Series B Chemical and Physical Meteorology B 44 (5), 545–555.

Hansson, H. C., Rood, M. J., Koloutsou-Vakakis, S., Hämeri, K., Orsini, D., Wiedensohler, A., 1998. NaCl aerosol particle hygroscopicity dependence on mixing with organic compounds. Journal of Atmospheric Chemistry 31 (3), 321–346.

Hegg, D. A., Ferek, R. J., Hobbs, P. V., 1993. Aerosol size distributions in the cloudy atmospheric boundary layer of the North Atlantic Ocean. Journal of Geophysical Research 98 (D5), 8841–8846.

Heintzenberg, J., Leck, C., 1994. Seasonal variation of the atmospheric aerosol near the top of the marine boundary layer over Spitsbergen related to the Arctic sulphur cycle*. Tellus B 46 (1), 52–67.

Huebert, B., Howell, S., Covert, D., Bertram, T., Clarke, A., Anderson, J., Lafleur, B., Seebaugh, W., Wilson, J., Gesler, D., et al., 2004. PELTI: Measuring the passing efficiency of an airborne low turbulence aerosol inlet. Aerosol Science and Technology 38 (8), 803–826.

Kondo, Y., Miyazaki, Y., Takegawa, N., Miyakawa, T., Weber, R. J., Jimenez, J. L., Zhang, Q., Worsnop, D. R., 2007. Oxygenated and water-soluble organic aerosols in Tokyo. Journal of Geophysical Research 112 (D1), D01203.

Lee, S. H., Murphy, D. M., Thomson, D. S., Middlebrook, A. M., 2002. Chemical components of single particles measured with Particle Analysis by Laser Mass Spectrometry (PALMS) during the Atlanta SuperSite Project: Focus on organic/sulfate, lead, soot, and mineral particles. Journal of Geophysical Research 107, 4003.

Levin, Z., Teller, A., Ganor, E., Graham, B., Andreae, M. O., Maenhaut, W., Falkovich, A. H., Rudich, Y., 2003. Role of aerosol size and composition in nucleation scavenging within clouds in a shallow cold front. Journal of Geophysical Research 108, 4700.

Li, J., Anderson, J. R., Buseck, P. R., 2003. TEM study of aerosol particles from clean and polluted marine boundary layers over the North Atlantic. Journal of Geophysical Research 108 (D6), 4189.

Maria, S. F., Russell, L. M., 2005. Organic and inorganic aerosol below-cloud scavenging by suburban New Jersey precipitation. Environmental Science &Technology 39 (13), 4793–4800.

Maria, S. F., Russell, L. M., Turpin, B. J., Porcja, R. J., 2002. FTIR measurements of functional groups and organic mass in aerosol samples over the Caribbean. Atmospheric Environment 36 (33), 5185–5196.

Maria, S. F., Russell, L. M., Turpin, B. J., Porcja, R. J., Campos, T. L., Weber, R. J., Huebert, B. J., 2003. Source signatures of carbon monoxide and organic functional groups in Asian Pacific Regional Aerosol Characterization Experiment (ACE-Asia) submicron aerosol types. Journal of Geophysical Research 108, 8637.

Mertes, S., Schwarzenbock, A., Bruggemann, E., Gnauk, T., Dippel, B., 2001. Phase partitioning of black carbon, non-volatile organic carbon and soluble inorganic substances between the droplet and interstitial phase of clouds at Mt. Brocken, Germany. Journal of Aerosol Science 32 (1001), 969–980.

Middlebrook, A. M., Murphy, D. M., Thomson, D. S., 1998. Observations of organic material in individual marine particles at Cape Grim during the First Aerosol Characterization Experiment (ACE 1). Journal of Geophysical Research 103, 16475–16484.

Ming, Y., Russell, L. M., 2004. Organic aerosol effects on fog droplet spectra. Journal of Geophysical Research 109 (D10), D10206.

Murphy, D. M., Cziczo, D. J., Froyd, K. D., Hudson, P. K., Matthew, B. M., Middlebrook, A. M., Peltier, R. E., Sullivan, A., Thomson, D. S., Weber, R. J., 2006. Single-particle mass spectrometry of tropospheric aerosol particles. Journal of Geophysical Research 111 (D23), D23S32.

Murphy, D. M., Thomson, D. S., 1997. Chemical composition of single aerosol particles at Idaho Hill: Positive ion measurements. Journal of Geophysical Research 102 (D5), 6341–6352.

Murphy, D. M., Thomson, D. S., Mahoney, M. J., 1998. In situ measurements of organics, meteoritic material, mercury, and other elements in aerosols at 5 to 19 kilometers. Science 282 (5394), 1664.

O'Dowd, C. D., Lowe, J. A., Smith, M. H., 1999. Observations and modelling of aerosol growth in marine stratocumulus- case study. Atmospheric environment 33 (18), 3053–3062.

Pósfai, M., Anderson, J. R., Buseck, P. R., Sievering, H., 1995. Compositional variations of sea-salt-mode aerosol particles from the North Atlantic. Journal of Geophysical Research 100 (D11), 23063.

Seinfeld, J., Pandis, S., 1998. Atmospheric chemistry and physics: from air pollution to climate change. Wiley-Interscience.

Sellegri, K., Laj, P., Dupuy, R., Legrand, M., Preunkert, S., Putaud, J. P., 2003. Size-dependent scavenging efficiencies of multicomponent atmospheric aerosols in clouds. Journal of Geophysical Research 108 (D11), 4334.

Stevens, B., Lenschow, D. H., Vali, G., Gerber, H., Bandy, A., Blomquist, B., Brenguier, J. L., Bretherton, C. S., Burnet, F., Campos, T., Chai, S., Faloona, I., Friesen, D., Haimov, S., Laursen, K., Lilly, D. K., Loehrer, S. M., Malinowski, S. P., Morely, B., Petters, M. D., Rogers, D. C., Russell, L. M., Savic-Jovcic, V., Snider, J. R., Straub, D., Szumowski, M. J., Takagi, J., Thornton, D. C., Tschudi, M., Twohy, C. H., Wetzel, M., van Zanten, M. C., 2003. Dynamics and chemistry of marine stratocumulus-DYCOMS-II. Bulletin of the American Meteorological Society 84 (5), 579–594.

Strapp, J. W., Leaitch, W. R., Liu, P. S. K., 1992. Hydrated and dried aerosol-size-distribution measurements from the particle measuring systems FSSP-300 probe and the deiced PCASP-100X probe. Journal of Atmospheric and Oceanic Technology 9 (5), 548–555.

Straub, D. J., Lee, T., Collett Jr, J. L., 2007. Chemical composition of marine stratocumulus clouds over the eastern Pacific Ocean. Journal of Geophysical Research 112 (D4), D04307.

Sugimoto, N., Matsui, I., Shimizu, A., Uno, I., Asai, K., Endoh, T., Nakajima, T., 2002. Observation of dust and anthropogenic aerosol plumes in the Northwest Pacific with a two-wavelength polarization lidar on board the research vessel Mirai. Geophysical Research Letters 29 (19), 1901.

Twohy, C. H., Anderson, J. R., Crozier, P. A., 2005a. Nitrogenated organic aerosols as cloud condensation nuclei. Geophysical Research Letters 32 (19), L19805.

Twohy, C. H., Hudson, J. G., Yum, S. S., Anderson, J. R., Durlak, S. K., Baumgardner, D., 2001. Characteristics of cloud-nucleating aerosols in the Indian Ocean region. Journal of Geophysical Research 106, 28.

Twohy, C. H., Petters, M. D., Snider, J. R., Stevens, B., Tahnk, W., Wetzel, M., Russell, L. M., Burnet, F., 2005b. Evaluation of the aerosol indirect effect in marine stratocumulus clouds: Droplet number, size, liquid water path, and radiative impact. Journal of Geophysical Research 110 (D9), 8203.

Twomey, S., 1977. The influence of pollution on the shortwave albedo of clouds. Journal of the Atmospheric Sciences 34 (7), 1149–1152.

VanZanten, M. C., Stevens, B., Vali, G., Lenschow, D. H., et al., 2005. Observations of drizzle in nocturnal marine stratocumulus. Journal of the Atmospheric Sciences 62 (1), 88–106.

Väkevä, M., Hämeri, K., Aalto, P., 2002. Hygroscopic properties of nucleation mode and Aitken mode particles during nucleation bursts and in background air on the west coast of Ireland. J. Geophys. Res 107, 8104.

Warneck, P., 1988. Chemistry of the natural atmosphere. Academic Press, London.

Chapter 2

Oxidation of ketone groups in transported biomass burning aerosol from the 2008 Northern California Lightning Series fires

Abstract. Submicron particles were collected from June-September 2008 at the Scripps pier to investigate the composition and sources of atmospheric aerosol in an anthropogenically-influenced coastal site using aerosol mass spectrometry (AMS) and Fourier transform infrared (FTIR) spectroscopy. The two largest sources of submicron organic mass (OM) at the sampling site were identified as (1) fossil fuel combustion associated with ship and diesel truck emissions near the ports of Los Angeles and Long Beach and (2) aged smoke from large wildfires burning in central and northern California. During fire periods, forest fire OM contributed up to 74% of FTIR OM, was correlated to an AMS factor with a spectrum similar to biomass burning sources, and consisted mostly of alkane (48%), ketone (25%), and carboxylic acid groups (17%). During non-fire periods, fossil fuel com-

49

bustion contributed up to 95% of OM and consisted mostly of alkane (86%) and carboxylic acid groups (9%). The spectrum of one AMS biomass burning factor was dominated by peaks at m/z 18 and m/z 44 and correlated to wood-burning and biogenic secondary organic aerosol source spectra while the second biomass burning factor spectrum correlated to less oxidized ambient spectra (e.g. brush fire and diesel exhaust emissions). The ratio of oxygenated to primary biomass burning OM shows a clear diurnal trend with an afternoon peak, consistent with photochemical oxidation. Back trajectory analysis indicates that 2-4 day old forest fire emissions include substantial ketone groups, which have both lower O/C and lower m/z 44/OM fraction than carboxylic acid groups. Air masses with more than 4-day old emissions have higher carboxylic acid/ketone group ratios, showing that atmospheric processing of these ketone-containing organic aerosol particles results in increased m/z 44 and O/C. These observations may provide functionally-specific evidence for the type of chemical processing that is responsible for biomass burning particle composition in the atmosphere.

2.1   Introduction

Globally the two largest sources of primary organic aerosol are fossil fuel combustion (2-28 Tg C yr^{-1}) and biomass burning (31-45 Tg C yr^{-1}) (Bond et al., 2004). Model estimates of secondary organic aerosol (SOA) range from 11.2 Tg yr^{-1} (Chung and Seinfeld, 2002) to 79 Tg yr^{-1} (Kanakidou et al., 2000) making SOA from fossil fuel combustion, biogenic, and biomass burning emissions a potentially important contributor to total organic mass (OM). The strength of these sources are temporally and spatially inhomogeneous such that global organic carbon emissions cannot be attributed solely to one source. However, Bond et al. (2004) estimate that 90% of combustion-related primary carbon emissions are from biofuel and biomass burning; secondary biomass burning emissions cannot be neglected either (Gelencsér et al., 2007; Grieshop et al., 2009). In a chamber study, Grieshop et al. (2009) observed a doubling of biomass burning organic aerosol due to photochemical oxidation of only a few hours. This is especially noteworthy given that biomass burning emissions include both light-absorbing (elemental and organic carbon) and water soluble components and that biomass burning emissions are thought to be the single largest source of brown carbon, a poorly understood component of organic aerosols (Kirchstetter et al., 2004; Pósfai et al., 2004; Lukács et al., 2007; Gustafsson et al., 2009).

Previous characterization of biomass burning aerosol has focussed on identifying tracer compounds in either the gas or particle phase (e.g. methylhalides, K, levoglucosan, and acetone) (Andreae, 1983; Andreae et al., 1996; Simoneit et al., 1999; Holzinger et al., 1999; Simoneit, 2002). Some studies have extended characterization to quantifying specific compounds (e.g. levoglucosan and dehydroabietic acid, DAA) (Simoneit et al., 1999; Leithead et al., 2006) or quantifying classes of compounds (e.g. sugars) (Graham et al., 2002; Medeiros et al., 2006). These tracers are qualitatively different from those found for fossil fuel combustion (e.g. NOx, sulfate, and heavy metals) (Hameed and Dignon, 1988; Benkovitz et al., 1996; Kato and Akimoto, 2007). Biomass tracer compounds generally compose a small fraction of total OM; Leithead et al. (2006) measured organic carbon in urban and rural regions influenced by biomass burning and found that levoglu-

cosan contributed between 0.4% and 2% of measured OM, on average, while DAA contributed up to 0.2% of OM. In Brazil, levoglucosan was found to represent between 1% and 6% of total carbon while other anhydrosugars contributed up to 5% of total carbon (Graham et al., 2002). For prescribed burns over a large variety of fuel types, Sullivan et al. (2008) found that for most samples, levoglucosan contributed between 2% and 4% of total carbon, with no fuel types exceeding 10%. In measurements of biomass burning particles collected close to high-levoglucosan producing fuels, levoglucosan has been observed to exceed 10% of total suspended particle mass (including supermicron diameters), which may account for more than 30% of water extractable organic mass (Radzi bin Abas et al., 2004).

Efforts to quantitatively characterize the remaining 90-95% of smoke-related aerosol particles are fettered by the diversity and complexity of organic molecules generated by the combustion process (Jacobson et al., 2000; Kanakidou et al., 2005). This complexity makes a complete, molecular-based characterization of biomass burning aerosol extremely difficult. As an alternative, solvent extraction techniques, including quantifying water soluble organic carbon (WSOC) fraction, have been used to estimate the contribution of multi-functional or oxygenated compounds to total OM (Mayol-Bracero et al., 2002; Saarikoski et al., 2007). However, in some cases, as much as 90% of the biomass burning WSOC is uncharacterizable (Graham et al., 2002). Fang et al. (1999) found that the solvent-extractable fraction of OM collected during Malaysian forest fires was dominated by n-alkanes, alkanoic acids, and polycyclic aromatic hydrocarbons (PAHs). Oros and Simoneit (2001) used dichloromethane filter extraction and derivatization coupled with GC-MS to analyze conifer smoke particles finding that straight-chain aliphatic compounds and diterpenoid acids composed over 60% of the solvent-extractable OM. While these measurements identify the presence of biomass burning aerosol, improve source attribution in regions with multiple organic aerosol sources, and provide some insight into the chemical composition of smoke particles, they are insufficient to provide a chemical characterization of the remaining aerosol mass.

Fourier transform infrared (FTIR) spectroscopy of ambient organic aerosol has been shown to quantify close to 100% of organic mass using the sum of mea-

sured organic functional groups and by calibrating the absorptivity of common organic bonds (Maria et al., 2002, 2003; Gilardoni et al., 2007; Russell et al., 2009b). In addition to providing quantitative OM concentration–without extraction or derivatization–and regardless of the number and diversity of compounds present, FTIR spectroscopy provides functional characterization of the aerosol including saturated and unsaturated aliphatic groups, carboxylic acid groups, organic hydroxyl groups, primary amine groups, and non-acid carbonyl groups (aldehydes and ketones). Non-acid carbonyl groups are particularly relevant for biomass burning and biogenic aerosol since they are characteristic of secondary organic aerosol (SOA) formed from the oxidation of biogenic volatile organic compounds (BVOCs) (Hatakeyama et al., 1991; Hakola et al., 1994; Calogirou et al., 1999; Capouet et al., 2004). Similarly, aerosol mass spectrometry (AMS) of organic aerosol can be used to estimate the non-refractory organic mass (nr-OM) and the contribution of individual mass fragments to nr-OM. The ratios of specific m/z fragments can be used to infer chemical properties, sources, and processes associated with organic aerosol (i.e. oxygenated vs. hydrocarbon-like fragments) (Jayne et al., 2000; Jimenez et al., 2003; Zhang et al., 2005b; Lanz et al., 2007).

The large organic fraction of biomass burning emissions is subject to photochemical aging that results in important chemical changes that reduce the number of chemical signatures available to identify aerosol sources, reducing the effectiveness of using organic tracer compounds to estimate the contribution of specific aerosol types to OM. Chamber studies have shown that at 1-amu resolution, the longer biomass burning particles are photochemically oxidized, the more similar the organic mass spectrum is to oxidized organic aerosol (OOA) from fossil fuels (Grieshop et al., 2009). This trend has been observed in ambient biomass burning aerosol over West Africa (Capes et al., 2008) where measurements in the smoke plume show increasing m/z 44 (COO^+) and decreasing m/z 60 and 73 in aging smoke particles. Measurements of biomass burning in the Amazon rainforest indicate that detectable compositional changes can occur even on a diurnal time scale (Hoffer et al., 2006).

In this study, we combine measurements from two organic characterization

techniques for submicron particles collected at a coastal site (1) to separate contributions from forest fire and fossil fuel combustion to submicron organic mass by two independent methods (FTIR spectroscopy and AMS), (2) to characterize the chemical differences among these types of organic particles and the background (polluted marine) aerosol, and (3) to illustrate diurnal and multi-day changes in the forest fire particles that result from photochemical aging of a smoke plume.

2.2   Methods

2.2.1   Sample collection

Submicron particles were collected from 27 June to 17 September 2008 in La Jolla, California, as part of the Aerosol Scripps Coastal Observatory Pier Experiment (AeroSCOPE), which was designed to characterize and quantify sources of particles that contribute to aerosol in this coastal region. Day (0700 - 1900) and night (1900-0700) samples were collected through an inlet approximately 14 m above sea level (masl) on 37 mm Teflon filters (Pall Inc.) located downstream of a 1-μm sharp-cut cyclone (SCC 2.229 PM1, BGI Inc.) in a temperature controlled housing located on the Scripps Pier. A quadrupole aerosol mass spectrometer (Q-AMS, Aerodyne Inc.) was also located downstream of the sharp-cut cyclone to quantify non-refractory sulfate, nitrate, ammonium, and organic mass at 1-amu resolution following standard calibration procedures (Jayne et al., 2000; Jimenez et al., 2003).

2.2.2   FTIR and XRF analyses

Filters for Fourier transform infrared (FTIR) spectroscopy and X-ray fluorescence (XRF) were transported back to the laboratory in air-tight bags and kept at 0ºC prior to FTIR spectroscopic analysis to reduce evaporative losses of organic compounds. Duplicate back filters accompanied each sample filter for the entirety of the sampling and transportation process and were analyzed to quantify the adsorption of volatile compounds and other contamination. These back filters

showed negligible infrared absorption.

FTIR absorbance spectra of each sample and back filter were obtained non-destructively using a Bruker Tensor 27 spectrometer with RT-DLATGS detector (Bruker, Billerica, MA) and were interpreted using calibration standards and a revised algorithm based on the linear response of absorption peak area to the number of moles of organic bond present on the Teflon filters (Maria et al., 2002, 2003; Gilardoni et al., 2007; Russell et al., 2009b). Quantified functional groups include saturated aliphatic C-CH (alkane), unsaturated aliphatic C=CH (alkene), aromatic C=CH, non-acid organic hydroxyl C-OH (alcohol, including phenol), primary amine $C-NH_2$, non-acid carbonyl C=O (aldehyde and ketone), and carboxylic acid COOH. The C=O absorption peak near 1700 cm^{-1} can be attributed to aldehyde, ketone, and carboxylic carbonyl groups; however, stretching of the aldehydic hydrogen produces a pair of weak absorption bands between 2700 cm^{-1} and 2860 cm^{-1} that were not present in the spectra from ambient particles. Therefore all carbonyl absorption has been attributed to either carboxylic acid or ketone groups, depending on the estimated concentration of carboxylic COH groups. Aromatic C=C-H and alkene C=C-H groups were below detection limit in all samples and are omitted from the discussion. Organosulfate $COSO_3$ groups absorb at 876 cm^{-1} in addition to carbonate and bisulfate; however, this peak was not above the organosulfate group detection limit in any sample and is omitted from this analysis.

Following FTIR spectroscopic analysis, a subset of filters were sent to Chester Labnet (Tigard, Oregon) for X-ray fluorescence (XRF) providing concentrations of Na and heavier elements (Maria et al., 2003; Gilardoni et al., 2007; Russell et al., 2009b). Elements present above detection limit in more than 25% of the analyzed subset include Na, Si, S, K, Ca, Ti, V, Fe, Ni, Zn, Se, and Br.

2.2.3   Aerosol mass spectrometry

The Q-AMS (Aerodyne, Billerica, MA) has been described in detail elsewhere (Jayne et al., 2000; Jimenez et al., 2003). An aerodynamic lens focusses submicron particles into a narrow beam that either passes without interference

from a spinning slotted wheel (in mass spectrum mode) or is aligned with the slotted spinning wheel to allow bursts of particles into the time-of-flight sizing chamber (in time-of-flight mode). In either mode, particles are then impacted onto a heated filament (600°C), where the non-refractory components are vaporized and passed into the quadrupole mass spectrometer. Alternating between these modes every 30 sec and taking a running average every 5 min provides high time resolution measurements of particle average mass spectra and average aerodynamic size distributions of the selected fragments. Particle losses resulting in a collection efficiency (CE) less than 1 can occur during transmission into the instrument, during beam focussing, and during impaction onto the heated filament. Laboratory experiments and ambient aerosol measurements indicate that particle phase is a significant factor controlling whether particles stick to the heated filament (and are collected) or bounce off the filament (and are missed) (Quinn et al., 2006; Matthew et al., 2008). For example, dry ammonium sulfate particles have a CE of 0.2 based on laboratory studies (Alfarra et al., 2004) though ambient ammonium sulfate CE is usually greater than 0.5 (Quinn et al., 2006; Bates et al., 2005, 2008).

We have applied corrections to the measured AMS concentrations following Quinn et al. (2006) and assuming that the measured particles are internal mixtures of non-refractory components; for most measurements, the ammonium to sulfate ratio was equal to that of ammonium sulfate requiring the maximum correction (a factor of 2.2). The corrected AMS S from sulfate and filter XRF S measurements show mild agreement (r=0.6), and the least-squares fit line has a slope of 1.16, which is within the 20% uncertainty associated with each method and indicates that non-sulfate S makes up only a small fraction of the total S, if present at all. For shorter periods, the correlation between AMS and XRF sulfur exceeds 0.8, suggesting that the mild correlation coefficient is likely caused by the intermittent contributions of non-sulfate S.

2.3 Results and Discussion

2.3.1 Organic, inorganic, and elemental aerosol components

Panels in Figure 3.4 show non-refractory submicron particle components from AMS, organic functional groups from FTIR, and potassium (K) and bromine (Br) from a subset of filters analyzed by XRF. From these measurements, two chemically distinct aerosol regimes are observable, suggesting that the Scripps Pier air masses were subject to two significantly different aerosol sources during summer 2008. From 27 June to 29 July, OM was the largest non-refractory component of the submicron aerosol (Fig. 3.4a) and ketone groups were above detection limit in nearly all samples (Fig. 3.4b). K and Br were elevated above 20 ng m^{-3} and 4 ng m^{-3} (Fig. 3.4c), respectively, consistent with forest fire emissions (Andreae, 1983; Andreae et al., 1996). This composition is very different from the composition observed during the period from 30 July to 9 September when SO$_4^{2-}$ was the largest non-refractory component of the submicron aerosol and ketone groups were below detection limit in nearly all samples. During this time Br remained below 4 ng m^{-3} and K was below 20 ng m^{-3} with one exception. After 9 September, similar relative concentrations of organic and sulfate components to the first period were observed, with smaller contributions from ketone groups and lower K and Br concentrations.

2.3.2 Identified particle sources

HYSPLIT back trajectories show most air masses arrived at the sampling location from the north having traveled south along the California coast, though occasionally sampled air masses arrived from central California, from northern Mexico, or from directly west of the Scripps Pier (Rolph, 2003). Recent work has shown that the ports of Los Angeles and Long Beach are a major pollution source for the aerosol at the Scripps Pier, and air masses passing over the Long Beach region contain particles include carbon, sulfate, vanadium and nickel originating from diesel trucks and large ships in port (Ault et al., 2009). However, shortly before sampling commenced (21 June 2008), approximately 2,000 fires were ignited by lightning during a dry low-pressure system in northern California. By mid July,
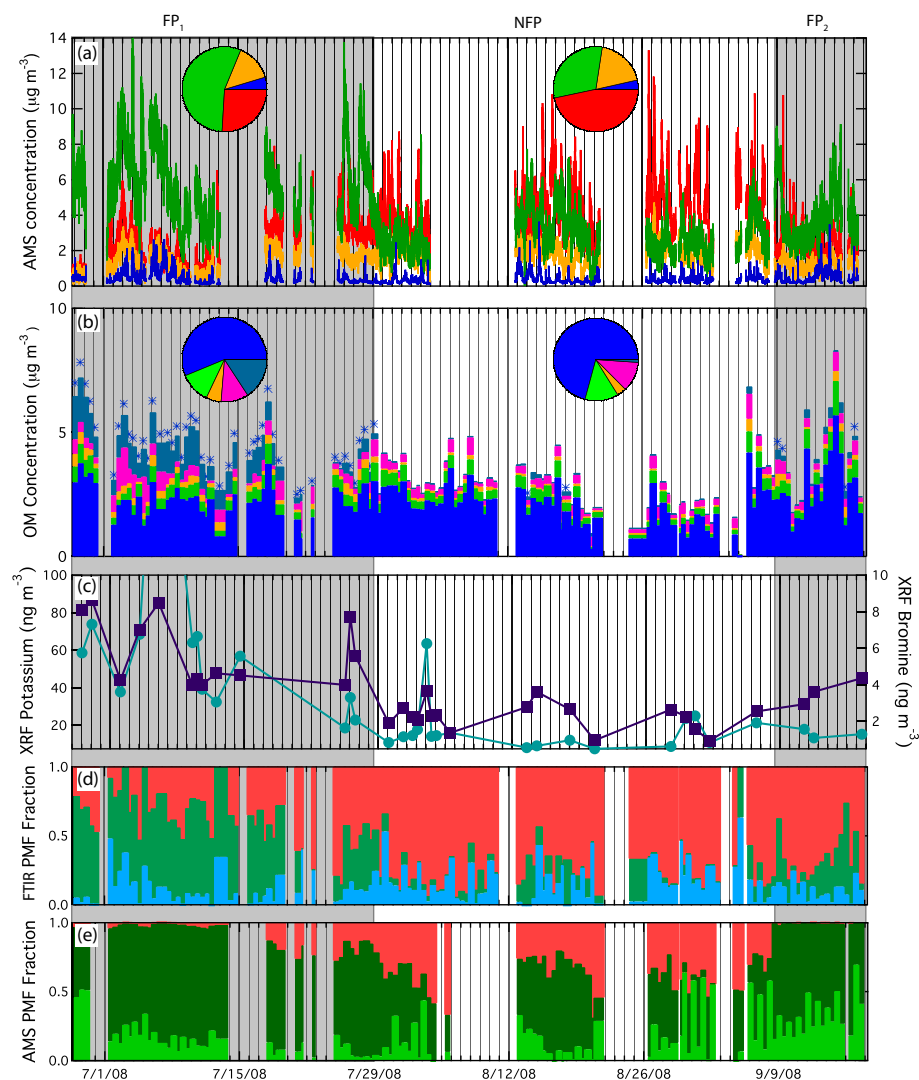
Figure 2.1: (a) Non-refractory aerosol components from AMS at 5-minute resolution including sulfate (red), ammonium (orange), nitrate (blue) and organics (green). (b) Organic functional groups from FTIR including alkane (dark blue), carboxylic acid (green), amine (orange), organic hydroxyl (pink), and ketone (teal). (c) XRF potassium (teal circles) and XRF bromine (purple squares) for the analyzed subset of FTIR filters. (d) PMF FTIR factors as fraction of total OM including BB_{FTIR} (green), FFC_{FTIR} (salmon) and polluted marine (light blue). (e) PMF AMS factors as fraction of total OM including OOA (salmon), O-BBOA (dark green), and H-BBOA (light green). Fire periods (grey regions) are defined as described in Section 3.2.

the Northern California Lightning Series fires burned over 3,000 km^2, severely impacting air quality in the Central Valley, the San Francisco Bay Area, Big Sur, and Santa Barbara county. By August 2008 most of the large fires were contained, the low pressure system passed, and smoke-related air pollution in northern and central California subsided. Because of these extremely large, persistent wildfires, the largest organic aerosol source to the Scripps Pier during this study was forest fire emissions, though particles consistent with diesel and oil combustion were also observed and dominated the submicron aerosol during non-fire periods.

On the basis of observed compositional patterns and the timing of the Northern California Lightning Series fires, we have designated 27 June to 29 July as "fire period 1" (FP$_1$), 30 July to 9 September as the "non-fire period" (NFP), and 10 September to 17 September as "fire period 2" (FP$_2$). For some portions of the discussion we have combined FP$_1$ and FP$_2$ as the "fire periods," recognizing that multiple types of particles were observed during all periods and that FP$_2$ has a larger contribution from fossil fuel combustion sources than does FP$_1$. Table 2.1 lists the average concentrations of each component for the entire campaign, for the two fire periods together, and for the non-fire period. Comparing the two, fire periods have higher total OM (4.3 μg m^{-3} vs. 2.8 μg m^{-3}) and a better agreement between the AMS and FTIR OM estimates. Fire periods also have lower sulfate (1.8 μg m^{-3} vs. 3.0 μg m^{-3}) and a significantly higher ketone group concentration (0.67 μg m^{-3} vs. 0.032 μg m^{-3}). K and Br are significantly higher during fire periods while S, V, and Ni are slightly lower.

For all measurements, FTIR OM shows mild agreement with the corrected AMS OM (Fig. 2.2, r=0.62, slope =1.1) although qualitative differences exist in the correlation during the three designated periods. FP$_1$ has the lowest FTIR/AMS OM ratio (0.90) and a mild correlation (r = 0.55) while FP$_2$ has the highest FTIR/AMS OM ratio (1.5) and the strongest correlation (r=0.62). The NFP has the weakest correlation (r = 0.37) and an average FTIR/AMS OM ratio of 1.3. These comparisons may result from chemical differences in the particle composition measured during all three periods and from applying a collection efficiency correction to all values assuming complete internal mixtures of organic mass and
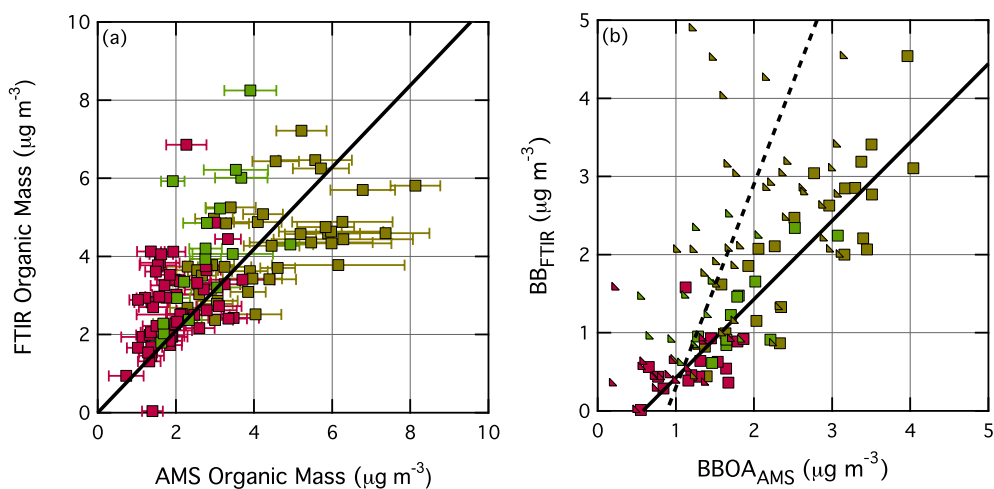
Figure 2.2: (a) FTIR OM compared with filter-averaged AMS OM corrected for bounce-related particle loss following Quinn et al. 2006 (slope = 1.1, r = 0.62). X-axis error bars represent one standard deviation of the AMS average OM. (b) BB_{FTIR} compared with BBOA (H-BBOA + O-BBOA) (squares, solid fit line: y = 1.1x-0.88, r=0.89) and with only O-BBOA (triangles, dashed fit line: y = 2.7x-2.3, r=0.52) from AMS for filters with greater than 10% BBOM. No correction for particle loss is applied to the PMF OM from AMS. Marker color in both panels indicates FP_1 (brown), FP_2 (green) and NFP (pink).

ammonium sulfate in all particles.

2.3.3 Positive Matrix Factorization of AMS and FTIR organic spectra

To quantitatively resolve the major factors that contribute to the measured mixtures of FTIR functional groups and AMS mass fragments, positive matrix factorization (PMF) was used to identify 3 factors for each data set separately and the resulting independently-derived factors were compared (Paatero and Tapper, 1994). For PMF of baselined FTIR spectra, only portions of the sample spectra with quantified peaks were included. The standard deviation of the absorbance for each wavenumber from all back filters was set as the measurement uncertainty. Results for 2, 3, 4, 5, and 6 factor solutions were explored and although the Q value (a normalized chi-square metric) was lowest for the 6-factor solution, factors

in the 5 and 6-factor solutions were correlated to one another; to avoid this type of splitting, the 4-factor solution was identified as optimal, reproducing 107% of the measured OM and organic functional groups. The 3-factor solution over-estimated the measured OM by more than 10%, which was an unsatisfactory representation of the measured concentrations and variability. The 4-factor solution was subsequently reduced to 3 factors by combining the two smallest factors (each of which show no correlations to XRF elements) into a single minor background factor. Total OM from the summed 3-factor solution compared well with the measured FTIR OM (slope = 1.09, r=0.96), demonstrating that three selected factors are sufficient to represent most of the features in the spectra. FPEAK (rotation) values from -0.4 to 0.4 were tested with the 4-factor solution but no significant difference was found among the rotations; FPEAK = 0 is presented here as a representative example.

Figure 2.3 shows the FTIR spectra and the functional group composition of each of the three FTIR PMF factors. Table 3.2 summarizes the properties of each factor. Factor 1 consists of alkane (48%), ketone (25%), carboxylic acid (17%), primary amine (8%), and organic hydroxyl groups (2%) and correlates strongly with Br (r=0.79) and mildly with K (0.68). Factor 2 comprises alkane (86%), carboxylic acid (9%), organic hydroxyl (3%), and primary amine groups (2%) and correlates strongly to S (r=0.82) and weakly to V (r=0.46). Factor 3 consists of organic hydroxyl (45%), alkane (35%), carboxylic acid (14%), and primary amine groups (6%) and does not correlate to any elemental markers measured by XRF. Panel (d) in Figure 3.4 shows the time-dependence of the three factors as fractions of FTIR OM. Factor 1 is present mainly during FP_1 and FP_2 and is largely absent during the NFP. This trend, in addition the positive correlations with K and Br and the presence of significant ketone groups, suggests that Factor 1 is associated with biomass burning from forest fires (BB_{FTIR}). The spectrum for this factor in Figure 2.3 shows two sharp peaks in the alkane absorption region at 2920 cm^{-1} and 2850 cm^{-1}, consistent with sp^3 C-H stretching absorption from methylene groups (-CH$_2$-) (Pavia et al., 2008). The sharpness of these peaks is due to a large number of repeating methylene units and may be derived from vegetative detritus (e.g. plant
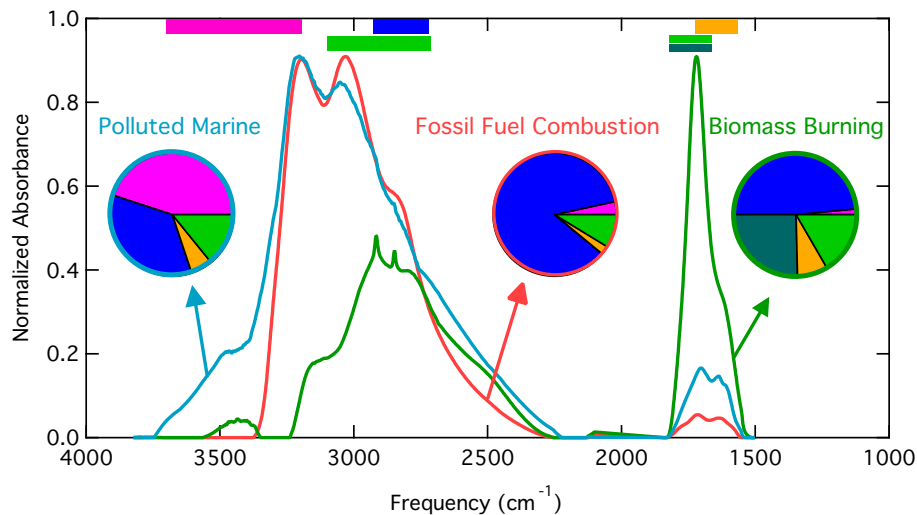
Figure 2.3: Representative FTIR normalized absorption spectra from the 3-factor PMF solution for BB_{FTIR} (green), FFC_{FTIR} (salmon) and polluted marine (light blue). Pies show the functional group composition of each factor following the colors in Fig. 3.4b.

cuticle waxes), which is commonly observed as part of biomass burning emissions (Simoneit, 1985; Fang et al., 1999; Simoneit et al., 2004; Medeiros et al., 2006). Factor 2 dominates the OM during NFP, has consistent tracer correlations with diesel and residual oil combustion, and has a strong ammonium absorption signal suggesting it is associated with fossil fuel combustion (FFC_{FTIR}, Fig. 2.3). Factor 3 shows no correlations to specific elements and is likely a combination of processed emissions and marine sources. The high organic hydroxyl fraction is consistent with previous measurements of marine organic aerosol in the southeastern Pacific (Hawkins et al., 2010), Arctic, and North Atlantic (Russell et al., 2010) oceans. In samples with little influence from FFC_{FTIR}, m/z 79 fraction of AMS OM (a fragment associated with MSA in Phinney et al. (2006) and Zorn et al. (2008)) is strongly correlated to organic hydroxyl fraction of OM (r = 0.95 for samples with less than 20% FFC_{FTIR}), supporting some influence of marine emissions on the composition of Factor 3. However, the small fractional contribution of this factor to the measurements during the project means that the marine emissions are likely not fully resolved from other pollution sources. Consequently, this factor is labeled "polluted marine."

PMF analysis of AMS organic spectra averaged to 30-minute resolution was explored for 2, 3, 4, 5, and 6 factor solutions along with FPEAK values from -0.4 to 0.4 following the procedure in Lanz et al. (2007). The source spectra determined from PMF were correlated to all spectra available on the AMS spectral database (Ulbrich, I.M., Lechner, M., and Jimenez, J.L. AMS Spectral Database. URL: http://cires.colorado.edu/jimenez-group/AMSsd/) described in Ulbrich et al. (2009) to determine which solutions produced spectra consistent with previous observations. For solutions of 2-6 factors, spectra from FPEAK = 0.4 had the highest correlations to literature spectra. Beyond 3 factors, additional factors showed correlations to one another indicative of factor splitting (Ulbrich et al., 2009). Therefore the 3-factor solution with FPEAK = 0.4 was selected to best represent the data chemically and quantitatively (reconstructed and measured OM had slope = 0.98 and r = 0.99). Figure 2.4 shows the normalized spectra of AMS factors 1-3; correlations to reference spectra and inorganic components are included in Table 3.2. The strength of Factor 1 is correlated to AMS sulfate (r = 0.64) and XRF Ni (r = 0.36) and is negatively correlated to BB_{FTIR}, K, and Br. Although the spectrum for this factor does not correlate strongly to any previously published spectra, correlating only m/z 45 and larger fragments results in strong correlations to aged rural aerosol (r=0.86), bovine aerosol (r=0.87), and aerosol measured in the summer in the San Joaquin Valley (r=0.87). M/z 44 is a prominent fragment, with small contributions from m/z 43, 55, and 57 resulting in this factor's assignment as OOA (Zhang et al., 2005c). The strength of Factor 2 is correlated to Br (r = 0.90), K (r = 0.57), and BB_{FTIR} (r = 0.81). The spectrum for Factor 2 is correlated to fir smoldering emissions (r=0.99), beech smoldering emissions (r=0.99), and fulvic acid (r=0.98) when all m/z are considered. For m/z 45 and larger, the spectrum is correlated to OOA (r=0.93), and terpinolene (r=0.89), myrcene (r=0.94), and m-xylene SOA particles (r=0.91). The strength of Factor 3 also correlates to Br (r = 0.46), K (r = 0.49), and BB_{FTIR} (r = 0.48) though correlations are weaker than for Factor 2. The spectrum of Factor 3 correlates to brush fire aerosol (r=0.91), San Joaquin Valley summer aerosol (r=0.95), and diesel exhaust (r=0.95). Factors 2 and 3 both have characteristics of biomass burn-

ing aerosol though Factor 2 is more similar to biogenic SOA and has a much larger contribution from m/z 44. Factor 3 is less oxygenated and shares similar fragments (43, 55, 57) with urban fossil fuel emissions. Therefore, Factors 2 and 3 are labeled together as "BBOA" with one "oxidized biomass burning organic aerosol" factor (O-BBOA) and one "hydrocarbon biomass burning organic aerosol" factor (H-BBOA). Figure 2.5a shows the difference between the normalized O-BBOA and H-BBOA spectra for each m/z that contributes more than 0.2% to the total organic signal. The largest differences are for m/z 17, 18, and 44 (positive) and m/z 27, 29, and 41 (negative). These differences support the assignment of O-BBOA as the more oxygenated of the two since m/z 18 (H_2O^+) and 44 (COO^+) are associated with dehydration and oxygenated fragments, and m/z 27 (CH_2CH^+) and 41 ($CH_2CH_2CH^+$) are associated with primary emissions from wood burning (Alfarra et al., 2007; Schneider et al., 2006). Small decreases in m/z 55, 56, and 58 also indicate oxidation or fragmentation of the larger hydrocarbon chains in O-BBOA. Recent comparisons between organic mass fragments and organic functional groups across multiple projects show general agreement on the assignments of m/z 44 and m/z 57 as carboxylic acid and alkane groups (Russell et al., 2009a). Figure 2.5b shows an afternoon peak in the ratio of the two types of BBOA, consistent with photochemical oxidation causing some of the observed differences in the two AMS mass spectra.

Figure 2.2b shows BB_{FTIR} compared with the summed BBOA. The two independent estimates of biomass burning aerosol correlate more strongly using the sum of the two types of BBOA than either type alone with BB_{FTIR} (r = 0.89) and have a slope of 1.1. Spectral similarities between H-BBOA and urban emissions like diesel exhaust indicate that H-BBOA may include local fossil fuel combustion emissions. However, BB_{FTIR} compared with only O-BBOA has a much weaker correlation (r=0.52) and slope = 2.7 suggesting that, especially during BB events, H-BBOA is likely to have only a small amount of contamination from fossil fuel combustion. During NFP, the contribution of hydrocarbon fossil fuel combustion emissions to H-BBOA is potentially significant and may account for the negative intercept in the least-squares fit in Figure 2.2b. To our knowledge, this is the first
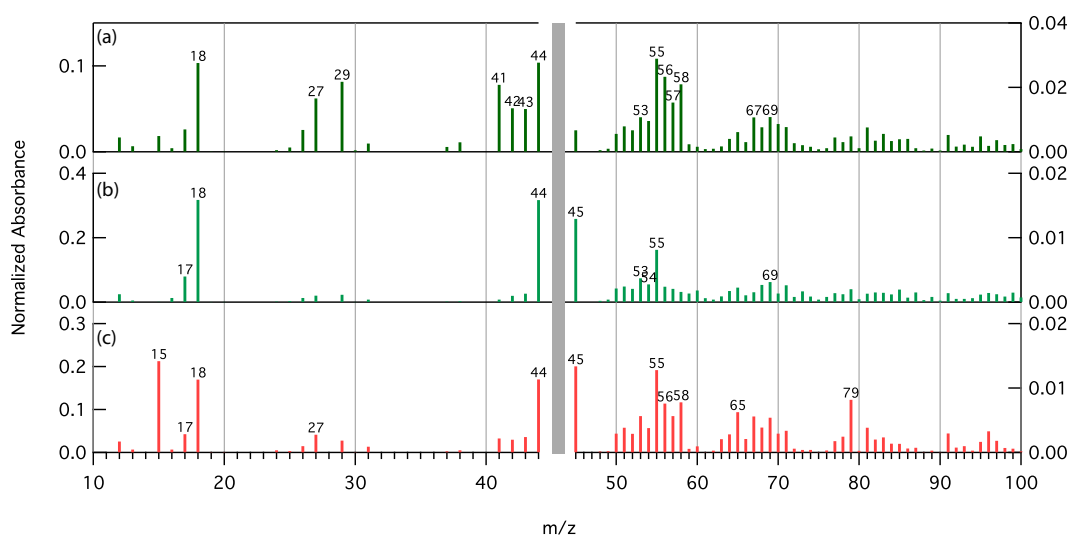
Figure 2.4: Representative AMS normalized mass spectra from the 3-factor PMF solution for (a) the less oxidized BBOA (H-BBOA), (b) the more oxygenated BBOA (O-BBOA), and (c) OOA. Left and right panels show fragments less than and greater than m/z 45, respectively.
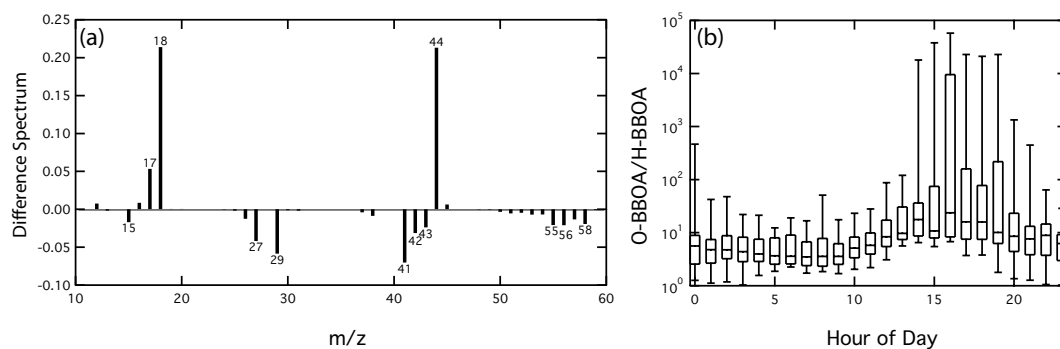
Figure 2.5: (a) Difference in normalized signal at each m/z (O-BBOA - H-BBOA) contributing greater than 0.2% to each spectrum. (b) Hourly averaged ratio of O-BBOA/H-BBOA for FP_1.

time organic mass from two independent measurements has been compared following factor analysis. This level of agreement between two independent OM or OC measurements is higher than found previously in comparing two OC measurements using the same technique (Turpin and Lim, 2001). This good agreement suggests that the collection efficiency of BBOA is close to 1 and that the two methods of OM quantification perform similarly for the types of chemical mixtures that constitute forest fire aerosol. The apparent overlap of the two instrument size ranges also suggests low particle mass above 700 nm vacuum aerodynamic diameter (VAD).

2.3.4 Distinguishing forest fire from fossil fuel combustion organic aerosol

Forest fire emissions from fires in Northern California contributed an average of 40% of OM in fire periods of 2008, with characteristic correlations to elemental markers (K, Br) and a frequent contribution of ketone groups observed in previous woodsmoke (Russell et al. 2009) and biomass burning aerosol (Liu et al., 2009). During NFP, fossil fuel combustion (FFC_{FTIR}) contributed 75% of OM and had distinctly different composition from both biomass burning and polluted marine aerosol. The traditional distinction of BBOA from HOA, OOA1, and OOA2 has rested on the presence of m/z 60 and 73 (Lanz et al., 2007; Zhang et al., 2007; Capes et al., 2008) although residual saccharides from cellulose combustion (levoglucosan) that produce those fragments and serve as tracers have been quantified as only a few percent of OM that may be lost in aging smoke plumes. The new result here is that BBOA is not just more or less oxygenated than fossil fuel combustion aerosol (Grieshop et al., 2009) but that it contains a significant fraction of ketone groups. The presence of ketone groups may result from more numerous alkene groups in non-aromatic ring structures present in biogenic VOCs that are coemitted from forests during burning events (Greenberg et al., 2006) than in fossil fuel VOC emissions. For example, pinonaldehyde, pina ketone, 4-methyl-3-cyclohexenone, and limonon aldehyde have all been identified as major products of α-pinene, β-pinene, terpinolene, or limonene oxidation and all contain ketone groups–in addition to organic hydroxyl or aldehyde groups (Hatakeyama

et al., 1991; Hakola et al., 1994; Calogirou et al., 1999).

PMF has been used with FTIR spectra in recent work to identify OM from oil combustion, woodsmoke, processed urban combustion, marine organic, and background aerosol (Russell et al., 2009b; Liu et al., 2009; Russell et al., 2010; Hawkins et al., 2010; Bahadur et al., 2010) based on the functional group composition of the factor, the sampling conditions and known sources, and the correlations to XRF tracer elements. Fossil fuel combustion particles identified in other regions typically include 40-70% alkane groups and 20-30% carboxylic acid groups (Russell et al., 2009b; Liu et al., 2009). On the other hand, PMF of measurements in the Gulf of Mexico resulted in a woodsmoke factor that was 12% to 32% non-acid carbonyl groups and 27% to 52% alkane groups, depending on the number of factors chosen for the solution (Russell et al., 2009b). This factor correlated mildly with K and Br in addition to several heavy metals. Because this factor was associated with urban wood burning, it is expected that it would be correlated to tracers commonly associated with fossil fuel combustion. However, no other factors included non-acid carbonyl groups above detection limits. Similarly, FTIR measurements in Mexico also included a factor with significant non-acid carbonyl group contribution (26% to 47%) that was elevated during periods of elevated K, levoglucosan, and acetonitrile consistent with biomass burning (Liu et al., 2009; Gilardoni et al., 2009). The sharp methylene peaks in the biomass burning factor presented here are unique among the FTIR biomass burning factor spectra, consistent with the hypothesis that they are POA from plant cuticle wax detritus which has been associated with large wildfires but not with residential wood or trash burning or smaller fires (Simoneit, 1985; Fang et al., 1999; Medeiros et al., 2006).

2.3.5 Chemical and physical changes associated with aging forest fire aerosol

To investigate the chemical changes associated with aging of California wild-fire aerosol, potential source contribution function (PSCF) analysis was applied to air masses sampled during FP_1 for high ketone group fraction ($> 20\%$) and high

carboxylic acid group fraction (> 12%) (Fig. 2.6a,b). PSCF analysis combines a gridded geographical domain with air mass back trajectories and measured concentrations to determine the probability that each particular grid box contains a source of the measured component (Zeng and Hopke, 1989). In Figure 2.6a, the high probability regions for ketone groups are located near the sampling site and off the coast of California between San Francisco and San Diego. This region experienced frequent intense plumes of smoke both from the fires in northern California and in Big Sur. Figure 2.6c shows several examples of trajectories with high ketone group fractions that crossed smoke plumes within 2 days of arriving at the sampling site. These particular trajectories crossed directly over the Basin Fire burning near Big Sur approximately 1-1.5 days before arriving at the pier. By contrast, the PSCF for high carboxylic acid group fractions shows high source probability near the far northern California coast and in the region southwest of the sampling site. The latter high probability region is due to trajectories like those shown in Figure 2.6d that followed indirect paths from the fires to the pier or were forced south of the pier by strong offshore winds before being blown back to the pier. Trajectories in Figure 2.6d reached the sampling site more than 3 days after crossing a fire or a smoke plume; trajectories from 10 and 11 July are examples of trajectories that were forced south before arriving at the pier. AMS time-of-flight mass distributions provide additional evidence that these air masses represent young (less than 2 days since emission) and aged (more than 4 days since emission) smoke particles (Fig. 2.7). Measurements of organic mass fragments (m/z 43, 44, and 55) from 1-day and 4-day old smoke particles show an increase in the peak diameter up to 80 nm (m/z 43) and a decrease in mass at 100 nm coinciding with an increase in mass at 400 nm (Fig. 2.7). Such a shift in the mean size has been observed in previous measurements of an aging biomass plume (Capes et al., 2008) where coagulation was determined to dominate the evolution of the particle number size distribution.

The submicron organic aerosol measurements presented here indicate that the ketone group signature of forest fire particles persists even in moderately aged particles but is weak or absent in measurements of highly aged smoke (greater
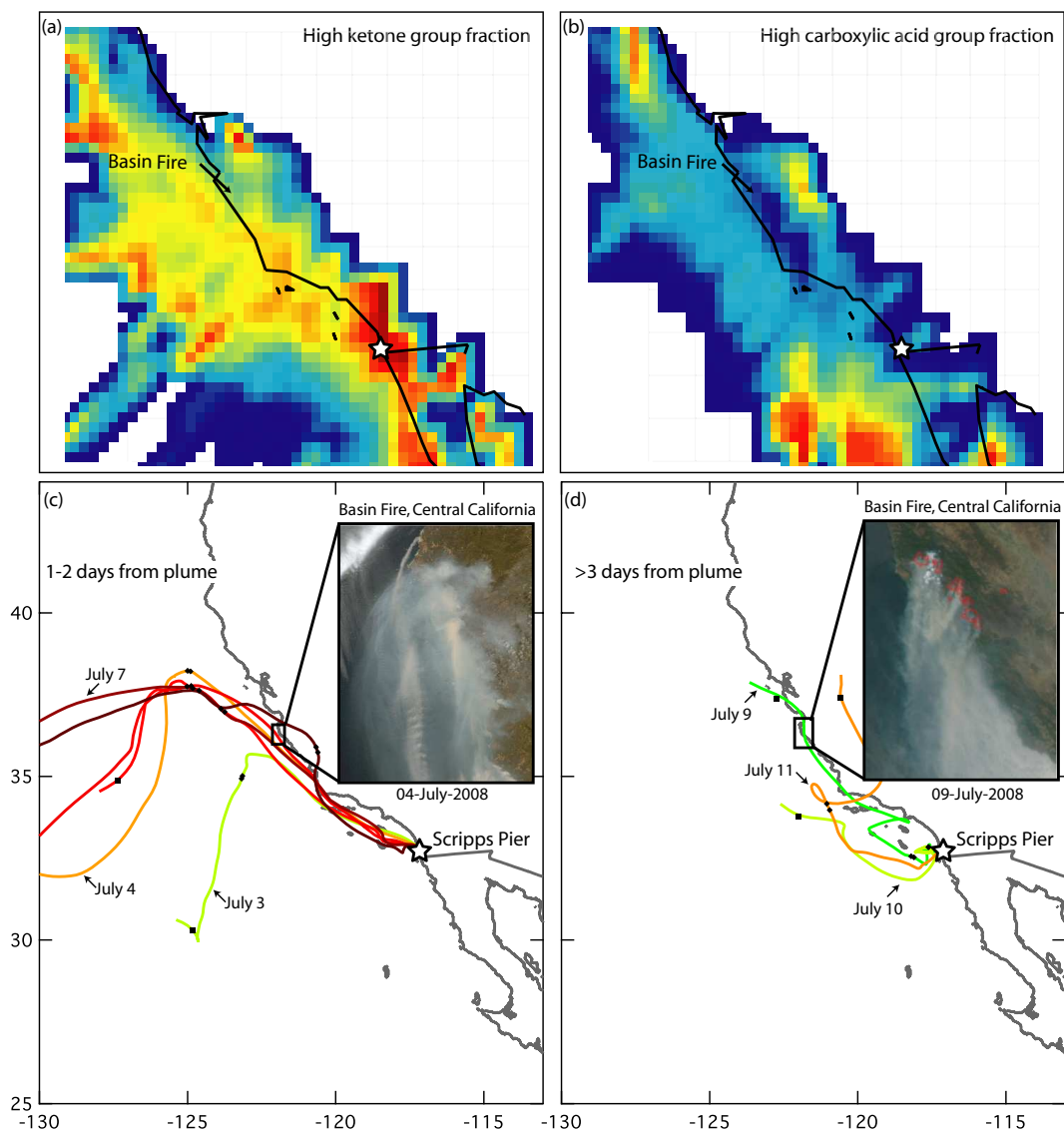
Figure 2.6: Potential Source Contribution Function (PSCF) for (a) high ketone group samples and (b) high carboxylic acid group samples during FP$_1$. (c) 4-day back trajectories for air masses reaching the sampling site between 3 July and 7 July 2008 with smoke emissions less than 2 days old. (d) 4-day back trajectories for air masses reaching the sampling site between 9 July and 12 July 2008 with smoke emissions more than 4 days old. Markers on the back trajectories indicate every 48 hours. Images in panels (c) and (d) were obtained from NASA's Terra satellite.
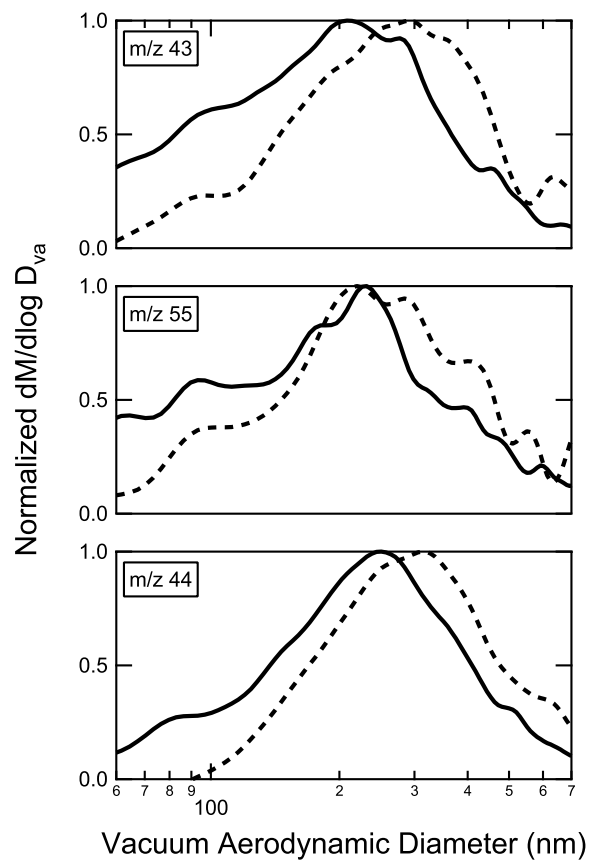
Figure 2.7: Normalized mass distributions for 1 (solid) and 4-day (dashed) old smoke plumes from AMS ToF measurements.

than 4 days) (Fig. 2.8). The carboxylic acid to ketone group ratio increases from 0.35±0.11 for samples within 2 days of emission to 1.3±0.6 for samples with greater than 4 days since emission. The increase in carboxylic acid/ketone group results from both a decrease in the ketone group fraction (Fig. 2.8b) and an increase in the carboxylic group fraction without an accompanying increase in BB_{FTIR} (Fig. 2.8a), consistent with particle phase formation of carboxylic acid and loss of ketone groups rather than additional SOA formation. Equation 2.1 shows the measured relationship between carboxylic acid to ketone groups and estimated smoke age, which are correlated mildly (r=0.72).

$$M_{COOH}/M_{C=O} = (0.2 \pm 0.06)t - (0.03 \pm 0.2) \tag{2.1}$$

where M_{COOH} and $M_{C=O}$ are the mass of carboxylic acid and ketone groups, respectively, and t is the estimated smoke age in days. A similar relationship was observed for the ratio of O-BBOA to H-BBOA. The ratio increases from 3.3±1.2 for samples within 2 days of emission to 11±0.77 for samples with more than 4 days since emission. Eq. 2.2 shows the measured relationship between O-BBOA and H-BBOA and estimated smoke age, which also has a mild though lower correlation (r=0.55).

$$M_{O-BBOA}/M_{H-BBOA} = (2 \pm 1)t - (0.5 \pm 3) \tag{2.2}$$

where M_{O-BBOA} and M_{H-BBOA} are the mass of oxygenated BBOA and hydrocarbon BBOA, respectively. Similarly, the hourly rate of oxidation of H-BBOA to O-BBOA can be estimated from the hourly average ratio of O-BBOA to H-BBOA, between 0900 and 1600 (Fig. 2.5b, Eq. 2.4).

$$M_{O-BBOA}/M_{H-BBOA} = (3 \pm 0.3)h - (30 \pm 4) \tag{2.3}$$

where h is the hour of the day. Using the same time unit (days) as Eqs. 2.1 and 2.2,

$$M_{O-BBOA}/M_{H-BBOA} = (70 \pm 8)t - (30 \pm 4) \tag{2.4}$$

The daily rate of increase in O-BBOA/H-BBOA from the diurnal average is more

than 30 times the rate in Eq. 2.2; extrapolating the oxidation rate from diurnal measurements to 4-day old aerosol results in much higher O-BBOA to H-BBOA ratios than were observed in actual 4-day old smoke particles, indicating that dilution and losses play a significant role in the net chemical changes to the aging aerosol. Uniform marine stratocumulus clouds are visible in images from NASA's Terra satellite along the coastal area near the sampling site during the measurement period increasing the likelihood that cloud processing is responsible for a significant fraction of the observed oxidation, though separating the contributions of photochemistry and cloud processing to the observed oxidation rates is not possible given the lack of airborne observations to characterize the meteorology.

The observed reduction in ketone groups simultaneously to the production of carboxylic acid groups in forest fire emissions during their processing in the atmosphere is consistent with the formation of carboxylic acid groups (O/C=2) coincident with loss of ketone groups (O/C=1) producing increasing O/C and m/z 44 fraction of OM. Ketone loss has previously been observed in controlled photochemical aging experiments (Mang et al., 2008), which demonstrate that photolysis of ketone groups in limonene SOA is a significant pathway for aging biogenic OM. Mang et al. (2008) attribute the simultaneous loss of ketone groups and production of CO to the Norrish type-I mechanism (Norrish and Bamford, 1936) that produces two alkyl radicals and one molecule of CO for each photolyzed parent ketone molecule. Grieshop et al. (2009) have shown that measurable chemical differences exist during oxidation of biomass burning particles, specifically increasing m/z 44 signal (up to 10% of the organic signal) and O/C (up to 0.5). Similarly, ambient measurements in West Africa following a smoke plume show that the contribution of m/z 44 increased from 7.4% in fresh biomass burning spectra to 14% in aged spectra (Capes et al., 2008). It should be noted that O/C can also increase from a reduction in the alkane group fraction due to oxidation, fragmentation, and volatilization of newly formed VOCs. However, the measured alkane fraction actually increased from 0.42 ± 0.06 to 0.60 ± 0.04 between air masses with 2-day and 4-day old smoke particles due to mixing of fossil fuel combustion emissions (which have high alkane group fractions) with forest fire emissions. Measurements
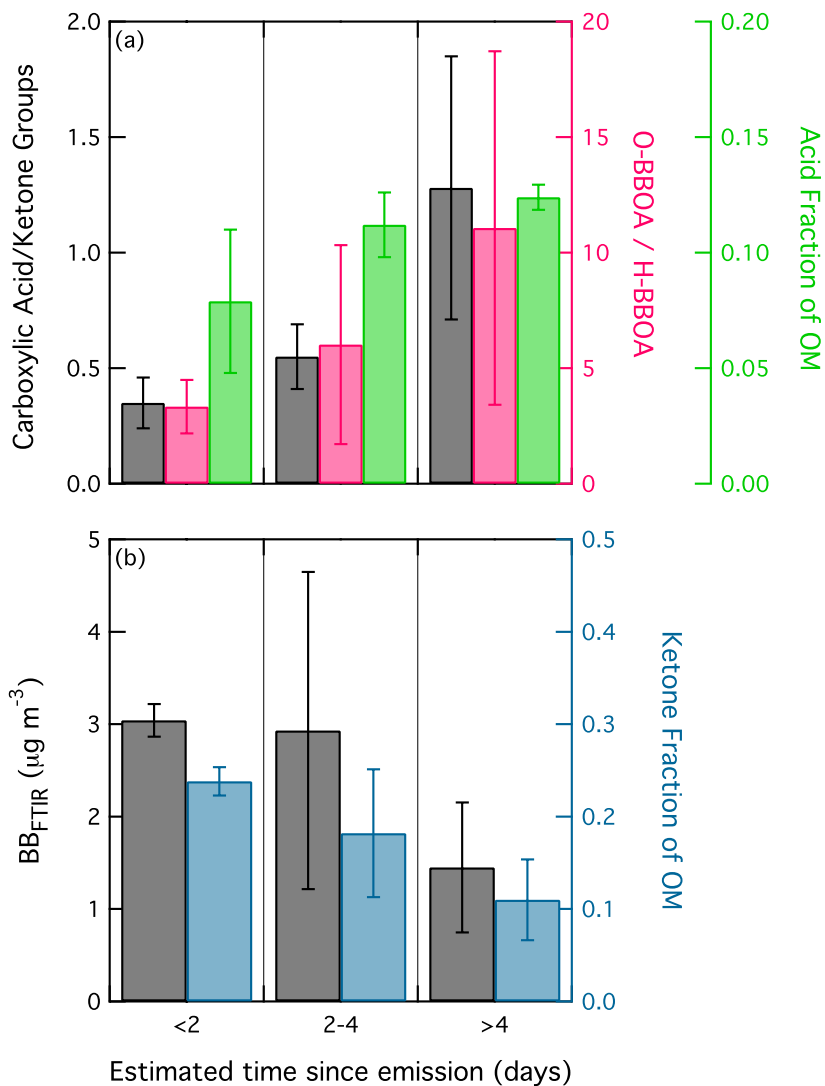
Figure 2.8: (a) Carboxylic acid/ketone group ratio (black), O-BBOA/H-BBOA ratio (pink), and carboxylic acid group fraction of OM (light green) for samples with estimated less than 2 days, between 2 and 4 days, and greater than 4 days since emission. (b) BB$_{FTIR}$ (black) and ketone group fraction of OM (teal) for the same samples. Vertical error bars indicate one standard deviation of the average.

from Barrow, Alaska, show that in smoke plumes older than 5 days, ketone groups are below detection limit while carboxylic acid groups dominate the oxygenated OM (Shaw et al., 2010). Therefore, for very long range transport, ketone groups may not be the best indicator of forest fire emissions as the aerosol has aged sufficiently to look like OOA from fossil fuel combustion, consistent with Grieshop et al. (2009).

2.4 Conclusion

Measurements of organic functional groups and collocated measurements of non-refractory aerosol were used to separate contributions from forest fire and fossil fuel combustion aerosol to OM during summer 2008 in California. Similarities to previously reported wood smoke and biomass burning aerosol are consistent with the compositions of the factors identified here. We report the first observations of substantial ketone groups (25%) in forest fire aerosol, which have both lower O/C and lower m/z 44/OM fraction than carboxylic acid groups. The similarity of the AMS spectrum of the dominant PMF-based factor to laboratory generated biogenic VOC oxidation products suggests that much of the measured organic aerosol is SOA from biomass burning sources rather than primary organic aerosol.

Changes in compositional measured in FTIR spectra were complementary to diel changes observed in AMS mass spectra including an increase in m/z 44 fraction and a decrease in m/z 27, 41, and 55 though the average daily increase in oxygenated BBOA was much greater than the rate estimated from observations of 2, 3, and 4-day old smoke particles. Atmospheric processing of these ketone-containing organic aerosol particles likely forms carboxylic acid groups and removes ketone groups, resulting in increased m/z 44 and O/C. These observations may provide an explanation for the observed increase in both O/C and m/z 44 in chamber studies of wood smoke oxidation–by formation of carboxylic acid groups and loss of ketone groups–using quantitative measurements of organic functionality of ambient aging forest fire particles.

2.5 Acknowledgments

Chapter 2, in full, has been submitted for publication to Atmospheric Environment 2010. Hawkins, L. N. and Russell, L. M. (2010), Oxidation of ketone groups in transported biomass burning aerosol from the 2008 Northern California Lightning Series fires. The dissertation author was the primary investigator and author of this paper.

Table 2.1: Mean and Standard Deviation of Measured OM, Sulfate, Organic Functional Groups, O/C, and Elemental Concentrations for AeroSCOPE and for Fire and Non-fire Periods.

	AeroSCOPE 2008	Fire Periods	Non-fire Period
FTIR OM (μg m^{-3})	3.6±1.4	4.3±1.3	2.8±1.1
AMS OM (μg m^{-3})	3.0±1.6	4.0±1.6	2.0±0.72
AMS SO$_4^{2-}$ (μg m^{-3})	2.4±0.93	1.8±0.68	3.0±0.75
FTIR Organic Functional Groups (μg m^{-3})			
Alkane	2.2±0.87	2.4±0.89	2.0±0.80
Carboxylic acid	0.43±0.19	0.50±0.19	0.37±0.16
Primary amine	0.17±0.12	0.24±0.12	0.10±0.07
Organic hydroxyl	0.39±0.26	0.45±0.31	0.33±0.18
Ketone	0.35±0.48	0.67±0.50	0.032±0.071
FTIR O/C (atomic)	0.26±0.12	0.31±0.12	0.22±0.11
FTIR OM/OC (mass)	1.55±0.17	1.62±0.16	1.49±0.15
XRF Elements (ng m^{-3})			
Br	3.8±2.1	5.4±1.9	2.3±0.77
Ca	7.0±3.7	7.4±3.3	6.7±4.1
Fe	3.0±2.2	3.0±1.6	3.0±2.8
K	34±41	53±52	17±13
Na	150±86	130±56	160±110
Ni	1.4±0.87	1.2±0.43	1.6±1.1
S	100±220	930±170	1100±240
Se	0.38±0.088	0.42±0.070	0.34±0.087
Si	13±29	11±18	15±36
Ti	0.60±0.63	0.67±0.78	0.45±0.12
V	2.8±1.0	2.5±0.79	3.1±1.2
Zn	2.7±3.6	2.4±2.7	2.9±4.4

Table 2.2: Organic Functional Group Composition, Elemental Correlations, and Reference Spectra Correlations of PMF Factors

	FTIR factors		
	Biomass Burning	Fossil Fuel Combustion	Polluted Marine
FTIR Organic Functional Groups			
Alkane	48%	86%	45%
Carboxylic acid	17%	9%	14%
Primary amine	8%	2%	6%
Organic hydroxyl	2%	3%	45%
Ketone	25%	0%	0%
Elemental Correlations (r, r>0.4 only)			
K	0.68		
Br	0.79		
S		0.82	
V		0.46	

Table 2.2: cont'd

	AMS factors		
	Oxidized BBOA	Hydrocarbon BBOA	OOA
Reference Spectra Correlations (r, r > 0.8 only)			
All m/z	fir smoldering[a] (0.99)	brush fire[b] (0.95)	
	beech smoldering[c] (0.99)	San Joaquin Valley[d] (0.95)	
	fulvic acid[e] (0.98)	diesel exhaust[f] (0.95)	
	OOA[g] (0.94)	OOA[h] (0.95)	
	oak smoldering[i] (0.94)	urban Vancouver[j] (0.94)	
m/z > 45	terpinolene SOA[k] (0.94)	urban Vancouver[j] (0.97)	San Joaquin Valley[d] (0.87)
	myrcene SOA[l] (0.93)	OOA[m] (0.96)	bovine[n] (0.87)
	OOA-I[g] (0.93)	brush fire[b] (0.94)	bovine[o] (0.86)
	terpinolene SOA[p] (0.92)	aged rural (low CO)[q] (0.93)	aged rural (low CO)[q] (0.86)
	m-xylene SOA[r] (0.91)	myrcene SOA[l] (0.93)	aged rural (high CO)[s] (0.86)
Elemental Correlations (r, r>0.4 only)			
K	0.57	0.49	
Br	0.9	0.46	
AMS sulfate (r)			0.64

Reference spectra: [a,c,i]Weimer et al. (2008), [b,k,l,p,r]Bahreini et al. (2005), [d,n,o]Sorooshian et al. (2008), [e]Alfarra (2004), [f]Sage et al. (2008), [g]Lanz et al. (2007), [h]Zhang et al. (2005a), [j,q,s]Alfarra et al. (2004), [m]Lanz et al. (2008).

References

Alfarra, M. R., Coe, H., Allan, J. D., Bower, K. N., Boudries, H., Canagaratna, M. R., Jimenez, J. L., Jayne, J. T., Garforth, A. A., Li, S. M., et al., 2004. Characterization of urban and rural organic particulate in the Lower Fraser Valley using two Aerodyne Aerosol Mass Spectrometers. Atmospheric Environment 38 (34), 5745–5758.

Alfarra, M. R., Prévôt, A. S., Szidat, S., Sandradewi, J., Weimer, S., Lanz, V. A., Schreiber, D., Mohr, M., Baltensperger, U., 2007. Identification of the mass spectral signature of organic aerosols from wood burning emissions. Environmental Science &Technology 41 (16), 5770.

Alfarra, R., 2004. Insights Into Atmospheric Organic Aerosols Using An Aerosol Mass Spectrometer. Ph.D. thesis, Univ. of Manchester.

Andreae, M. O., 1983. Soot carbon and excess fine potassium: Long-range transport of combustion-derived aerosols. Science 220 (4602), 1148.

Andreae, M. O., Atlas, E., Harris, G. W., Helas, G., De Kock, A., Koppmann, R., Maenhaut, W., Manϕ, S., Pollock, W. H., Rudolph, J., et al., 1996. Methyl halide emissions from savanna fires in southern Africa. Journal of Geophysical Research–Atmospheres 101 (D19), 23603–23613.

Ault, A. P., Moore, M. J., Furutani, H., Prather, K. A., 2009. Impact of Emissions from the Los Angeles Port Region on San Diego Air Quality during Regional Transport Events. Environmental Science &Technology 43 (10), 3500–3506.

Bahadur, R., Uplinger, T., Russell, L. M., Sive, B. C., Cliff, S. C., Millet, D. B., Goldstein, A., Bates, T. S., 2010. Phenols in northeastern U. S. aerosol particles from lignin and its products in seawater. http://aerosols.ucsd.edu/publications.html, in review.

Bahreini, R., Keywood, M. D., Ng, N. L., Varutbangkul, V., Gao, S., Flagan, R. C., Seinfeld, J. H., Worsnop, D. R., Jimenez, J. L., 2005. Measurements of secondary organic aerosol (SOA) from oxidation of cycloalkenes, terpenes, and m-xylene using an Aerodyne aerosol mass spectrometer. Environmental Science &Technology 39 (15), 5674–5688.

Bates, T. S., Quinn, P. K., Coffman, D., Schulz, K., Covert, D. S., Johnson, J. E., Williams, E. J., Lerner, B. M., Angevine, W. M., Tucker, S. C., et al., 2008. Boundary layer aerosol chemistry during TexAQS/GoMACCS 2006: Insights into aerosol sources and transformation processes. Journal of Geophysical Research–Atmospheres 113, doi:10.1029/2008JD010023.

Bates, T. S., Quinn, P. K., Coffman, D. J., Johnson, J. E., Middlebrook, A. M., 2005. Dominance of organic aerosols in the marine boundary layer over the Gulf of Maine during NEAQS 2002 and their role in aerosol light scattering. Journal of Geophysical Research–Atmospheres 110, doi:10.1029/2005JD005797.

Benkovitz, C. M., Trevor Scholtz, M., Pacyna, J., Tarrasón, L., Dignon, J., Voldner, E. C., Spiro, P. A., Logan, J. A., Graedel, T. E., 1996. Global gridded inventories of anthropogenic emissions of sulfur and nitrogen. Journal of Geophysical Research–Atmospheres 101, 29–29.

Bond, T. C., Streets, D. G., Yarber, K. F., Nelson, S. M., Woo, J. H., Klimont, Z., 2004. A technology-based global inventory of black and organic carbon emissions from combustion. Journal of Geophysical Research–Atmospheres 109 (D14), 14203–14203.

Calogirou, A., Larsen, B. R., Kotzias, D., 1999. Gas-phase terpene oxidation products: a review. Atmospheric Environment 33 (9), 1423–1439.

Capes, G., Johnson, B., McFiggans, G., Williams, P. I., Haywood, J., Coe, H., 2008. Aging of biomass burning aerosols over West Africa: Aircraft measurements of chemical composition, microphysical properties, and emission ratios. Journal of Geophysical Research–Atmospheres 113, doi:10.1029/2008JD009845.

Capouet, M., Peeters, J., Noziere, B., Müller, J. F., 2004. Alpha-pinene oxidation by OH: simulations of laboratory experiments. Atmospheric Chemistry and Physics 4 (9/10), 2285–2311.

Chung, S. H., Seinfeld, J. H., 2002. Global distribution and climate forcing of carbonaceous aerosols. Journal of Geophysical Research–Atmospheres 107 (19), 4407.

Fang, M., Zheng, M., Wang, F., To, K. L., Jaafar, A. B., Tong, S. L., 1999. The solvent-extractable organic compounds in the Indonesia biomass burning aerosols-characterization studies. Atmospheric Environment 33 (5), 783–795.

Gelencsér, A., May, B., Simpson, D., Sánchez-Ochoa, A., Kasper-Giebl, A., Puxbaum, H., Caseiro, A., Pio, C., Legrand, M., 2007. Source apportionment of PM2. 5 organic aerosol over Europe: Primary/secondary, natural/anthropogenic, and fossil/biogenic origin. Journal of Geophysical Research–Atmospheres 112, doi:10.1029/2006JD008094.

Gilardoni, S., Russell, L. M., Sorooshian, A., Flagan, R. C., Seinfeld, J. H., Bates, T. S., Quinn, P. K., Allan, J. D., Williams, B., Goldstein, A. H., et al., 2007. Regional variation of organic functional groups in aerosol particles on four US east coast platforms during the International Consortium for Atmospheric Research on Transport and Transformation 2004 campaign. Journal of Geophysical Research–Atmospheres 112, doi:10.1029/2006JD007737.

Gilardoni, S., Shang, L., Takahama, S., Russell, L. M., Allan, J. D., Steinbrecher, R., Jimenez, J. L., Decarlo, P. F., Dunlea, E. J., Baumgardner, D., 2009. Characterization of organic ambient aerosol during MIRAGE 2006 on three platforms. Atmospheric Chemistry and Physics Discussionsions 9 (2), 6617–6655.

Graham, B., Mayol-Bracero, O. L., Guyon, P., Roberts, G. C., Decesari, S., Facchini, M. C., Artaxo, P., Maenhaut, W., Koll, P., Andreae, M. O., 2002. Water-soluble organic compounds in biomass burning aerosols over Amazonia– 1. Characterization by NMR and GC-MS. Journal of Geophysical Research– Atmospheres 107 (8047), 1–16.

Greenberg, J., Friedli, H., Guenther, A., Hanson, D., Harley, P., Karl, T., 2006. Volatile organic emissions from the distillation and pyrolysis of vegetation. Atmospheric Chemistry and Physics 6, 81–91.

Grieshop, A. P., Donahue, N. M., Robinson, A. L., 2009. Laboratory investigation of photochemical oxidation of organic aerosol from wood fires 2: analysis of aerosol mass spectrometer data. Atmospheric Chemistry and Physics 9, 2227– 2240.

Gustafsson, O., Krusa, M., Zencak, Z., Sheesley, R. J., Granat, L., Engstrom, E., Praveen, P. S., Rao, P. S. P., Leck, C., Rodhe, H., 2009. Brown Clouds over South Asia: Biomass or Fossil Fuel Combustion? Science 323 (5913), 495.

Hakola, H., Arey, J., Aschmann, S. M., Atkinson, R., 1994. Product formation from the gas-phase reactions of OH radicals and O_3 with a series of monoterpenes. Journal of Atmospheric Chemistry 18 (1), 75–102.

Hameed, S., Dignon, J., 1988. Changes in the geographical distributions of global emissions of NOx and SOx from fossil-fuel combustion between 1966 and 1980. Atmospheric Environment 22 (3), 441–449.

Hatakeyama, S., Izumi, K., Fukuyama, T., Akimoto, H., Washida, N., 1991. Reactions of OH with α-pinene and β-pinene in air: estimate of global CO production from the atmospheric oxiodation of terpenes. Journal of Geophysical Research– Atmospheres 96 (1), 947–958.

Hawkins, L. N., Russell, L. M., Covert, D. S., Quinn, P. K., Bates, T. S., 2010. Carboxylic Acids, Sulfates, and Organosulfates in Processed Continental Organic

Aerosol over the Southeast Pacific Ocean during VOCALS-REx 2008 *submitted*, http://aerosols.ucsd.edu/publications.html.

Hoffer, A., Gelencser, A., Blazsó, M., Guyon, P., Artaxo, P., Andreae, M. O., 2006. Diel and seasonal variations in the chemical composition of biomass burning aerosol. Atmospheric Chemistry and Physics 6 (11), 3505–3515.

Holzinger, R., Warneke, C., Hansel, A., Jordan, A., Lindinger, W., Scharffe, D. H., Schade, G., Crutzen, P. J., 1999. Biomass Burning as a Source of Formaldehyde, Acetaldehyde, Methanol, Acetone, Acetonitrile, and Hydrogen Cyanide. Geophysical Research Letters 26 (8), 1161–1164.

Jacobson, M. C., Hansson, H. C., Noone, K. J., Charlson, R. J., 2000. Organic atmospheric aerosols: Review and state of the science. Reviews of Geophysics 38 (2), 267–294.

Jayne, J. T., Leard, D. C., Zhang, X., Davidovits, P., Smith, K. A., Kolb, C. E., Worsnop, D. R., 2000. Development of an aerosol mass spectrometer for size and composition analysis of submicron particles. Aerosol Science and Technology 33 (1), 49–70.

Jimenez, J. L., Jayne, J. T., Shi, Q., Kolb, C. E., Worsnop, D. R., Yourshaw, I., Seinfeld, J. H., Flagan, R. C., Zhang, X., Smith, K. A., et al., 2003. Ambient aerosol sampling using the aerodyne aerosol mass spectrometer. Journal of Geophysical Research–Atmospheres 108 (D7), 8425.

Kanakidou, M., Seinfeld, J. H., Pandis, S. N., Barnes, I., Dentener, F., Facchini, M. C., Van Dingenen, R., Ervens, B., Nenes, A., Nielsen, C. J., et al., 2005. Organic aerosol and global climate modelling: a review. Atmospheric Chemistry and Physics 5 (4), 1053–1123.

Kanakidou, M., Tsigaridis, K., Dentener, F. J., Crutzen, P. J., 2000. Human-activity-enhanced formation of organic aerosols by biogenic hydrocarbon oxidation. Journal of Geophysical Research–Atmospheres 105 (D7), 9243–9354.

Kato, N., Akimoto, H., 2007. Anthropogenic emissions of SO2 and NOx in Asia: emission inventories. Atmospheric Environment 41, 171–191.

Kirchstetter, T. W., Novakov, T., Hobbs, P. V., 2004. Evidence that the spectral dependence of light absorption by aerosols is affected by organic carbon. Journal of Geophysical Research–Atmospheres 109 (D21), doi:10.1029/2004JD004999.

Lanz, V. A., Alfarra, M. R., Baltensperger, U., Buchmann, B., Hueglin, C., Prévôt, A. S. H., 2007. Source apportionment of submicron organic aerosols at an urban site by factor analytical modelling of aerosol mass spectra. Atmospheric Chemistry and Physics 7 (6), 1503–1522.

Lanz, V. A., Alfarra, M. R., Baltensperger, U., Buchmann, B., Hueglin, C., Szidat, S., Wehrli, M. N., Wacker, L., Weimer, S., Caseiro, A., et al., 2008. Source attribution of submicron organic aerosols during wintertime inversions by advanced factor analysis of aerosol mass spectra. Environmental science & technology 42 (1), 214.

Leithead, A., Li, S. M., Hoff, R., Cheng, Y., Brook, J., 2006. Levoglucosan and dehydroabietic acid: Evidence of biomass burning impact on aerosols in the Lower Fraser Valley. Atmospheric Environment 40 (15), 2721–2734.

Liu, S., Takahama, S., Russell, L., Gilardoni, S., Baumgardner, D., 2009. Oxygenated organic functional groups and their sources in single and submicron organic particles in MILAGRO 2006 campaign. Atmospheric Chemistry and Physics 9, 6849–6863.

Lukács, H., Gelencsér, A., Hammer, S., Puxbaum, H., Pio, C., Legrand, M., Kasper-Giebl, A., Handler, M., Limbeck, A., Simpson, D., et al., 2007. Seasonal trends and possible sources of brown carbon based on 2-year aerosol measurements at six sites in Europe. Journal of Geophysical Research–Atmospheres 112, doi:10.1029/2006JD008151.

Mang, S. A., Henricksen, D. K., Bateman, A. P., Andersen, M. P. S., Blake, D. R., Nizkorodov, S. A., 2008. Contribution of carbonyl photochemistry to aging of atmospheric secondary organic aerosol. The Journal of Physical Chemistry A 112 (36), 8337–8344.

Maria, S. F., Russell, L. M., Turpin, B. J., Porcja, R. J., 2002. FTIR measurements of functional groups and organic mass in aerosol samples over the Caribbean. Atmospheric Environment 36 (33), 5185–5196.

Maria, S. F., Russell, L. M., Turpin, B. J., Porcja, R. J., Campos, T. L., Weber, R. J., Huebert, B. J., 2003. Source signatures of carbon monoxide and organic functional groups in Asian Pacific Regional Aerosol Characterization Experiment (ACE-Asia) submicron aerosol types. Journal of Geophysical Research–Atmospheres 108, 8637.

Matthew, B. M., Middlebrook, A. M., Onasch, T. B., 2008. Collection efficiencies in an Aerodyne aerosol mass spectrometer as a function of particle phase for laboratory generated aerosols. Aerosol Science and Technology 42 (11), 884–898.

Mayol-Bracero, O. L., Guyon, P., Graham, B., Roberts, G., Andreae, M. O., Decesari, S., Facchini, M. C., Fuzzi, S., Artaxo, P., 2002. Water-soluble organic compounds in biomass burning aerosols over Amazonia: 2. Apportionment of the chemical composition and importance of the polyacidic fraction. Journal of Geophysical Research–Atmospheres 107, 8091.

Medeiros, P. M., Conte, M. H., Weber, J. C., Simoneit, B. R. T., 2006. Sugars as source indicators of biogenic organic carbon in aerosols collected above the Howland Experimental Forest, Maine. Atmospheric Environment 40 (9), 1694–1705.

Norrish, R. G. W., Bamford, C. H., 1936. Photo-decomposition of aldehydes and ketones. Nature 138, 1016.

Oros, D. R., Simoneit, B. R. T., 2001. Identification and emission factors of molecular tracers in organic aerosols from biomass burning Part 1. Temperate climate conifers. Applied Geochemistry 16 (13), 1513–1544.

Paatero, P., Tapper, U., 1994. Positive matrix factorization: A non-negative factor model with optimal utilization of error estimates of data values. Environmetrics 5 (2), 111–126.

Pavia, D., Lampman, G., Kriz, G., 2008. Introduction to spectroscopy. Brooks/Cole Pub Co.

Phinney, L., Richard Leaitch, W., Lohmann, U., Boudries, H., Worsnop, D. R., Jayne, J. T., Toom-Sauntry, D., Wadleigh, M., Sharma, S., Shantz, N., 2006. Characterization of the aerosol over the sub-arctic north east Pacific Ocean. Deep-Sea Research Part II 53 (20-22), 2410–2433.

Pósfai, M., Gelencser, A., Simonics, R., Arató, K., Li, J., Hobbs, P. V., Buseck, P. R., 2004. Atmospheric tar balls: Particles from biomass and biofuel burning. Journal of Geophysical Research–Atmospheres 109, doi:10.1029/2003JD004169.

Quinn, P. K., Bates, T. S., Coffman, D., Onasch, T. B., Worsnop, D., Baynard, T., De Gouw, J. A., Goldan, P. D., Kuster, W. C., Williams, E., et al., 2006. Impacts of sources and aging on submicrometer aerosol properties in the marine boundary layer across the Gulf of Maine. Journal of Geophysical Research–Atmospheres 111, doi:10.1029/2006JD007582.

Radzi bin Abas, M., Oros, D. R., Simoneit, B. R. T., 2004. Biomass burning as the main source of organic aerosol particulate matter in Malaysia during haze episodes. Chemosphere 55 (8), 1089–1095.

Rolph, G. D., 2003. Real-time Environmental Applications and Display sYstem (READY) Website. http://www.arl.noaa.gov/ready.php) NOAA Air Resources Laboratory, Silver Spring, MD.

Russell, L. M., Bahadur, R., Hawkins, L. N., Allan, J., Baumgardner, D., Quinn, P. K., Bates, T. S., 2009a. Organic aerosol characterization by complementary measurements of chemical bonds and molecular fragments. Atmospheric Environment 43, 6100–6105.

Russell, L. M., Hawkins, L. N., Frossard, A. A., Quinn, P. K., Bates, T. S., 2010. Carbohydrate-Like Composition of Submicron Atmospheric Particles and their Production from Ocean Bubble Bursting. Proceedings of the National Academy of Sciences, doi:10.1073/pnas.0908905107.

Russell, L. M., Takahama, S., Liu, S., Hawkins, L. N., Covert, D. S., Quinn, P. K., Bates, T. S., 2009b. Oxygenated fraction and mass of organic aerosol from direct emission and atmospheric processing measured on the R/V Ronald Brown during TEXAQS/GoMACCS 2006. Journal of Geophysical Research–Atmospheres 114, doi:10.1029/2008JD011275.

Saarikoski, S., Sillanpaa, M., Sofiev, M., Timonen, H., Saarnio, K., Teinila, K., Karppinen, A., Kukkonen, J., Hillamo, R., 2007. Chemical composition of aerosols during a major biomass burning episode over northern Europe in spring 2006: Experimental and modelling assessments. Atmospheric Environment 41 (17), 3577–3589.

Sage, A. M., Weitkamp, E. A., Robinson, A. L., Donahue, N. M., 2008. Evolving mass spectra of the oxidized component of organic aerosol: results from aerosol mass spectrometer analyses of aged diesel emissions. Atmospheric Chemistry and Physics 8 (5), 1139–1152.

Schneider, J., Weimer, S., Drewnick, F., Borrmann, S., Helas, G., Gwaze, P., Schmid, O., Andreae, M. O., Kirchner, U., 2006. Mass spectrometric analysis and aerodynamic properties of various types of combustion-related aerosol particles. International Journal of Mass Spectrometry 258 (1-3), 37–49.

Shaw, P., Russell, L. M., Jefferson, A., Quinn, P. K., 2010. Arctic organic aerosol measurements reveal mixed combustion particles from spring haze and ocean-derived particles in winter. http://aerosols.ucsd.edu/publications.html, submitted.

Simoneit, B. R. ., Schauer, J. J., Nolte, C. G., Oros, D. R., Elias, V. O., Fraser, M. P., Rogge, W. F., Cass, G. R., 1999. Levoglucosan, a tracer for cellulose in biomass burning and atmospheric particles. Atmospheric Environment 33 (2), 173–182.

Simoneit, B. R. T., 1985. Application of molecular marker analysis to vehicular exhaust for source reconciliations. International Journal of Environmental Analytical Chemistry 22 (3-4), 203–233.

Simoneit, B. R. T., 2002. Biomass burninga review of organic tracers for smoke from incomplete combustion. Applied Geochemistry 17 (3), 129–162.

Simoneit, B. R. T., Kobayashi, M., Mochida, M., Kawamura, K., Lee, M., Lim, H. J., Turpin, B. J., Komazaki, Y., 2004. Composition and major

sources of organic compounds of aerosol particulate matter sampled during the ACE-Asia campaign. Journal of Geophysical Research–Atmospheres 109, doi:10.1029/2004JD004598.

Sorooshian, A., Murphy, S. M., Hersey, S., Gates, H., Padro, L. T., Nenes, A., Brechtel, F. J., Jonsson, H., Flagan, R. C., Seinfeld, J. H., 2008. Comprehensive airborne characterization of aerosol from a major bovine source. Atmospheric Chemistry and Physics 8, 5489–5520.

Sullivan, A., Holden, A., Patterson, L., McMeeking, G., Kreidenweis, S., Malm, W., Hao, W., Wold, C., Collett Jr, J., 2008. A method for smoke marker measurements and its potential application for determining the contribution of biomass burning from wildfires and prescribed fires to ambient PM2. 5 organic carbon. Journal of Geophysical Research–Atmospheres 113, doi:10.1029/2008JD010216.

Turpin, B., Lim, H., 2001. Species contributions to PM2. 5 mass concentrations: Revisiting common assumptions for estimating organic mass. Aerosol Science and Technology 35 (1), 602–610.

Ulbrich, I. M., Canagaratna, M. R., Zhang, Q., Worsnop, D. R., Jimenez, J. L., 2009. Interpretation of organic components from positive matrix factorization of aerosol mass spectrometric data. Atmospheric Chemistry and Physics 9, 2891–2918.

Weimer, S., Alfarra, M. R., Schreiber, D., Mohr, M., Prevot, Prévôt, A. S. H., Baltensperger, U., 2008. Organic aerosol mass spectral signatures from wood-burning emissions: Influence of burning conditions and wood type. Journal of Geophysical Research–Atmospheres 113 (D10), doi:10.1029/2007JD009309.

Zeng, Y., Hopke, P., 1989. A study of the sources of acid precipitation in Ontario, Canada. Atmospheric Environment 23 (7), 1499–1509.

Zhang, Q., Alfarra, M. R., Worsnop, D. R., Allan, J. D., Coe, H., Canagaratna, M. R., Jimenez, J. L., 2005a. Deconvolution and quantification of hydrocarbon-like and oxygenated organic aerosols based on aerosol mass spectrometry. Environmental Science &Technology 39 (13), 4938–4952.

Zhang, Q., Canagaratna, M. R., Jayne, J. T., Worsnop, D. R., Jimenez, J. L., 2005b. Time-and size-resolved chemical composition of submicron particles in Pittsburgh: Implications for aerosol sources and processes. Journal of Geophysical Research–Atmospheres 110, doi:10.1029/2004JD004649.

Zhang, Q., Jimenez, J. L., Canagaratna, M. R., Allan, J. D., Coe, H., Ulbrich, I., Alfarra, M. R., Takami, A., Middlebrook, A. M., Sun, Y. L., et al., 2007. Ubiquity and dominance of oxygenated species in organic aerosols in

anthropogenically-influenced Northern Hemisphere midlatitudes. Geophysical Research Letters 34, doi:10.1029/2007GL029979.

Zhang, Q., Worsnop, D. R., Canagaratna, M. R., Jimenez, J. L., 2005c. Hydrocarbon-like and oxygenated organic aerosols in Pittsburgh: Insights into sources and processes of organic aerosols. Atmospheric Chemistry and Physics 5, 3289–3311.

Zorn, S. R., Drewnick, F., Schott, M., Hoffmann, T., Borrmann, S., 2008. Characterization of the South Atlantic marine boundary layer aerosol using an aerodyne aerosol mass spectrometer. Atmospheric Chemistry and Physics 8, 4711–4728.

Chapter 3

Carboxylic Acids, Sulfates, and Organosulfates in Processed Continental Organic Aerosol over the Southeast Pacific Ocean during VOCALS-REx 2008

Abstract. Submicron particles were collected on board the NOAA R/V *Ronald H. Brown* during the VAMOS Ocean-Cloud-Atmosphere-Land Study Regional Experiment (VOCALS-REx) in the southeast Pacific marine boundary layer in October and November 2008. The aerosol in this region was characterized by low numbers of particles (150-700 cm^{-3}) that were dominated by sulfate ions at concentrations of 0.9 ± 0.7 μg m^{-3} and organic mass at 0.6 ± 0.4 μg m^{-3}, with no measurable nitrate and low ammonium ion concentrations. Measurements of submicron organic aerosol functional groups and tracer elements show that continental

outflow of anthropogenic emissions is the dominant source of organic mass (OM) to the southeast Pacific with an additional, smaller contribution of organic mass from primary marine sources. This continental source is supported by a correlation between OM and radon. Saturated aliphatic C-CH (alkane) composed 41±27% of OM. Carboxylic acid COOH (32±23% of OM) was observed in single particles internally mixed with ketonic carbonyl, carbonate, and potassium. Organosulfate $COSO_3$ (4±8% of OM) was observed only during the periods of highest organic and sulfate concentrations and lowest ammonium concentrations, consistent with a sulfuric acid epoxide hydrolysis for proposed surrogate compounds (*e.g.* isoprene oxidation products) or reactive glyoxal uptake mechanisms from laboratory studies. This correlation suggests that in high sulfate, low ammonium conditions, the formation of organosulfate compounds in the atmosphere contributes a significant fraction of aerosol OM (up to 13% in continental air masses). Organic hydroxyl C-OH composed 20±12% of OM and up to 50% of remote marine OM and was inversely correlated with radon indicating a marine source. A two-factor solution of Positive Matrix Factorization (PMF) analysis resulted in one factor dominated by organic hydroxyl (> 70% by mass) and one factor dominated by saturated aliphatic C-CH (alkane) and carboxylic acid (together 90% by mass), identified as the Marine and Combustion factors, respectively. Measurements of particle concentrations in the study region compared with concentrations estimated from MODIS aerosol optical depth indicate that continental outflow results in MBL particle concentrations elevated up to 2 times the background level (less than 300 cm^{-3}) away from shore and up to 10 times the background level at the coast. The presence of both coastal fossil fuel combustion and marine sources of oxygenated organic aerosol results in little change in the oxygenated fraction and oxygen to carbon ratio (O/C) along the outflow of the region's dominant organic particle source.

3.1 Background

Aerosol particles in the marine boundary layer (MBL) are often mixtures of local primary (*e.g.* seasalt and organic compounds from seaspray), local secondary (*e.g.* sulfate from DMS oxidation), and transported primary and secondary emissions (*e.g.* organic carbon, elemental carbon, sulfate, nitrate, and ammonium) (Quinn et al., 1996; Maria et al., 2003; Allan et al., 2004; Quinn et al., 2006; Hawkins et al., 2008; Bates et al., 2008). Relative contributions of the particle sources will determine the specific particle composition but organic compounds are almost always present and often compose a significant fraction of the total submicron mass (Zhang et al., 2007); the large number of organic compounds present in ambient aerosol, in combination with their wide variety of hygroscopic properties, makes solubility of multi-component aerosols difficult to constrain using the available chemical information (Ervens et al., 2005; Prenni et al., 2007). This constraint has resulted in the implementation of several methods to measure water uptake and solubility proxies including water soluble organic carbon (WSOC), optical hygroscopicity (f(RH)), and cloud condensation nuclei (CCN) concentration.

Chemically-based approaches to characterizing the properties of organic particle mixtures (in the absence of detailed compound quantification) have included identifying organic mass by the presence of hetero-atoms (OM/OC) (Russell, 2003; Russell et al., 2009b), the presence of functional groups (Maria et al., 2002, 2003, 2004; Gilardoni et al., 2007), or the atomic ratio of oxygen to carbon (O/C) (DeCarlo et al., 2007; Russell et al., 2009b). These approaches rely on assumed relationships between these quantities and the mechanisms of their formation or the properties of the resulting organic mixtures.

For example, O/C has been used to infer the degree of atmospheric processing or photochemical "age" of organic aerosols under the assumption that emitted organic aerosol becomes increasingly oxidized (increase in O/C) with age (Maria et al., 2004; Zhang et al., 2005b; Johnson et al., 2005). This trend is consistent with laboratory measurements of secondary organic aerosol (SOA) formation pathways (Seinfeld et al., 2001; Donahue et al., 2005; Robinson et al., 2007) and field

measurements of organic aerosol composition near organic particle sources (Zhang et al., 2005b; Russell et al., 2009b; Liu et al., 2009). However, in these cases, the majority of the aerosol was formed either from gas or particle phase hydrocarbon compounds in the absence of a primary source of oxygenated aerosol. This assumption is an oversimplification, for example, in the anthropogenically-influenced marine atmosphere where primary emissions of oxygenated marine organic aerosol can mix with transported oxidized organic aerosol from continental sources (Mochida et al., 2002; Russell et al., 2010).

Quantitative measurements of organic functional groups (measured either in bulk submicron or in single particles) provide additional, detailed information on organic composition beyond O/C or WSOC fraction. FTIR measurements of carboxylic acid and organosulfate groups also provide estimates of the contribution of SOA to total OM, which is currently poorly understood (Donahue et al., 2005; Robinson et al., 2007). Organosulfate groups in particular are a potentially large, yet currently rarely quantified, source of SOA owing to their ability to increase partitioning of semivolatile organic compounds from the gas phase to the particle phase (Iinuma et al., 2007; IInuma et al., 2007; Surratt et al., 2007b,a; Iinuma et al., 2009; Claeys et al., 2009).

In this study we use measurements of particle concentrations, organic functional groups, elemental concentrations, and single particle composition to explore the composition, sources, and processes influencing submicron aerosol chemical composition in the MBL. We investigate organic composition from Fourier Transform Infrared (FTIR) spectroscopy and from Quadrupole Aerosol Mass Spectrometry (Q-AMS) in order to improve our understanding of (1) the relative contributions of anthropogenic and marine sources to organic aerosol, (2) the oxidation of organic aerosols emitted from combustion sources, and (3) the significance and formation of organosulfate compounds in submicron aerosol. We also explore the significance and geographic distribution of continental outflow on the background MBL aerosol loading. The measurements used in this study were collected over a 42-day period aboard the NOAA R/V *Ronald H. Brown* (RHB) traveling near the western coasts of Peru and Chile using fixed temperature, relative humidity, and

size-cut sampling protocols (Bates et al., 2008).

3.2   Introduction

The southeast Pacific MBL was the location of the VAMOS Ocean-Cloud-Atmosphere-Land Study Regional Experiment (VOCALS-REx) conducted in October and November 2008. Strong southeasterly surface winds north of 23°S in this region follow the coast lines of Chile and Peru and drive intense coastal upwelling, making the coastal surface waters significantly colder than those found at similar latitudes in other regions (Garreaud and Muñoz, 2005). This cold surface water helps to sustain a large, uniform marine stratocumulus cloud deck present nearly year-round (Richter and Mechoso, 2006). The strong southeasterly surface winds also transport aerosol and aerosol precursor components (*e.g.* sulfate, SO_2, dust, and organic components) from cities such as Santiago, Chile, to the marine boundary layer increasing the background concentration of particles and potentially impacting cloud drop number, concentration, albedo and precipitation (Artaxo et al., 1999; Bretherton et al., 2004; Huneeus et al., 2006). A goal of the aerosol chemistry portion of the VOCALS-REx campaign was to characterize the composition, size, and variability of the submicron aerosol to improve understanding of the particle sources to the region and to better constrain the hygroscopic properties of the ambient aerosol. Radon (a decay product of rocks) has a 3.8 day half-life and was used to quantify the relative amount of continental influences on the sampled air masses. We have designated three air mass types based on radon concentrations and HYSPLIT back trajectories. Consistent with radon measurements, HYSPLIT back trajectories show air masses traveling from the south along the coast to the ship; air masses with back trajectories that had passed closer to land within 3 days of reaching the ship had higher radon concentrations.

3.3 Method

Submicron particles were collected through an isokinetic sampling inlet located on the forward deck of the RHB approximately 18 meters above sea level (masl) (Quinn et al., 2008; Bates et al., 2008; Russell et al., 2009b). 37 mm Teflon filters (Pall Inc., 1 μm pore) for Fourier Transform Infrared (FTIR) spectroscopic and X-Ray Fluorescence (XRF) analyses were located downstream of a 1-μm sharp-cut cyclone (SCC 2.229 PM1, BGI Inc.) in a humidity-controlled enclosure (60%) and were collected over 12 to 24 hours (short samples) with simultaneous 24 to 48 hour duplicate samples. Sampling times were adjusted based on the organic mass concentration measured by the Aerodyne Quadrupole Aerosol Mass Spectrometer (Q-AMS). Long sampling times allowed improved signal-to-noise ratios for the low concentrations of the organic functional groups (< 0.8 μg m^{-3}) in the relatively clean marine boundary layer (MBL).

FTIR samples were kept at 0°C from the end of sample collection until FTIR spectroscopic analysis to reduce evaporative losses of organic compounds. For the earliest samples, this period was approximately 60 days. Duplicate back filters accompanied each sample filter for the entirety of the sampling process and were analyzed to quantify the adsorption of volatile compounds and other sources of contamination. These back filters showed negligible infrared absorption. FTIR absorbance spectra of each sample and back filter were measured non-destructively using a Bruker Tensor 27 spectrometer with RT-DLATGS detector (Gilardoni et al., 2007) and were interpreted using a revised algorithm and calibration standards (Russell et al., 2009b). Quantified functional groups include saturated aliphatic C-CH (alkane), unsaturated aliphatic C=CH (alkene), aromatic C=CH, non-acidic organic hydroxyl C-OH (alcohol, including phenol), primary amine C-NH$_2$, non-acidic carbonyl C=O, carboxylic acid COOH, and organosulfate COSO$_3$ groups. Non-acidic carbonyl C=O, aromatic C=C-H, and unsaturated aliphatic C=C-H (alkene) groups were below detection limit in all samples and were omitted from the discussion presented here. Organosulfate groups absorb at 876 cm^{-1} and have interference from HSO$_4^-$ and CO$_3^{2-}$ absorption. To quantify this interference, filters with detectable absorption at 876 cm^{-1} were rinsed with 2 mL of hexane solvent,

which removes the organosulfate-containing compounds but not bisulfate or carbonate (Maria et al., 2003; Gilardoni et al., 2007). Concentrations of organosulfate were determined from the peak area removed by the hexane rinse (which resulted in complete removal of the absorbance at 876 cm^{-1}) and an ethylsulfate calibration standard. The sum of all measured organic functional groups is used to determine organic mass (OM) concentration for each filter period. X-ray fluorescence on the Teflon filters was completed by Chester Labnet (Tigard, Oregon) and provided concentrations of Na and heavier elements (Maria et al., 2003; Gilardoni et al., 2007; Russell et al., 2009b).

The Aerodyne Quadrupole Aerosol Mass Spectrometer (Q-AMS) measures bulk non-refractory submicron aerosol chemical composition and component-specific size distributions in real-time. Only a brief description is provided here; more detailed information on the Q-AMS can be found in Jayne et al. (2000) and Jimenez et al. (2003). The instrument consists of an aerodynamic lens followed by a rotating chopper. This time-of-flight (ToF) region is followed by a 600°C vaporizer and electron impact ionizer. From there the sample is analyzed using a quadrupole mass spectrometer with 1 amu resolution. Quantified components include SO_4^{2-}, NO_3^-, NH_4^+, and organic mass. Collocated multi-stage impactors were used to collect inorganic samples for extraction and ionic analysis (761 Compact IC, Metrohm) (Quinn et al., 2006, 2008; Bates et al., 2008). SO_4^{2-} and NH_4^+ from ion chromatography (IC) analysis of the impactor samples were used to derive the collection efficiency of the AMS for the inorganic ions (Quinn et al., 2006). The project average shows good correlation for sulfate (AMS vs IC slope = 1.09, r = 0.94) and ammonium (AMS vs IC slope = 0.85, r = 0.9) between the two methods and a collection efficiency (CE) of 1 is applied to the inorganic AMS measurements. The CE of organic mass was lower than 1 based on the FTIR/AMS comparison of OM as described in Section 4.3. Collocated measurements of condensation nuclei (CN) concentration for particle diameters greater than 13 nm were collected using a TSI 3010 condensation particle counter (CPC) on the shared inlet at 1-minute resolution. Particle number-size distribution was measured on a 5-minute time basis by a combination of mobility and aerodynamic particle sizing from 20 nm to

10 μm diameter (Bates et al., 2008).

From the same isokinetic inlet, single particles were collected by impaction onto silicon nitride windows (Si$_3$N$_4$, Silson Ltd, Northampton, England) for 30 min periods (Streaker, PIXE Internationl Corp., Tallahassee, FL). The windows were kept at 0°C prior to analysis by Scanning Transmission X-ray Microscopy-Near Edge X-ray Fine Structure (STXM-NEXAFS) at the Advanced Light Source at Lawrence Berkeley National Laboratory in Berkeley, CA (Takahama et al., 2007, 2010). Particle morphology (*e.g.* spherical, irregular, or cubic) and mixture type (*e.g.* seasalt-organic, dust-organic, or combustion) can be determined from single particle images and optical density spectra of the carbon K-edge (between 278 and 305 eV). Mixture type is determined from STXM-NEXAFS spectra based on relative amounts of components (*i.e.* alkane, alkene, carboxylic carbonyl, ketonic carbonyl, carbonate, and potassium).

3.4 Results

3.4.1 Regional Extent of Continental Outflow to the MBL

Remote-sensing measurements of cloud drop radius analyzed by Bretherton et al. (2004) and Huneeus et al. (2006) have indicated that the large pollution sources, especially copper smelters, along the Peruvian and Chilean coasts could impact particle concentrations, cloud properties, and cloud albedo in the southeast Pacific MBL by significantly increasing particle concentrations above background levels, resulting in longitudinal gradients in particle concentration and cloud drop radii. One of the goals of the VOCALS-REx study was to quantify the extent of this continental outflow on the stratocumulus-topped boundary layer near 20°S. Defining a particle concentration for the "clean" marine atmosphere is not straightforward, as background concentrations are regionally and temporally variable. However, a survey of previous studies (Fig. 3.1a) suggests that particle concentrations (CN) between 300 and 500 cm^{-3} are a reasonable upper limit for the clean MBL (Pirjola et al., 2000; Bates et al., 2000; O'Dowd et al., 2001; Twohy et al., 2005; Andreae, 2009). Particle concentrations in the MBL defined

as "polluted" in the same studies range from greater than 400 cm^{-3} to greater than 1500 cm^{-3}. VOCALS-REx average CN concentration was 350 ± 135 cm^{-3}, corresponding to a clean to moderately polluted MBL. Shipboard observations are limited to the cruise track and sampling times, so obtaining a regional picture of continental outflow from in situ measurements is difficult.

To address this issue, measurements of aerosol optical depth (AOD) from the MODerate resolution Imaging Spectroradiometer (MODIS) aboard NASA's Terra spacecraft were compared with filter-averaged CN concentrations when the satellite passed over the cruise track during clear-sky conditions. AOD was averaged over the entire latitude and longitude range traveled during the filter period. Due to the narrow satellite path and frequently cloudy skies, only three filters met the conditions for quantitative comparison. Measurements of AOD$_{500}$ from the ground-based AErosol RObotic NETwork (AERONET) and collocated measurements of CN concentration compiled by Andreae (2009) for clean and polluted marine environments were added to the comparison. Figure 3.1b shows the relationship between AOD and CN concentration for VOCALS-REx and previous studies in marine environments. MODIS AOD is slightly higher than AERONET AOD for similar aerosol loading though differences within the AERONET measurements for similar aerosol loadings are equally as large. Validation studies suggest that the two measurements agree within 2% when measurements are compared for the same wavelengths (Remer et al., 2002).

Figure 3.1c shows the average MODIS AOD for October and November 2008 during clear-sky conditions. South of 23°S, AOD is largely below 0.1, corresponding to CN concentrations less than 300 cm^{-3} based on the comparison in Figure 3.1b. This horizontal band of low AOD is expected from westerly surface winds that increase in intensity from about 23°S to 30°S and bring relatively clean marine air to the southeast Pacific. North of 23°S, surface winds are generally easterly (Bretherton et al., 2004) bringing polluted air masses from the Chilean coast west to the study region. Shipboard CN measurements have been converted to AOD using the best fit line for all points in Figure 3.1b. From only shipboard measurements, the latitudinal trend in AOD is not visible. A weak longitudinal
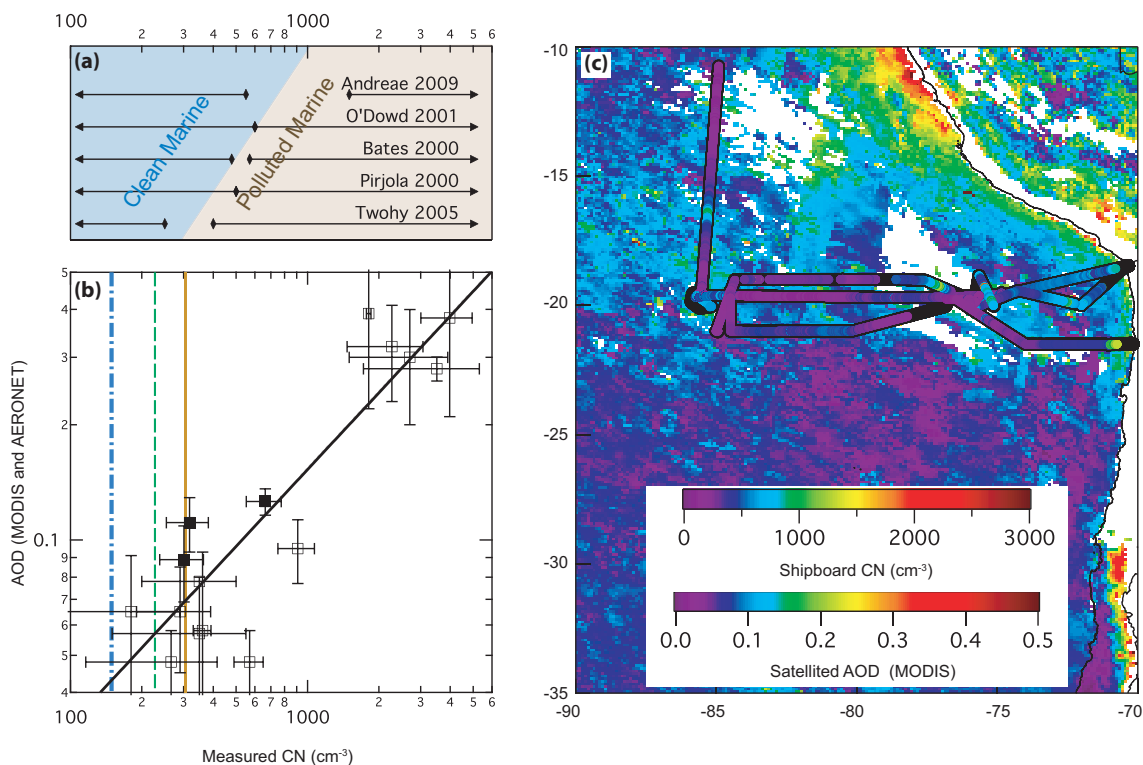
Figure 3.1: (a) Particle concentrations (and ranges of concentrations) classified as "clean marine" and "polluted marine" in previous studies. (b) Satellite-derived AOD from MODIS (this work, closed squares) and AERONET (Andreae (2009), open squares) compared with CN measurements. In all cases, error bars represent one standard deviation on the mean. The best fit line (AOD = $0.0017*CN^{0.66}$) includes both MODIS and AERONET measurements. Blue (dot-dashed), green (dashed), and tan (solid) vertical lines mark the average CN concentration during MAM, XAM, and CAM periods, respectively. (c) Average MODIS AOD for October and November 2008 for study region. White regions (missing data) were cloudy during both October and November. Cruise track of the NOAA R/V *Ronald H. Brown* is shown in black. Shipboard CN measurements are overlaid on the cruise track.

trend is present, but the sharp decrease in AOD with distance from the coast is masked by patchy areas of intermediate aerosol loading. Because of the surface winds, the steep longitudinal gradient in particle concentration is superimposed on the large scale latitudinal trend. Near shore AOD ranged from 0.15 to 0.4 corresponding roughly to CN concentrations between 600 and 4000 cm^{-3}, with the highest AOD occurring within the first several hundred kilometers from the coast. AOD values from 0.1 to 0.15 (corresponding to 300 to 600 cm^{-3}), corresponding to a doubling of particle concentration, were observed at distances even greater than 1000 km from the nearest coastline in the region north of 23°S. Therefore, the outflow of continental emissions has only a minor, near-shore influence in the region south of 23°S, while the region north of 23°S appears to have particle concentrations significantly elevated above background levels, which would result in greater potential direct and indirect aerosol effects in, and to the north of, the VOCALS-REx study region. This finding supports the proposed hypothesis that continental outflow from the South American coast has a significant impact on ambient aerosol concentrations.

For in situ measurements, radon concentrations were used to categorize VOCALS-REx air masses as "continental" air masses (CAM), "mixed" air masses (XAM), and "marine" air masses (MAM). Based on calibrations, the lower limit of detectable radon for the project was 200 mBq m^{-3}. However, an increase in the background concentration of radon between the first and second calibration periods and subsequent adjustment to the concentrations means that different radon concentration limits were needed for each leg to assign air mass categories. For Leg 1, MAM periods were defined by radon less than 250 mBq m^{-3}, CAM periods were defined by radon greater than 350 mBq m^{-3}, and XAM periods were defined between the two concentrations. For Leg 2, MAM periods were defined by radon less than 150 mBq m^{-3}, CAM periods were defined by radon greater than 300 mBq m^{-3}, and XAM periods were defined between the two concentrations. This assignment is a simplification to highlight similarities and differences among the samples and not to imply that only one type of particle was measured at a given time. In Figure 3.1b, colored vertical lines mark the average CN concentration
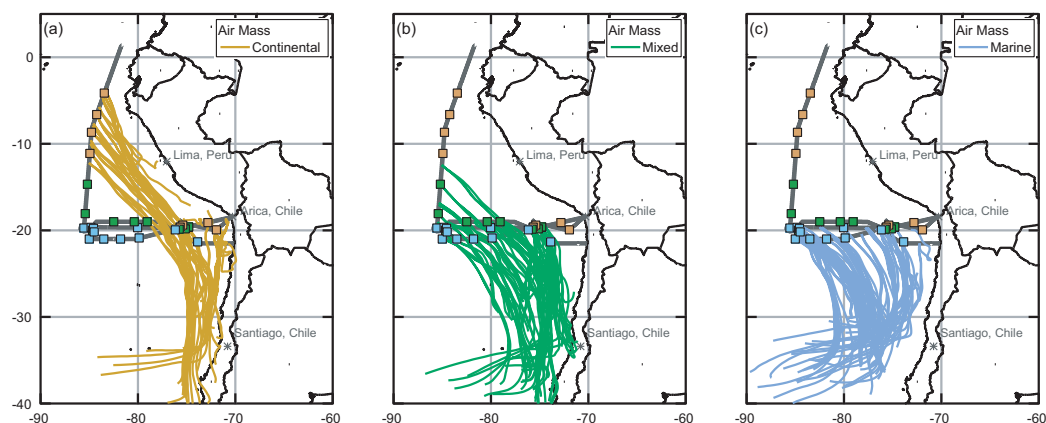
Figure 3.2: Track of the NOAA R/V *Ronald H. Brown* during VOCALS-REx from 21 October to 30 November 2008 and average location of each filter, marked by colored squares. Squares are colored by air mass assignment determined from average radon concentration. Nine 3-day HYSPLIT back trajectories (beginning, middle, and end of filter period at 50 m, 100 m, and 500 masl) are shown for (a) continental (CAM), (b) mixed (XAM), and (c) marine air masses (MAM).

during MAM, XAM, and CAM periods. For each filter, HYSPLIT back trajectories were calculated for the start, middle, and end of the sampling period at 50 masl, 100 masl, and 500 masl (Fig. 3.2) and are shown colored by air mass category. For most of the cruise, air masses traveled north, northeast, or east while south of 30°S latitude and then turned northwest, generally following the coastline. Radon measurements are consistent with HYSPLIT back trajectories; samples measured near the coast had higher radon (up to 1000 mBq m^{-3}) than those measured near 85° W latitude (less than 300 mBq m^{-3}).

3.4.2 Cluster Analysis of FTIR Spectra

Hierarchical Ward cluster analysis (Ward Jr, 1963) was used to separate the 31 sample FTIR spectra into three clusters (Fig. 3.3). For the cluster analysis, only absorbance between 4000 cm^{-1} and 1500 cm^{-1} was considered due to Teflon interference below 1300 cm^{-1} and the absence of quantified groups other than organosulfate below 1500 cm^{-1}. Using more than three clusters resulted in clusters with only 3 spectra, which were considered too small to be meaningful. Cluster
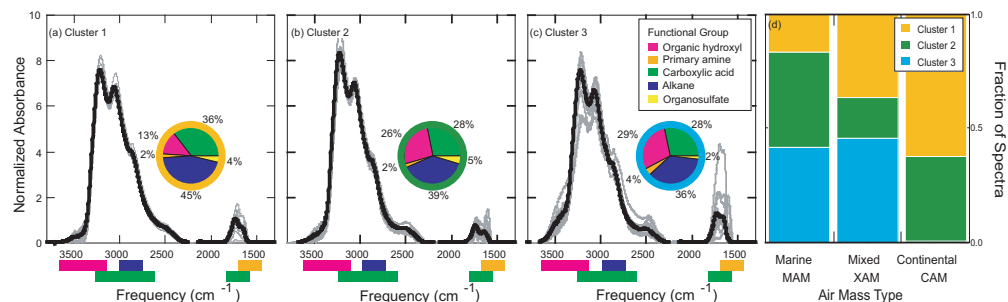
Figure 3.3: Ward cluster analysis on the 31 normalized sample spectra produced 3 clusters (Panels a-c). Average spectra of each cluster are shown in black. Pie charts show the average functional group composition of each cluster. Colored bars shown along the x-axis correspond to functional groups in the legend and indicate approximate absorbance region of each functional group with the exception of organosulfate, which is not included in the cluster analysis but is shown on the pie charts. (d) Fraction of sample spectra from each cluster for MAM, XAM, and CAM.

1 has the highest carboxylic acid and alkane fractions and a significantly lower organic hydroxyl fraction than the other clusters. Cluster 2 has twice the fraction of organic hydroxyl groups of Cluster 1 and less carboxylic acid and alkane groups. Cluster 3 has only slightly higher organic hydroxyl and lower alkane groups than Cluster 2 but includes three sample spectra all observed at the cruise location farthest from land and one sample with over 40% organic hydroxyl groups.

Figure 3.3(d) shows the fraction of sample spectra observed during each of the three air mass periods. Cluster 1 was observed in all three air mass types but was the dominant spectra type observed during CAM periods (63%) and was only observed in 17% of MAM periods indicating that the average composition of Cluster 1 represents the composition of processed continental organic aerosol. Cluster 3 was observed only during XAM (45%) and MAM (42%) periods, indicating that the higher organic hydroxyl fraction was related to a larger contribution from a marine organic source.

3.4.3   Organic, Inorganic, and Elemental Components

Figure 3.4 shows FTIR organic functional groups, AMS sulfate, ammonium, nitrate, and organic components. OM fraction from marine and combustion factors identified from PMF analysis for October and November 2008 are also shown (described in detail in Section 4.4). The variation in continental influence (radon) correlates with FTIR OM and AMS sulfate over the campaign. The sum of the organic functional groups defines total organic mass from FTIR. After 18 November the AMS was operated in the full scan mode (m/z range 0-300) with the particle beam permanently unblocked due to chopper motor malfunction. The background gas signal was obtained by closing the valve periodically, so sulfate concentrations after 18 November may have a higher uncertainty than measurements collected during normal operation, though baseline sulfate measured during the valve closed periods showed no change from baseline sulfate measured during normal operation. Organics, ammonium, and nitrate mass spectra overlap with air mass spectra and could not be estimated from the modified "closed" signal. Colored bars across the top axis show CAM, XAM, and MAM periods; total OM and sulfate were highest during CAM periods and lowest during MAM periods. Average concentrations of organic, inorganic, and elemental components for the campaign and CAM, XAM, and MAM periods are shown in Table 3.1. Sulfate was the dominant component of the submicron mass with an average of 0.93 ± 0.67 μg m^{-3} and ranged from 0.67 ± 0.33 μg m^{-3} in MAM to 1.4 ± 1.0 μg m^{-3} in CAM. FTIR OM was between 0.18 and 1.9 μg m^{-3} with a project average of 0.59 ± 0.37 μg m^{-3}. FTIR OM was only 0.4 ± 0.17 μg m^{-3} in MAM compared with 1.0 ± 0.5 μg m^{-3} in CAM. The average composition of the organic mass was $41 \pm 27\%$ alkane, $32 \pm 23\%$ carboxylic acid, $20 \pm 12\%$ organic hydroxyl, $3 \pm 2\%$ primary amine, and $4 \pm 8\%$ organosulfate. Average carboxylic acid fraction showed a small decrease from CAM to MAM while average organic hydroxyl fraction increased from 16% to 22%. O/C and OM/OC average ratios for the entire campaign were 0.62 ± 0.12 and 2.0 ± 0.19, respectively, and showed little change over the three air mass types. Elements above detection limit in greater than 20% of samples include S, Sn, V, Fe, K, Br, Ca, and Ni; other elements measured by XRF were below detection limit in more than 80%

of the samples and are not included in chemical comparisons. Concentrations of all reported elements show a decrease from CAM to MAM, with intermediate values reported for XAM, consistent with the air mass classification. Submicron Na and Cl from ion chromatography were above detection limit in most samples and composed $9\pm6\%$ of PM_1 on average.

Figure 3.5 shows the relationship of OM, sulfate, XRF elements, carboxylic acid fraction, organic hydroxyl fraction, FTIR O/C, and AMS m/z 44 fraction with radon. FTIR OM, dust and metals, and carboxylic acid fraction have mild correlations with radon (r=0.60, 0.74, and 0.54, respectively). AMS sulfate has a weak positive correlation to radon (0.43), possibly because the Chilean copper smelters have a stronger influence on sulfate concentration near the southern part of the cruise track while radon was higher near the northern part of the cruise track (along the coast of Peru). The organic hydroxyl fraction shows no correlation to radon (r = -0.23). Alkane fraction (not shown in Figure 3.5) does not show a trend with radon despite likely having a continental source and being removed by oxidation during atmospheric processing. This observation suggests that there were contributions from both continental and marine sources to alkane groups.

FTIR O/C and AMS m/z 44 fraction of OM are shown in the top two panels of Figure 3.5. FTIR O/C is calculated from the total number of oxygen atoms from oxygen-containing functional groups normalized by the total number of carbon atoms from all groups (Gilardoni et al., 2007; Russell et al., 2009b). AMS O/C is estimated from the ratio of m/z 44 fragment to AMS OM, which has shown a consistent relationship with atomic O/C from Elemental Analysis (EA) for both laboratory and field measurements (Aiken et al., 2008). The accuracy of reproducing atomic O/C from EA varies with organic compounds and is based on the fragmentation of organic acid groups which are assumed to be present in proportion to other oxygen-containing organic functional groups, including organic hydroxyl groups (Aiken et al., 2007). The m/z 44 fraction of AMS OM, which is reported to have a linear relationship with atomic O/C (Aiken et al., 2007) correlates with radon (r=0.56) while FTIR O/C shows no clear trend with radon reflecting the composition of the organic mass based on a mixture of both carboxylic acid and
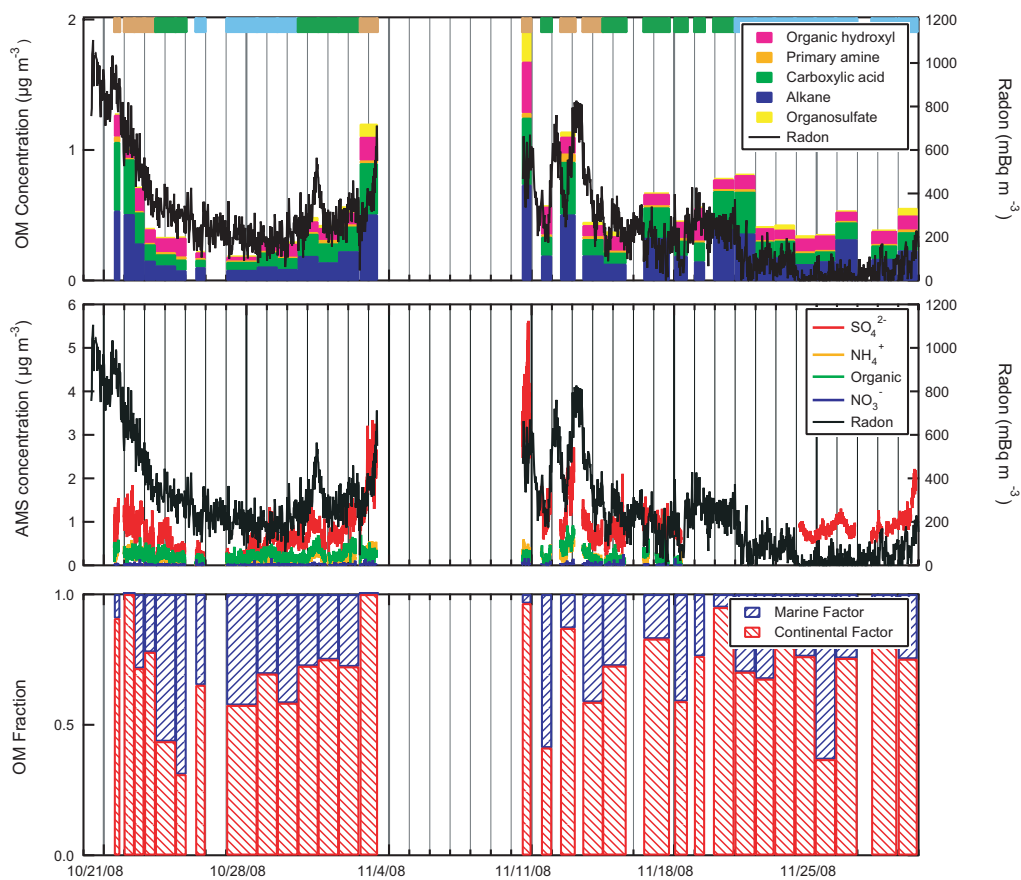
Figure 3.4: Time series of (a) FTIR functional groups, (b) AMS inorganic and organic components, and (c) fraction of OM from marine and combustion PMF factors. Colors across the top of (a) indicate air masses: CAM (tan), XAM (green) and MAM (blue). AMS organics, nitrate, and ammonium are not available after 18 November due to instrument malfunction. AMS sulfate has been estimated from the MS Open mode and the valve closed signal. Radon is a proxy for continental influence.
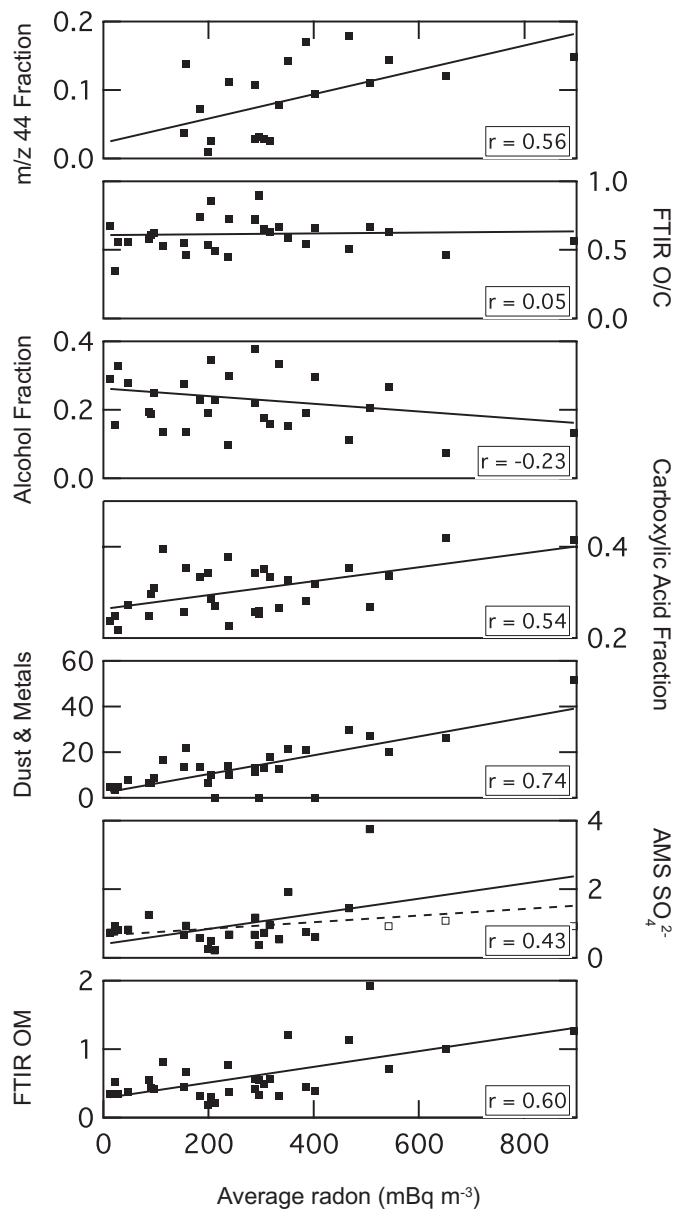
Figure 3.5: From top to bottom: AMS m/z 44 mass fraction, FTIR atomic O/C, FTIR organic hydroxyl fraction of OM (by mass), FTIR carboxylic acid fraction of OM (by mass), sum of XRF elements K, Ni, Ca, Fe, Sn, V, Br (ng m^{-3}), AMS SO$_4^{2-}$ (μg m^{-3}), and FTIR OM (μg m^{-3}). For AMS SO$_4^{2-}$, the open squares have been omitted from the reported linear regression (solid line) to illustrate the southerly bias of AMS SO$_4^{2-}$. The dashed line includes all AMS SO$_4^{2-}$.

other oxygenated organic functional groups (discussed in detail in Section 5.2).

3.4.4   Comparisons of FTIR and AMS Organic and Sulfate Concentrations

FTIR OM was correlated with AMS OM (r = 0.7) and was higher than AMS OM by a factor of 2.4 on average (Fig. 3.6). In previous field measurements, the two methods have been within 20% of each other, which is within the 20-30% uncertainty associated with both measurements (Gilardoni et al., 2007, 2009; Russell et al., 2009b). Adsorption of organic gases onto the filters was eliminated as a possible reason for the discrepancy because the back-filters showed negligible OM and the discrepancy in OM was independent of sampling duration and showed no diurnal dependence. A portion of this difference can be explained by organosulfate $COSO_3$ groups. In AMS mass spectra and the fragmentation table used to assign mass fragments to particular components, only the carbon-containing fragment of the organosulfate would be attributed to organic mass. The sulfate fragment typically would be attributed to inorganic sulfate leading to a smaller organic mass measured by AMS than by FTIR when organosulfate groups are present. However, the organosulfate contribution can only explain a small fraction of the observed difference in OM between the two methods because sulfate from organosulfate groups composes only 0% to 12% of OM.

Another possible explanation for the discrepancy is an AMS OM collection efficiency (CE) less than the 100% measured for sulfate. Laboratory and field measurements have shown that solid particles have a much lower CE than liquid particles (Matthew et al., 2008) due to particles bouncing off the vaporizer before volatilization. For example, drying ammonium sulfate below its efflorescence relative humidity can reduce the CE of submicron particles from 100% to as low as 20% (Alfarra et al., 2004; Allan et al., 2004; Matthew et al., 2008). Ambient organic compounds are mostly present as liquids and generally have 100% CE (Alfarra et al., 2004; Zhang et al., 2005a) when they are not mixed with other components. The CE of organic components in organic and sulfate mixtures can be approximated to the CE of sulfate, generally measured independently (Jimenez et al.,
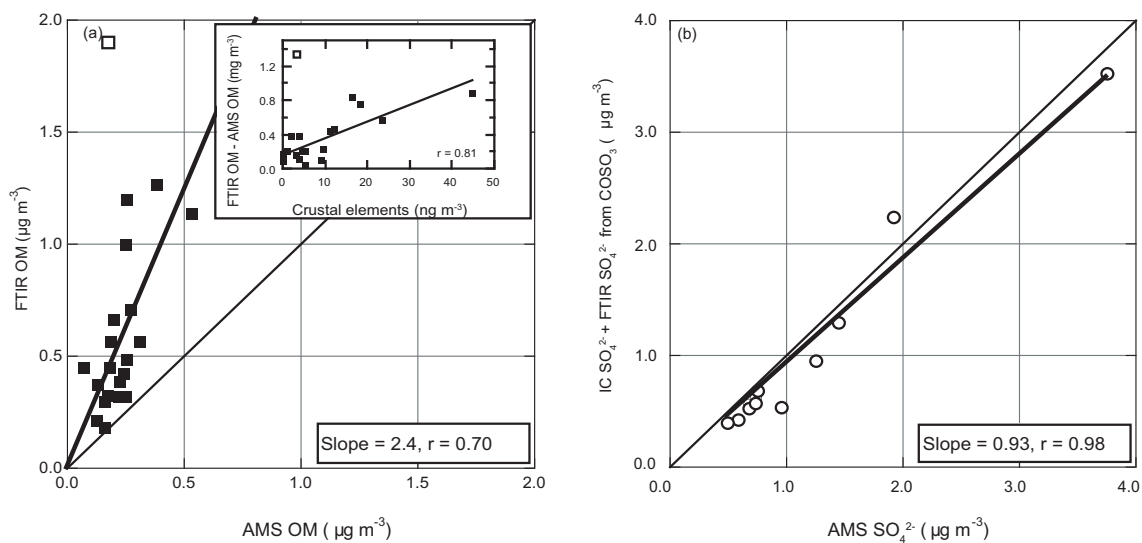
Figure 3.6: (a) Organic mass quantified from FTIR spectroscopy on Teflon filters is 2.4 times that measured by the Aerodyne AMS. AMS OM is averaged from the 5-minute resolution data and includes only those points when the filters were sampling. Inset: The difference in organic mass measured by FTIR spectroscopy (not including organosulfate) and AMS is correlated to the concentration of crustal components (nss-K, nss-Ca, Al, Si, Fe, and Ti). The open square in both graphs is not included in either linear regression to preserve the meaning of the calculated coefficients. (b) Comparison of the sum of IC nss-SO_4^{2-} and FTIR organic sulfate from $COSO_3$ with AMS sulfate.

2003; Drewnick et al., 2003; Bates et al., 2005; Quinn et al., 2006). However, the collection efficiency of organic mass may be lowered if the organic compounds are present on refractory particles with very low collection efficiencies, especially if the ratio of organic mass to refractory material is low. The CE of refractory material is not measurable since the AMS can only measure species that volatilize at the set operating temperature (600°C). In this case, only an independent measure of OM can provide an accurate determination of organic CE, similar to the correction applied to AMS sulfate by collocated, time-integrated ion chromatography.

The difference in OM between FTIR and AMS is correlated (r = 0.8) with the concentration of dust elements (nss-K, nss-Ca, Al, Si, Fe, and Ti) measured by XRF of Teflon filters (Fig. 3.6, inset). Aluminum and silicon are included here for above detection limit samples although they were not above detection in more than 20% of the samples and they are not included in Table 3.1. This relationship is consistent with the hypothesis that the reduced CE of AMS organic mass was caused by particles containing organic and dust components bouncing off the AMS vaporizer. Some of the difference in measured OM could also be attributed to organic components that were present on particles small enough to be sampled by FTIR but large enough to have less than 100% transmission into the AMS particle beam. Further, organic single particles identified with STXM-NEXAFS that were internally mixed with carbonate and potassium, corresponding to type "f" spectra (dust) in Takahama et al. (2007), represent 47 of the 96 submicron single particles analyzed. Other identified types include secondary (type "a"), biomass (types "i" and "j"), and combustion (an umbrella class including six particle types) (Fig. 3.7a). In previous studies, dust type single particles have composed less than 20% of the measured particles (Takahama et al., 2007). Figure 3.7b shows the average optical density spectrum of VOCALS organic-dust particles, with strong absorbances from carboxylic carbonyl, carbonate, and potassium. Using an algorithm developed by Takahama et al. (2010), the organic mass fraction of some particles identified as organic and dust mixtures was estimated to be 0.34±0.24 on average. The uncertainty associated with the estimated organic mass fraction depends on the homogeneity of the single particle mixture and varies widely over

the analyzed particles, but it is clear that the particles have significant dust fractions that may make them more susceptible to phase-dependent particle bounce in the AMS. These single particles were collected over a large geographical area and include measurements both near to and far from the continent making the small number of particles analyzed fairly representative of the regional submicron organic particle population.

Sulfate composed a large fraction of the observed submicron mass and has anthropogenic and marine sources. Ion chromatography of 12-24 hour filters was used to determine the average concentration of MSA (50 ± 22 ng m^{-3}). The continental sources of sulfate in South America include copper smelting, diesel, and coal combustion and appear to dominate the marine source of sulfate (oxidation of DMS) given the high coastal concentration of sulfate and the strong correlation with radon. In Figure 3.6b, the sum of inorganic sulfate (IC sulfate) and organic sulfate as in organosulfate groups ($COSO_3$) is compared with AMS sulfate. IC sulfate, unlike AMS sulfate, does not include organosulfate groups because IC sulfate is not fragmented before analysis. Sulfate from organosulfate groups is not distinguished from inorganic sulfate in the AMS due to fragmentation of the organosulfate molecule into an organic fragment and a sulfate fragment. A slightly more accurate CE for AMS sulfate is therefore determined by comparing it with the sum of organic and inorganic sulfate. The strong correlation (r = 0.98) and slope of 0.93 are consistent with the AMS CE of 1 for sulfate.

Further evidence of organic and sulfate components occurring on different particle populations is given in Figure 3.8. The negative correlation (r = -0.85 for all air masses) of the organic acid fraction of PM_1 with the sulfate fraction of PM_1 indicates that the two components result from different sources. For CAM only, the inverse relationship is stronger (r = -0.92). Conversely, the acid fraction of PM_1 is mildly correlated to the dust fraction of PM_1 (r = 0.70) in all air masses and is more strongly correlated (r = 0.85) for CAM only. As expected, continental air masses show higher correlations among continental emissions than the XAM and MAM air masses in which other source types reduce the correlation. These relationships, combined with single particle measurements and the observed
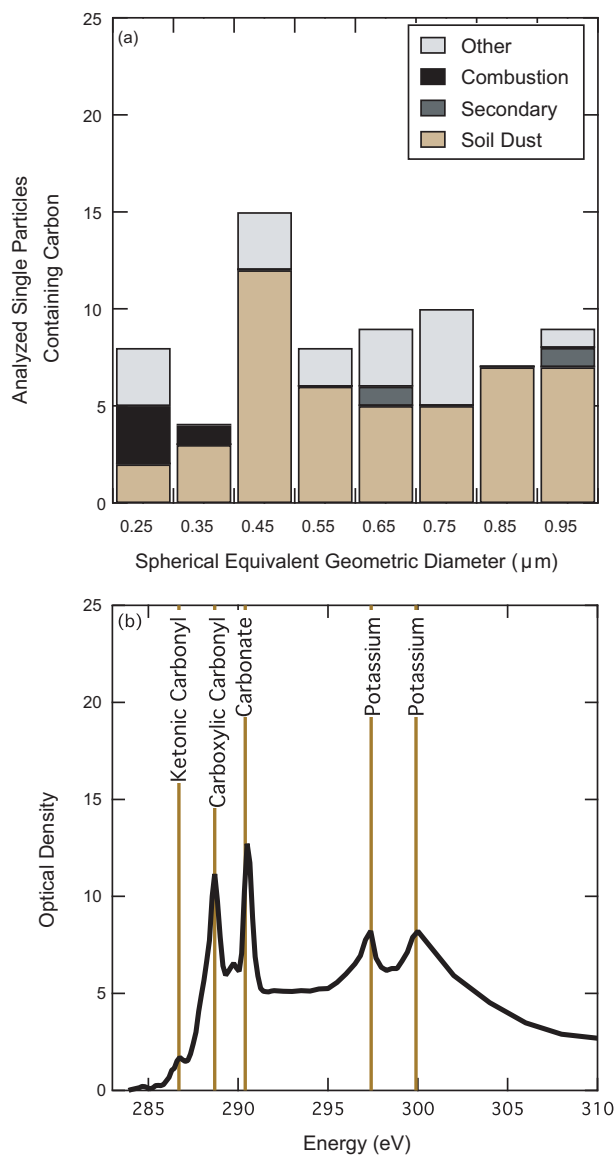
Figure 3.7: (a) 96 organic-containing single particles identified by STXM-NEXAFS binned by 0.1 μm size increments. Bar height shows the total number of particles identified at each size. (b) Average spectrum of individual submicron organic-containing particles classified as "dust", normalized by the average optical density between 305 and 320 eV. The average absorption of the pre-K edge portion of the spectrum (278-285 eV) was subtracted from all spectra. Vertical lines mark absorption peaks for organic and inorganic groups.
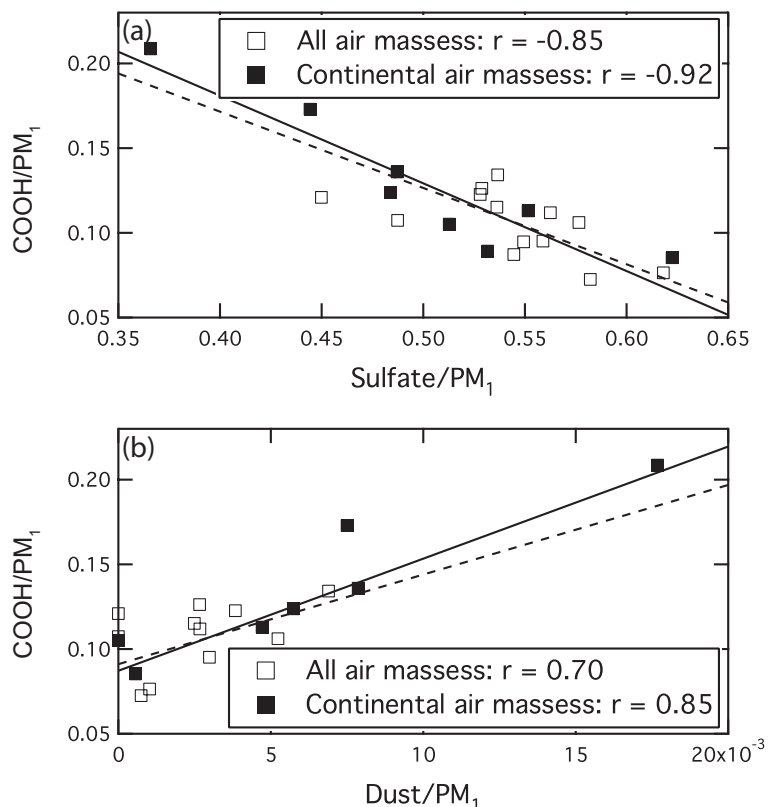
Figure 3.8: Comparison of acid fraction of PM_1 with (a) AMS sulfate and (b) dust fractions of PM_1.

differences in AMS CE for organic and sulfate components, suggest that much of the organic mass was not present on sulfate-containing particles.

3.4.5 Combustion and Marine Organic Aerosol Factors

Positive Matrix Factorization (PMF) was used to identify source factors from FTIR sample spectra (Paatero and Tapper, 1994) including only portions of the sample spectra with quantified peaks. One advantage of PMF is that the uncertainty associated with each measurement is included and used to constrain the determination of source factors. For each wavenumber, the standard deviation of the absorbance from all back filters was set as the measurement uncertainty. Results for 2, 3, 4, 5, and 6 factor solutions were explored and although the Q value (a normalized chi-square metric) was lowest for the 6-factor solution, a 2-factor solution was found to best represent the data. More than 2 factors resulted in factors

that were not linearly independent. Also, the XRF elemental correlations with the additional factors in the 3, 4, 5, and 6-factor solutions were nearly identical to the correlations with one of the two factors in the 2-factor solution, indicating factor-splitting beyond two factors (Ulbrich et al., 2009). The 2-factor solution was able to reproduce greater than 90% of the absorbance signal and greater than 75% of the organic mass, demonstrating that two factors are sufficient to represent most of the organic mixture features in the VOCALS-REx spectra. FPEAK (rotation) values from -0.4 to 0.4 were tested with the 2-factor solution but no significant difference was found among the rotations; FPEAK = 0 is presented here as a representative example. The two source spectra are shown in Figure 3.9 along with their average composition determined by integrating the factor spectra following the method for ambient spectra. The "Combustion" factor comprises mainly alkane (65%) and carboxylic acid (27%) groups and correlates with XRF measurements of sulfur, potassium, calcium, and metals while the "Marine" factor is over 70% organic hydroxyl and either weakly or inversely (if at all) correlated to the same elements (Table 3.2). Vanadium was weakly correlated to Marine OM and is emitted by residual oil combustion on ships and on land, so the small correlation observed is consistent with the interpretation of factor composition as "Marine". Figure 3.4c shows the fraction of organic mass associated with each factor for October and November 2008. The Combustion factor dominates the organic mass for most of the campaign. However, during some MAM periods, the fraction OM associated with the Marine factor is greater than 50%, illustrating the importance of marine organic sources to total OM in the remote marine atmosphere.

3.5   Discussion

3.5.1   Continental Sources of Organic, Inorganic, and Elemental Components

OM was an order of magnitude higher near the South American continent than in the remote marine atmosphere and correlations of OM with radon, sulfate
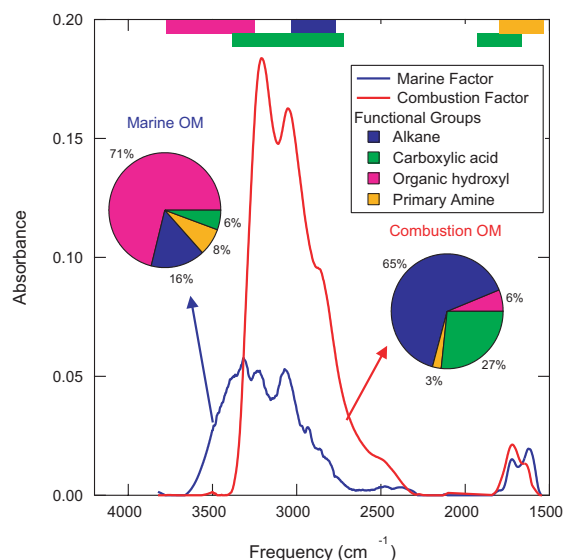
Figure 3.9: Positive Matrix Factorization of sample spectra resulted in two sources (Marine and Combustion) with representative FTIR spectra. As in Figure 3.3, colored bars across the top axis show the approximate range of absorbance of the functional groups. The average composition of each source is given in the two pie charts and corresponds to the values in Table 3.2.

and elements from dust or soil (Ca, Fe, and K), and industrial activities (S, V, Br, Ni, Sn) support an anthropogenic continental source of OM. Because air masses moved generally northward to the ship's location, measurements during CAM periods were likely influenced by urban centers along the Chilean coast south of the ship's track, such as Santiago. Artaxo et al. (1999) determined concentrations of elements in Santiago fine mode aerosol ($D_p < 2$ μm) using Particle-Induced X-ray Emission (PIXE). Samples were collected in two sites in downtown Santiago and several sources of PM_2 were identified by Absolute Principle Factor Analysis (APFA). The identified sources include sulfate (oxidized SO_2 from coal combustion) (64%), resuspended soil dust (15%), traffic emissions (16%), and oil combustion (2%). For consistency we will limit our comparison to elements in Table 3.1. Elements associated with the "Sulfates" factor are S, Sn, and K. Sn is not commonly found in urban aerosols but is particular to the soil in Chile which is enriched in Sn (Artaxo et al., 1999). Elements associated with "Oil Combustion" include Ni, V, and to a smaller extent, K, all of which were observed in our samples. Auto-

mobile and bus emissions are classified as the "Transport" factor and include Br, Sn, and K. Black carbon is most associated with the traffic emissions which are also the most likely anthropogenic source of organic compounds. Elements associated with the "Resuspended Soil Dust" factor are Ca and Fe. Resuspended soil dust in Santiago is contaminated with heavy metals and was observed by Artaxo et al. (1999) to be heavily mixed with traffic emissions. This observation is consistent with our single particle measurements of organic, carbonate, and potassium mixtures (Fig. 3.7) and with the hypothesis that much of the organic mass was present on refractory particles (Fig. 3.8b) rather than sulfate-containing particles. A second, biogenic continental source of OM from BVOC oxidation may exist in addition to anthropogenic sources described by Artaxo et al. (1999). For example, Elshorbany et al. (2009) found that isoprene contributed 16% of the photochemically produced formaldehyde in Santiago, Chile. In this study, VOC measurements were not available to determine if isoprene or other biogenic VOCs contributed to continentally-derived OM.

Other cities along the Chilean and Peruvian coast are likely to contribute to the observed OM, sulfate, and elemental components but Santiago is a large and likely representative source of the regional anthropogenic aerosol particles with over 50 μg m^{-3} PM$_2$ measured during the 1996 campaign. Artaxo et al. (1999) report sources of PM$_2$ specific to Santiago, Chile, that are similar to the measurements of inorganic and elemental components observed during VOCALS-REx. The proximity of Santiago to the back trajectories in the Continental samples and the magnitude of it as an emission source indicate that much of the observed organic mass associated with dust and metal components in our measurements originated from cities such as Santiago.

3.5.2 Marine Sources of Organic Components

During MAM periods and some XAM periods, OM was as low as 0.2 μg m^{-3} and had a significantly different functional group composition from CAM periods. The organic mass observed during MAM periods was dominated by the "Marine" factor, but was not purely biogenic marine OM given the small but detectable

amounts of ship emission tracers–Fe and V–in the submicron particles. Organic hydroxyl groups composed 71% of OM associated with the Marine factor compared to only 6% of OM in the Combustion factor and are found in polysaccharides and fatty alcohol molecules which, in addition to fatty acids, are some of the molecule types thought to be concentrated on the ocean's surface (Aluwihare et al., 1997). Biogenic organic compounds on the ocean's surface can be emitted to the atmosphere during bubble bursting (Blanchard and Syzdek, 1970; Hoffman and Duce, 1977; Tseng et al., 1992; Mochida et al., 2002; O'Dowd et al., 2004; Cavalli et al., 2004; Leck and Bigg, 2005; Russell et al., 2010). Russell et al. (2010) show a large contribution from a similar PMF-derived marine OM in the Arctic and North Atlantic and positive correlations between marine OM and sea salt. In addition, comparisons of PMF-derived marine factors (including the marine factor presented here) to reference di- and polysaccharides imply very similar composition, with large contributions from organic hydroxyl to the total organic mass (Russell et al., 2010).

3.5.3 Effect of Mixing Combustion and Marine Oxygenated Organic Aerosol on O/C

Observations of organic aerosols close to and more distant from particle sources generally show an increase in oxygenated groups such as carboxylic acids and a decrease in hydrophobic groups such as alkenes and alkanes with distance from source (Maria et al., 2004; Zhang et al., 2007; Gilardoni et al., 2007). Quantifying transformations of organic aerosol components such as oxidation of alkane, alkene, and aromatic groups to organic hydroxyl and carboxylic acid groups is often complicated in remote regions when multiple sources are mixed during transport and because some transformations are more rapid than others (Volkamer et al., 2006). A simplified proxy for photochemical aging is the atomic O/C ratio of organic aerosols, which increases with photochemical age due to an increasing fraction of oxidized chemical groups (Zhang et al., 2007; DeCarlo et al., 2007, 2008; Russell et al., 2009b). The usefulness of O/C in organic aerosol measurements has resulted in new efforts to measure O/C at high time resolution with the Aerodyne

Aerosol Mass Spectrometer (Aiken et al., 2007, 2008; DeCarlo et al., 2007). Elemental analysis (EA) of High Resolution (HR) mass spectra shows fairly good agreement with atomic O/C and H/C ratios for laboratory standards, although O/C in groups such as organic hydroxyl were under-predicted by as much as 50% (Aiken et al., 2007). The observed O/C ratio during VOCALS-REx from organic functional groups (FTIR) agrees with O/C estimated from the mass fraction of m/z 44 (AMS) for samples with the lowest organic hydroxyl group fractions ($<$ 15%), but is up to 5 times larger in samples with greater than 30% organic hydroxyl groups. This difference is most important in the more remote samples which have a smaller contribution from continental OM and larger contribution from marine OM, and therefore a larger fraction of organic hydroxyl groups. A recent comparison of organic functional groups and organic mass fragments has shown weak correlations between both carboxylic acid and organic hydroxyl groups and m/z 44 fraction (Russell et al., 2009a). Further, because O/C of the organic aerosol does not change significantly in the remote atmosphere it is not a relevant metric for photochemical age of transported particles. Consequently O/C does not represent a relevant metric for changes in the composition from atmospheric processing and is unlikely to provide a direct proxy for CCN activity or other aerosol properties.

3.5.4   Aqueous-Phase Formation of Organosulfate Groups

The contribution of SOA to total organic aerosol mass is variable even on small time and spatial scales and depends on a large number of factors including gas phase precursor concentrations, oxidant levels, time of day, and preexisting aerosol (Odum et al., 1996; Maria et al., 2004; Donahue et al., 2005), making model predictions of SOA challenging and often inaccurate when compared with measurements (Heald et al., 2005; De Gouw et al., 2005; Volkamer et al., 2006; Robinson et al., 2007). Identifying, separating, and quantifying SOA in ambient mixtures of primary and secondary organic aerosol is therefore a key step towards understanding the major formation pathways and the top parameters controlling SOA production. Recently several studies have highlighted the potentially important role of organosulfate formation in increasing SOA yield by increasing partitioning

of semi-volatile organic compounds (SVOCs) into the particle phase (Romero and Oehme, 2005; Iinuma et al., 2007; IInuma et al., 2007; Surratt et al., 2007b,a, 2008; Lukács et al., 2009; Altieri et al., 2009; Minerath and Elrod, 2009; Iinuma et al., 2009; Claeys et al., 2009). Claeys et al. (2009) found organosulfate compounds in fine aerosol in a marine environment with little continental influence, illustrating the importance of primary marine organic sources (fatty acid residues) and DMS-derived sulfate when no pollution sources exist. Galloway et al. (2009) identified organosulfate compounds in laboratory aerosol particles from reactive uptake of glyoxal onto ammonium sulfate seed aerosol under irradiated conditions. Altieri et al. (2009) found organosulfate compounds in rainwater samples that contained other compounds characteristic of SOA, such as organic acids. However, few quantitative ambient measurements of organosulfate compounds or groups exist, providing little basis for estimating the atmospheric importance of organosulfate groups relative to other secondary organic aerosol products, such as carboxylic acids (Maria and Russell, 2005; Gilardoni et al., 2007; Surratt et al., 2008; Lukács et al., 2009; Russell et al., 2009b). Size-segregated measurements of organosulfate in rural fine aerosol particles collected in Hungary show a peak in estimated organosulfate concentration (6-14% of total sulfate) for particle diameters near 400 nm coinciding with the typical peak in effective surface size distribution (Lukács et al., 2009), consistent with proposed heterogeneous mechanisms from laboratory studies (Surratt et al., 2007b,a; Minerath and Elrod, 2009; Iinuma et al., 2009). For the same study, Surratt et al. (2008) estimate that the organosulfate contribution to the total organic mass could be as high as 30%.

VOCALS-REx organosulfate group concentrations were more strongly associated with continental emissions than marine organics with 51 ng m^{-3} in CAM, 29 ng m^{-3} in XAM and 15 ng m^{-3} in MAM and composed up to 13% of OM and up to 9% of total sulfate. Our measurements show a strong positive correlation (r = 0.85) between organosulfate and sulfate fractions of PM$_1$ (Fig. 3.10a) and a strong inverse correlation (r = -0.87) between organosulfate and ammonium fractions of PM$_1$ (Fig. 3.10b), consistent with both particle-phase formation by reaction with condensed sulfate and acid catalysis. The highest observed organosulfate con-
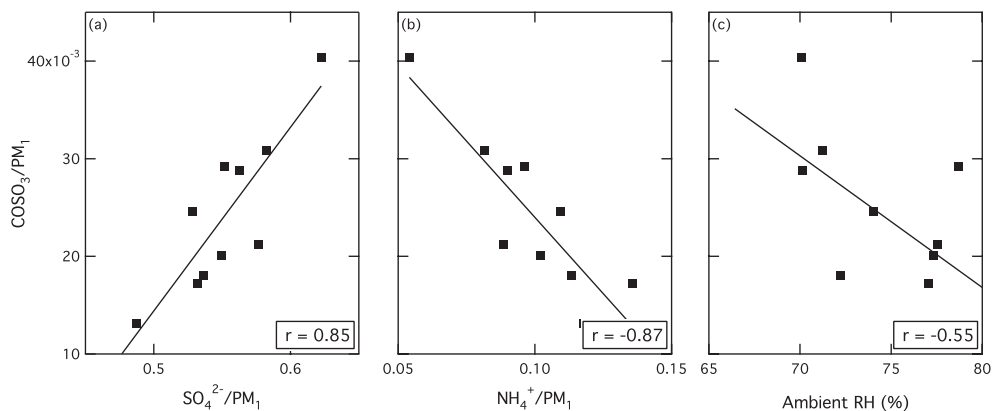
Figure 3.10: Comparison of organosulfate fraction of PM_1 with (a) AMS sulfate and (b) AMS ammonium fractions of PM_1. (c) Comparison of organosulfate fraction of PM_1 with ambient RH (%).

centration coincided with the peak sulfate concentration and the highest ratio of sulfate to ammonium measured. This is consistent with observations from Surratt et al. (2007b) and Minerath and Elrod (2009) of increased SOA yield with increasing acidity due to an acid hydrolysis mechanism for organosulfate formation of biogenic VOC oxidation products (epoxides). VOC precursors for organosulfate are most likely continental given the higher concentration of OM and specifically organosulfate groups in CAM. However, speciated VOC measurements are not available for the study period so it is not possible to separate biogenic and anthropogenic continental sources. Biogenic VOCs have been identified in Santiago, Chile (Elshorbany et al., 2009) though their contribution to formaldehyde was estimated to be only 16%.

Laboratory studies with glyoxal and inorganic seed aerosol under dark conditions by Liggio et al. (2005) show a stronger relationship between relative humidity (RH) and SOA yield than particle acidity. They observed little SOA formation below 50% RH, which they attribute to a reaction mechanism requiring aqueous dissolution of the organic VOC (*i.e.* glyoxal) prior to reaction. A significant increase in SOA yield was observed above 50% RH, however, at very high RH (above 80%) a small decrease in SOA yield was observed. This trend was attributed to the dilution of the hydrated glyoxal available as reactant and the reduction of the

particle acidity. Figure 3.10c shows the inverse relationship between organosulfate fraction of PM_1 with ambient relative humidity (r = -0.55) above 65% RH consistent with Liggio et al. (2005).

HYSPLIT back trajectories shown in Figure 3.2 indicate that even CAM samples had spent two to three days in the stratocumulus-topped MBL so cloud processing may also play a role in the observed organosulfate group concentrations. Other work has shown that cloud and fog processing may play a significant role in SOA formation through aqueous phase photooxidation of organic components (Blando and Turpin, 2000; Sorooshian et al., 2007; Perri et al., 2009). The VOCALS results are consistent with the role of aqueous particles in organosulfate production, but they suggest that higher amounts of liquid water associated with some cloud conditions may reduce the yield of organosulfate. However, ambient relative humidity was correlated with the ratio of ammonium to sulfate (r = 0.71) such that the driest conditions coincidentally had the most acidic sulfate aerosol. The tighter correlations of organosulfate fraction with sulfate implies that particle acidity had a more direct relationship with organosulfate formation than ambient RH for VOCALS-REx conditions (which were all at RH > 50%). The observed trends in VOCALS-REx organosulfate concentration suggest that in regions with similar conditions (*i.e.* RH above 50%, high sulfate concentrations relative to ammonium, and elevated VOC concentrations) organosulfate may have a significant contribution to SOA mass.

3.6   Conclusion

Organic functional groups measured in submicron particles showed higher carboxylic acid fractions (and lower organic hydroxyl fractions) in CAM than in MAM and no measurable change in O/C ratio with radon or distance from the continent, consistent with oxygenated organic groups from both marine and continental sources. OM associated with continental tracers such as radon, sulfate, and dust elements was on average 4 times that observed during periods of very low continental influence. In the most remote sampling location, OM associated with

the Marine factor was greater than 50% of the total OM measured by FTIR spectroscopy. Satellite measurements support the hypothesis that continental outflow is a significant source of aerosol to the region around 20°S; in situ measurements give estimated particle concentrations for the satellite AOD, while providing detailed size and chemistry information. A comparison of OM and O/C from FTIR spectroscopy and AMS showed that the AMS may have a reduced CE for organic mass on refractory particles and that m/z 44 fraction of OM may not accurately predict atomic O/C when organic hydroxyl composes a large fraction of OM.

Measurements in CAM show a strong positive correlation between carboxylic acid fraction and dust fractions of PM_1 and a strong negative correlation between carboxylic acid and sulfate fractions of PM_1, consistent with observed differences in AMS CE for organic and sulfate that indicate external mixtures of the two components. Previous measurements of submicron aerosol within Santiago show similar elemental signatures to those measured on board NOAA R/V *Ronald H. Brown* supporting the identification of this large source of PM_1. Organosulfate groups were frequently present in significant fractions of OM (3-13%) and correlated positively with sulfate fraction and inversely with ammonium fraction and ambient relative humidity, consistent with previously reported ambient and laboratory studies. Additional measurements of organic functional group concentrations would provide a more detailed, quantitative understanding of the sources and processes controlling submicron organic mass in the southeast Pacific MBL.

3.7 Acknowledgments

Table 3.1: Mean and Standard Deviation of Measured OM, Organic Functional Group, O/C, m/z 44 fraction, and Elemental Concentrations for VOCALS-REx and for Periods defined as CAM, XAM, and MAM.

	VOCALS-REx	CAM	XAM	MAM
Distance to Coast (km)	580 ± 230	370 ± 160	520 ± 240	670 ± 180
Average Radon (mBq m^{-3})	270 ± 200	530 ± 180	380 ± 180	110 ± 80
CN $<$ 80 nm (cm^{-3})	122 ± 90	100 ± 65	102 ± 55	154 ± 124
CN $>$ 80 nm (cm^{-3})	197 ± 102	305 ± 130	227 ± 114	149 ± 55
Average modal D_p (nm)[a]	340 ± 20	340 ± 16	340 ± 23	360 ± 19
FTIR OM (μg m^{-3})	0.59 ± 0.37	1.0 ± 0.5	0.71 ± 0.42	0.4 ± 0.17
AMS OM (μg m^{-3})	0.23 ± 0.10	0.29 ± 0.11	0.24 ± 0.10	0.17 ± 0.10
AMS SO$_4^{2-}$ (μg m^{-3})	0.93 ± 0.67	1.4 ± 1.0	1.1 ± 0.8	0.67 ± 0.33

[a]Average modal electrical mobility diameter of the accumulation mode volume-size distribution.

Table 3.1: Cont'd

	VOCALS-REx	CAM	XAM	MAM
FTIR Organic Functional Groups (μg m^{-3})				
Alkane	0.24 ± 0.16 (41%)	0.43 ± 0.20 (43%)	0.30 ± 0.19 (40%)	0.17 ± 0.09 (43%)
Carboxylic acid	0.19 ± 0.13 (32%)	0.34 ± 0.16 (34%)	0.23 ± 0.15 (33%)	0.11 ± 0.069 (29%)
Organic hydroxyl	0.12 ± 0.068 (20%)	0.16 ± 0.10 (16%)	0.14 ± 0.078 (20%)	0.088 ± 0.025 (22%)
Amine	0.015 ± 0.014 (3%)	0.023 ± 0.023 (2%)	0.019 ± 0.015 (3%)	0.0089 ± 0.0068 (2%)
Organosulfate	0.023 ± 0.047 (4%)	0.051 ± 0.085 (5%)	0.029 ± 0.058 (4%)	0.015 ± 0.019 (4%)
FTIR O/C (atomic)	0.62 ± 0.12	0.58 ± 0.073	0.63 ± 0.13	0.59 ± 0.13
FTIR OM/OC (mass)	2.0± 0.19	2.0 ± 0.11	2.1 ± 0.19	2.0 ± 0.20
AMS m/z 44 fraction (mass)	0.085 ± 0.057	0.14 ± 0.028	0.099 ± 0.052	0.023 ± 0.035
XRF Elements (ng m^{-3})				
S (μg m^{-3})	0.23 ± 0.15	0.42 ± 0.19	0.29 ± 0.17	0.15 ± 0.046
V	0.29 ± 0.18	0.43 ± 0.17	0.34 ± 0.172	0.12 ± 0.15
Br	0.39 ± 0.18	0.59 ± 0.25	0.43 ± 0.21	0.30 ± 0.083
Sn	5.9 ± 4.4	9.6 ± 6.5	7.8 ± 4.9	3.4 ± 1.5
Ni	1.1 ± 0.81	1.2 ± 0.82	1.3 ± 0.86	0.59 ± 0.13
K	7.0 ± 7.7	15 ± 12	9.4 ± 8.9	3.5 ± 3.0
Fe	1.3 ± 1.4	2.0 ± 1.8	1.6 ± 1.5	0.52 ± 0.18
Ca	1.7 ± 0.96	2.6 ± 1.1	2.0 ± 0.94	0.93 ± 0.42

Table 3.2: Organic functional group composition and elemental correlations for Positive Matrix Factorization (PMF) 2-Factor Analysis. Correlations stronger than 0.2 (and -0.2) are shown.

	Marine Factor	Combustion Factor
Average OM	0.11 ± 0.07	0.4 ± 0.3
Organic Composition (% mass)		
Alkane	16%	65%
Carboxylic acid	6%	27%
Organic hydroxyl	71%	6%
Amine	8%	3%
Elemental Correlations (r)		
S	-0.22	0.94
V	0.24	0.74
Sn	–	0.69
K	–	0.6
Br	–	0.82
Ni	–	0.28
Ca	–	0.38
Fe	–	0.62

References

Aiken, A. C., DeCarlo, P. F., Jimenez, J. L., 2007. Elemental analysis of organic species with electron ionization high-resolution mass spectrometry. Anal. Chem. 79 (21), 8350–8358.

Aiken, A. C., DeCarlo, P. F., Kroll, J. H., Worsnop, D. R., Huffman, J. A., Docherty, K., Ulbrich, I. M., Mohr, C., Kimmel, J. R., Sueper, D., et al., 2008. O/C and OM/OC Ratios of Primary, Secondary, and Ambient Organic Aerosols with High-Resolution Time-of-Flight Aerosol Mass Spectrometry. Environ. Sci. Technol. 42 (12), 4478–4485.

Alfarra, M. R., Coe, H., Allan, J. D., Bower, K. N., Boudries, H., Canagaratna, M. R., Jimenez, J. L., Jayne, J. T., Garforth, A. A., Li, S. M., et al., 2004. Characterization of urban and rural organic particulate in the Lower Fraser Valley using two Aerodyne Aerosol Mass Spectrometers. Atmos. Environ. 38 (34), 5745–5758.

Allan, J. D., Bower, K. N., Coe, H., Boudries, H., Jayne, J. T., Canagaratna, M. R., Millet, D. B., Goldstein, A. H., Quinn, P. K., Weber, R. J., et al., 2004. Submicron aerosol composition at Trinidad Head, California, during ITCT 2K2: Its relationship with gas phase volatile organic carbon and assessment of instrument performance. J. Geophys. Res. 109.

Altieri, K. E., Turpin, B. J., Seitzinger, S. P., 2009. Oligomers, organosulfates, and nitrooxy organosulfates in rainwater identified by ultra-high resolution electrospray ionization FT-ICR mass spectrometry. Atmos. Chem. Phys. 9, 2533–2542.

Aluwihare, L. I., Repeta, D. J., Chen, R. F., 1997. A major biopolymeric component to dissolved organic carbon in surface sea water. Nature 387 (6629), 166–169.

Andreae, M. O., 2009. Correlation between cloud condensation nuclei concentration and aerosol optical thickness in remote and polluted regions. Atmos. Chem. Phys. 9 (2), 543–556.

Artaxo, P., Oyola, P., Martinez, R., 1999. Aerosol composition and source apportionment in Santiago de Chile. Nuclear Instruments and Methods in Phys Res-Section B Only-Beam Interact Mater Atoms 150 (1), 409–416.

Bates, T. S., Quinn, P. K., Coffman, D., Schulz, K., Covert, D. S., Johnson, J. E., Williams, E. J., Lerner, B. M., Angevine, W. M., Tucker, S. C., et al., 2008. Boundary layer aerosol chemistry during TexAQS/GoMACCS 2006: Insights into aerosol sources and transformation processes. J. Geophys. Res. 113.

Bates, T. S., Quinn, P. K., Coffman, D. J., Johnson, J. E., Middlebrook, A. M., 2005. Dominance of organic aerosols in the marine boundary layer over the Gulf of Maine during NEAQS 2002 and their role in aerosol light scattering. J. Geophys. Res. 110.

Bates, T. S., Quinn, P. K., Covert, D. S., Coffman, D. J., Johnson, J. E., Wiedensohler, A., 2000. Aerosol physical properties and processes in the lower marine boundary layer: a comparison of shipboard sub-micron data from ACE-1 and ACE-2. Tellus B 52 (2), 258–272.

Blanchard, D. C., Syzdek, L., 1970. Mechanism for the water-to-air transfer and concentration of bacteria.

Blando, J. D., Turpin, B. J., 2000. Secondary organic aerosol formation in cloud and fog droplets: a literature evaluation of plausibility. Atmos. Environ. 34 (10), 1623–1632.

Bretherton, C. S., Uttal, T., Fairall, C. W., Yuter, S. E., Weller, R. A., Baumgardner, D., Comstock, K., Wood, R., Raga, G. B., 2004. The EPIC 2001 stratocumulus study. Bull. Am. Meteo rol. Soc. 85 (7), 967–977.

Cavalli, F., Facchini, M. C., Decesari, S., Mircea, M., Emblico, L., Fuzzi, S., Ceburnis, D., Yoon, Y. J., ODowd, C. D., Putaud, J. P., et al., 2004. Advances in characterization of size-resolved organic matter in marine aerosol over the North Atlantic. J. Geophys. Res. 109, 1–14.

Claeys, M., Wang, W., Vermeylen, R., Kourtchev, I., Chi, X., Farhat, Y., Surratt, J. D., Gómez-González, Y., Sciare, J., Maenhaut, W., 2009. Chemical characterisation of marine aerosol at Amsterdam Island during the austral summer of 2006–2007. J. of Aero. Sci.

De Gouw, J. A., Middlebrook, A. M., Warneke, C., Goldan, P. D., Kuster, W. C., Roberts, J. M., Fehsenfeld, F. C., Worsnop, D. R., Canagaratna, M. R., Pszenny, A. A. P., et al., 2005. Budget of organic carbon in a polluted atmosphere: Results from the New England Air Quality Study in 2002. J. Geophys. Res. 110.

DeCarlo, P. F., Dunlea, E. J., Kimmel, J. R., Aiken, A. C., Sueper, D., Crounse, J., Wennberg, P. O., Emmons, L., Shinozuka, Y., Clarke, A., et al., 2007. Fast airborne aerosol size and chemistry measurements with the high resolution aerosol mass spectrometer during the MILAGRO Campaign. Atmos. Chem. Phys. Discuss 7, 18269–18317.

DeCarlo, P. F., Dunlea, E. J., Kimmel, J. R., Aiken, A. C., Sueper, D., Crounse, J., Wennberg, P. O., Emmons, L., Shinozuka, Y., Clarke, A., et al., 2008. Fast airborne aerosol size and chemistry measurements above Mexico City and Central Mexico during the MILAGRO campaign. Atmos. Chem. Phys. 8, 4027–4048.

Donahue, N. M., Hartz, K. E. H., Chuong, B., Presto, A. A., Stanier, C. O., Rosenhørn, T., Robinson, A. L., Pandis, S. N., 2005. Critical factors determining the variation in SOA yields from terpene ozonolysis: A combined experimental and computational study. Faraday Discuss. 130, 295–309.

Drewnick, F., Schwab, J. J., Hogrefe, O., Peters, S., Husain, L., Diamond, D., Weber, R., Demerjian, K. L., 2003. Intercomparison and evaluation of four semi-continuous PM2. 5 sulfate instruments. Atmos. Environ. 37 (24), 3335–3350.

Elshorbany, Y. F., Kurtenbach, R., Wiesen, P., Lissi, E., Rubio, M., Villena, G., Gramsch, E., Rickard, A. R., Pilling, M. J., Kleffmann, J., 2009. Oxidation capacity of the city air of Santiago, Chile. Atmos. Chem. Phys 9, 2257–2273.

Ervens, B., Feingold, G., Kreidenweis, S. M., 2005. Influence of water-soluble organic carbon on cloud drop number concentration. J. Geophys. Res. 110.

Galloway, M. M., Chhabra, P. S., Chan, A. W. H., Surratt, J. D., Flagan, R. C., Seinfeld, J. H., Keutsch, F. N., 2009. Glyoxal uptake on ammonium sulphate seed aerosol: reaction products and reversibility of uptake under dark and irradiated conditions. Atmos. Chem. Phys 9, 3331–3345.

Garreaud, R. D., Muñoz, R. C., 2005. The low-level jet off the west coast of subtropical South America: Structure and variability. Monthly Weather Review 133 (8), 2246–2261.

Gilardoni, S., Russell, L. M., Sorooshian, A., Flagan, R. C., Seinfeld, J. H., Bates, T. S., Quinn, P. K., Allan, J. D., Williams, B., Goldstein, A. H., et al., 2007. Regional variation of organic functional groups in aerosol particles on four US east coast platforms during the International Consortium for Atmospheric Research on Transport and Transformation 2004 campaign. J. Geophys. Res. 112.

Gilardoni, S., Shang, L., Takahama, S., Russell, L. M., Allan, J. D., Steinbrecher, R., Jimenez, J. L., Decarlo, P. F., Dunlea, E. J., Baumgardner, D., 2009. Characterization of organic ambient aerosol during MIRAGE 2006 on three platforms. Atmospheric Chemistry and Physics Discussions 9 (2), 6617–6655.

Hawkins, L. N., Russell, L. M., Twohy, C. H., Anderson, J. R., 2008. Uniform particle-droplet partitioning of 18 organic and elemental components measured in and below DYCOMS-II stratocumulus clouds. J. Geophys. Res. 113.

Heald, C. L., Jacob, D. J., Park, R. J., Russell, L. M., Huebert, B. J., Seinfeld, J. H., Liao, H., Weber, R. J., 2005. A large organic aerosol source in the free troposphere missing from current models. Geophys. Res. Lett. 32, 18.

Hoffman, E. J., Duce, R. A., 1977. Organic carbon in marine atmospheric particulate matter- Concentration and particle size distribution. Geophys. Res. Lett. 4, 449–452.

Huneeus, N., Gallardo, L., Rutllant, J. A., 2006. Offshore transport episodes of anthropogenic sulfur in northern Chile: Potential impact on the stratocumulus cloud deck. Geophys. Res. Lett. 33 (19).

Iinuma, Y., Böge, O., Kahnt, A., Herrmann, H., 2009. Laboratory chamber studies on the formation of organosulfates from reactive uptake of monoterpene oxides. Phys. Chem. Chem. Phys. 11 (36), 7985–7997.

IInuma, Y., Müeller, C., Berndt, T., Böege, O., Claeys, M., Herrmann, H., 2007. Evidence for the Existence of Organosulfates from beta 2-Pinene Ozonolysis in Ambient Secondary Organic Aerosol. Environ. Sci. Tech. 41 (19), 6678–6683.

Iinuma, Y., Müller, C., Böge, O., Gnauk, T., Herrmann, H., 2007. The formation of organic sulfate esters in the limonene ozonolysis secondary organic aerosol (SOA) under acidic conditions. Atmos. Environ. 41 (27), 5571–5583.

Jayne, J. T., Leard, D. C., Zhang, X., Davidovits, P., Smith, K. A., Kolb, C. E., Worsnop, D. R., 2000. Development of an aerosol mass spectrometer for size and composition analysis of submicron particles. Aerosol Sci. Technol. 33 (1), 49–70.

Jimenez, J. L., Jayne, J. T., Shi, Q., Kolb, C. E., Worsnop, D. R., Yourshaw, I., Seinfeld, J. H., Flagan, R. C., Zhang, X., Smith, K. A., et al., 2003. Ambient aerosol sampling using the aerodyne aerosol mass spectrometer. J. Geophys. Res. 108 (D7), 8425.

Johnson, K. S., Zuberi, B., Molina, L. T., Molina, M. J., Iedema, M. J., Cowin, J. P., Gaspar, D. J., Wang, C., Laskin, A., 2005. Processing of soot in an urban environment: case study from the Mexico City Metropolitan Area. Atmos. Chem. Phys. 5 (11), 3033–3043.

Leck, C., Bigg, E. K., 2005. Source and evolution of the marine aerosol A new perspective. Geophys. Res. Lett. 32 (19), L19803.

Liggio, J., Li, S. M., McLAREN, R., 2005. Heterogeneous reactions of glyoxal on particulate matter: Identification of acetals and sulfate esters. Environ. Sci. Technol. 39 (6), 1532–1541.

Liu, S., Takahama, S., Russell, L. M., Gilardoni, S., Baumgardner, D., 2009. Oxygenated organic functional groups and their sources in single and submicron organic particles in MILAGRO 2006 campaign. Atmos. Chem. Phys. Discuss. 9, 4567–4607.

Lukács, H., Gelencsér, A., Hoffer, A., Kiss, G., Horváth, K., Hartyáni, Z., 2009. Quantitative assessment of organosulfates in size-segregated rural fine aerosol. Atmos. Chem. Phys. 9, 231–238.

Maria, S. F., Russell, L. M., 2005. Organic and inorganic aerosol below-cloud scavenging by suburban New Jersey precipitation. Environ. Sci. Technol. 39 (13), 4793–4800.

Maria, S. F., Russell, L. M., Gilles, M. K., Myneni, S. C. B., 2004. Organic aerosol growth mechanisms and their climate-forcing implications.

Maria, S. F., Russell, L. M., Turpin, B. J., Porcja, R. J., 2002. FTIR measurements of functional groups and organic mass in aerosol samples over the Caribbean. Atmos. Environ. 36 (33), 5185–5196.

Maria, S. F., Russell, L. M., Turpin, B. J., Porcja, R. J., Campos, T. L., Weber, R. J., Huebert, B. J., 2003. Source signatures of carbon monoxide and organic functional groups in Asian Pacific Regional Aerosol Characterization Experiment (ACE-Asia) submicron aerosol types. J. Geophys. Res. 108, 8637.

Matthew, B. M., Middlebrook, A. M., Onasch, T. B., 2008. Collection efficiencies in an Aerodyne aerosol mass spectrometer as a function of particle phase for laboratory generated aerosols. Aerosol Sci. Technol. 42 (11), 884–898.

Minerath, E. C., Elrod, M. J., 2009. Assessing the potential for diol and hydroxy sulfate ester formation from the reaction of epoxides in tropospheric aerosols. Environ. Sci. Tech. 43 (5), 1386.

Mochida, M., Kitamori, Y., Kawamura, K., Nojiri, Y., Suzuki, K., 2002. Fatty acids in the marine atmosphere: Factors governing their concentrations and evaluation of organic films on sea-salt particles. J. Geophys. Res. 107 (D17), 4325.

O'Dowd, C. D., Becker, E., Kulmala, M., 2001. Mid-latitude North-Atlantic aerosol characteristics in clean and polluted air. Atmos. Res. 58 (3), 167–185.

O'Dowd, C. D., Facchini, M. C., Cavalli, F., Ceburnis, D., Mircea, M., Decesari, S., Fuzzi, S., Yoon, Y. J., Putaud, J. P., 2004. Biogenically driven organic contribution to marine aerosol. Nature 431 (7009), 676–680.

Odum, J. R., Hoffmann, T., Bowman, F., Collins, D., Flagan, R. C., Seinfeld, J. H., et al., 1996. Gas/particle partitioning and secondary organic aerosol yields. Environ. Sci. Technol. 30 (8), 2580–2585.

Paatero, P., Tapper, U., 1994. Positive matrix factorization: A non-negative factor model with optimal utilization of error estimates of data values. Environmetrics 5 (2), 111–126.

Perri, M. J., Seitzinger, S., Turpin, B. J., 2009. Secondary organic aerosol production from aqueous photooxidation of glycolaldehyde: Laboratory experiments. Atmos. Environ. 43 (8), 1487–1497.

Pirjola, L., O'Dowd, C. D., Brooks, I. M., Kulmala, M., 2000. Can new particle formation occur in the clean marine boundary layer? J. Geophys. Res. 105 (D21), 26531–26546.

Prenni, A. J., Petters, M. D., Kreidenweis, S. M., DeMott, P. J., Ziemann, P. J., 2007. Cloud droplet activation of secondary organic aerosol. J. Geophys. Res. 112, D10223.

Quinn, P. K., Bates, T. S., Coffman, D., Onasch, T. B., Worsnop, D., Baynard, T., De Gouw, J. A., Goldan, P. D., Kuster, W. C., Williams, E., et al., 2006. Impacts of sources and aging on submicrometer aerosol properties in the marine boundary layer across the Gulf of Maine. J. Geophys. Res. 111.

Quinn, P. K., Bates, T. S., Coffman, D. J., Covert, D. S., 2008. Influence of particle size and chemistry on the cloud nucleating properties of aerosols. Atmos. Chem. Phys. 8, 1029–1042.

Quinn, P. K., Kapustin, V. N., Bates, T. S., Covert, D. S., 1996. Chemical and optical properties of marine boundary layer aerosol particles of the mid-Pacific in relation to sources and meteorological transport. J. Geophys. Res. 101 (D3).

Remer, L. A., Tanré, D., Kaufman, Y. J., Ichoku, C., Mattoo, S., Levy, R., Chu, D. A., Holben, B. .N .and Dubovik, O., Smirnov, A., et al., 2002. Validation of MODIS aerosol retrieval over ocean. Geophys. Res. Lett. 29 (12), 8008.

Richter, I., Mechoso, C. R., 2006. Orographic influences on subtropical stratocumulus. J. Atmos. Sci. 63 (10), 2585–2601.

Robinson, A. L., Donahue, N. M., Shrivastava, M. K., Weitkamp, E. A., Sage, A. M., Grieshop, A. P., Lane, T. E., Pierce, J. R., Pandis, S. N., 2007. Rethinking organic aerosols: Semivolatile emissions and photochemical aging. Science 315 (5816), 1259.

Romero, F., Oehme, M., 2005. Organosulfates–A New Component of Humic-Like Substances in Atmospheric Aerosols? J. of Atmos. Chem. 52 (3), 283–294.

Russell, L., Bahadur, R., Hawkins, L., Allan, J., Baumgardner, D., Quinn, P., Bates, T., 2009a. Organic aerosol characterization by complementary measurements of chemical bonds and molecular fragments. Atmospheric Environment 43, 6100–6105.

Russell, L. M., 2003. Aerosol organic-mass-to-organic-carbon ratio measurements. Environ. Sci.Technol. 37 (13), 2982–2987.

Russell, L. M., Hawkins, L. N., Frossard, A. A., Quinn, P. K., Bates, T. S., 2010. Carbohydrate-Like Composition of Submicron Atmospheric Particles and their Production from Ocean Bubble Bursting. Proc. Nat. Acad. Sci.

Russell, L. M., Takahama, S., Liu, S., Hawkins, L. N., Covert, D. S., Quinn, P. K., Bates, T. S., 2009b. Oxygenated fraction and mass of organic aerosol from direct emission and atmospheric processing measured on the R/V Ronald Brown during TEXAQS/GoMACCS 2006. J. Geophys. Res. 114 (null).

Seinfeld, J. H., Erdakos, G. B., Asher, W. E., Pankow, J. F., 2001. Modeling the Formation of Secondary Organic Aerosol (SOA). 2. The Predicted Effects of Relative Humidity on Aerosol Formation in the α-Pinene-,β-Pinene-, Sabinene-,δ 3-Carene-, and Cyclohexene-Ozone Systems. Environ. Sci. Technol. 35 (9), 1806–1817.

Sorooshian, A., Lu, M. L., Brechtel, F. J., Jonsson, H., Feingold, G., Flagan, R. C., Seinfeld, J. H., 2007. On the source of organic acid aerosol layers above clouds. Environ. Sci. Technol. 41 (13), 4647–4654.

Surratt, J. D., Gmez-Gonzlez, Y., Chan, A. W. H., Vermeylen, R., Shahgholi, M., Kleindienst, T. E., Edney, E. O., Offenberg, J. H., Lewandowski, M., Jaoui, M., et al., 2008. Organosulfate formation in biogenic secondary organic aerosol. J. Phys. Chem. A 112 (36), 8345–8378.

Surratt, J. D., Kroll, J. H., Kleindienst, T. E., Edney, E. O., Claeys, M., Sorooshian, A., Ng, N. L., Offenberg, J. H., Lewandowski, M., Jaoui, M., et al., 2007a. Evidence for organosulfates in secondary organic aerosol. Environ. Sci. Technol. 41 (2), 517–527.

Surratt, J. D., Lewandowski, M., Offenberg, J. H., Jaoui, M., Kleindienst, T. E., Edney, E. O., Seinfeld, J. H., 2007b. Effect of acidity on secondary organic aerosol formation from isoprene. Environ. Sci. Technol. 41 (15), 5363–5369.

Takahama, S., Gilardoni, S., Russell, L. M., Kilcoyne, A. L. D., 2007. Classification of multiple types of organic carbon composition in atmospheric particles by scanning transmission X-ray microscopy analysis. Atmos. Environ. 41 (40), 9435–9451.

Takahama, S., Liu, S., Russell, L. M., 2010. Coatings and clusters of carboxylic acids in carbon-containing atmospheric particles from spectromicroscopy and their implications for cloud-nucleating and optical properties. J. Geophys. Res. *In press.*

Tseng, R., Viechnicki, J. T., Skop, R. A., Brown, J. W., 1992. Sea-to-air transfer of surface-active organic compounds by bursting bubbles. J. Geophys. Res. 97 (C4).

Twohy, C. H., Petters, M. D., Snider, J. R., Stevens, B., Tahnk, W., Wetzel, M., Russell, L., Burnet, F., 2005. Evaluation of the aerosol indirect effect in marine stratocumulus clouds: Droplet number, size, liquid water path, and radiative impact. J. Geophys. Res. 110.

Ulbrich, I. M., Canagaratna, M. R., Zhang, Q., Worsnop, D. R., Jimenez, J. L., 2009. Interpretation of organic components from positive matrix factorization of aerosol mass spectrometric data. Atmos. Chem. Phys. 9, 2891–2918.

Volkamer, R., Jimenez, J. L., San Martini, F., Dzepina, K., Zhang, Q., Salcedo, D., Molina, L. T., Worsnop, D. R., Molina, M. J., 2006. Secondary organic aerosol formation from anthropogenic air pollution: Rapid and higher than expected. Geophys. Res. Lett. 33, 17.

Ward Jr, J. H., 1963. Hierarchical grouping to optimize an objective function. J. Am. Stat. Assoc., 236–244.

Zhang, Q., Canagaratna, M. R., Jayne, J. T., Worsnop, D. R., Jimenez, J. L., 2005a. Time-and size-resolved chemical composition of submicron particles in Pittsburgh: Implications for aerosol sources and processes. J. Geophys. Res. 110.

Zhang, Q., Jimenez, J. L., Canagaratna, M. R., Allan, J. D., Coe, H., Ulbrich, I., Alfarra, M. R., Takami, A., Middlebrook, A. M., Sun, Y. L., et al., 2007. Ubiquity and dominance of oxygenated species in organic aerosols in anthropogenically-influenced Northern Hemisphere midlatitudes. Geophys. Res. Lett. 34.

Zhang, Q., Worsnop, D. R., Canagaratna, M. R., Jimenez, J. L., 2005b. Hydrocarbon-like and oxygenated organic aerosols in Pittsburgh: Insights into sources and processes of organic aerosols. Atmos. Chem. Phys. 5, 3289–3311.

Chapter 4

The Effect of Increased Organic Solubility on Predicted CCN Activity in the Anthropogenically-Influenced Marine Boundary Layer

Abstract. Aerosol particles in the marine boundary layer (MBL) are transported from their source region and processed in the atmosphere, and are therefore often mixtures of inorganic (*e.g.* $SO_4{}^{2-}$, $NH_4{}^+$, and $NO_3{}^-$) and organic components (*e.g.* carboxylic acid, hydroxyl, and saturated aliphatic functional groups). Although the solubility of inorganic aerosol components is fairly well known, the large number of unknown organic compounds present in ambient aerosol, in combination with their wide variety of hygroscopic properties, makes CCN activity of mixtures difficult to constrain. Here we present predicted CCN

concentrations using recent measurements of submicron aerosol organic functional groups from the stratocumulus-topped MBL in the southeast Pacific Ocean. The particles included both hydrophobic (saturated aliphatic C-CH) and hydrophilic (carboxylic acid COOH and hydroxyl COH) groups, in addition to small amounts of amine $C-NH_2$ and organosulfate $COSO_3$ groups. These measurements have been coupled with simultaneous measurements of particle size, inorganic elements, and inorganic ions to predict CCN activity of the ambient aerosol using a multi-component Köhler model. The model calculations show that CCN concentrations at 0.3% supersaturation are sensitive to the solubility of the organic fraction for the particle sizes observed during VOCALS-REx and that the sensitivity is inversely correlated with particle size below 180 nm. Above 180 nm, predicted ratios of CCN/CN are close to 100% for all compositions. For the smallest particles, a 1% increase in average solubility resulted in a 6% increase in the fraction of activated particles. Predicted CCN concentrations in the region of highest continental influence (less than 600 km from shore) are highest and most sensitive to composition because of smaller particle size. The coastal region also has smaller effective cloud drop radii based on satellite observations from the Geostationary Operational Environmental Satellite (GOES-10) as expected in an area with elevated CCN.

4.1 Introduction

The extent to which aerosols impact cloud optical properties, lifetime, and precipitation patterns by acting as cloud condensation nuclei (CCN) is controlled by their ability to grow in a saturated air parcel (hygroscopic growth), which in turn is controlled by their size and chemical composition (Köhler, 1936; Roberts et al., 2002; Quinn et al., 2008). In conditions with high supersaturations or for particles of uniform composition, particle size may be more critical for predicting accurate CCN concentrations (Dusek et al., 2006; Hawkins et al., 2008). For low supersaturations, when composition varies with size, or when particles are small, both particle size and composition are relevant (Nenes et al., 2002; Roberts et al., 2002). Organic components in ambient aerosol range from non-polar (hydrocarbons) to polar (carboxylic acids) (Maria et al., 2002, 2003; Russell et al., 2009; Hawkins et al., 2010) in varying proportions but are often treated as insoluble in CCN studies due to insufficient chemically specific measurements to constrain estimates of solubility. However, the presence of organic compounds can drastically reduce or increase CCN concentrations by lowering solubility, increasing molecular weight, and suppressing surface tension (Ervens et al., 2005; Chan et al., 2008). Fourier Transform Infrared (FTIR) spectroscopy permits us to constrain solubility of the organic mass based on functional group contribution to total organic mass (OM).

The southeastern Pacific Ocean is dominated by marine stratocumulus clouds, which generally have low supersaturations (around 0.3%) (Martin et al., 1994).Typically the marine atmosphere also has low background particle concentrations (O'Dowd and de Leeuw, 2007; Hawkins et al., 2008). Because of this, marine stratocumulus clouds are sensitive to additional CCN (Albrecht, 1989) such that even small perturbations to the existing concentration of CCN may have a significant impact on cloud reflectivity and lifetime.

The specific conditions for which particle composition and organic solubility are relevant will vary with the chemical and physical properties of the aerosol and with supersaturation and cannot be strictly defined. For this reason, thermodynamic models are needed to understand how or if small scale changes in size and

composition affect CCN concentration. Here we use a multi-component Köhler model described by Roberts et al. (2002) to investigate the potential importance of constraining organic composition with functional group fraction on predicted CCN concentrations for the range of observed particle concentrations and chemical compositions in the low supersaturation (SS) environment of the southeast Pacific marine boundary layer.

4.2 Methods

4.2.1 Sample Collection

Submicron particles were measured at 5-minute intervals by an Aerodyne Quadrupole Aerosol Mass Spectrometer (Q-AMS) through an isokinetic sampling inlet located on the forward deck of the R/V *Ronald H. Brown* approximately 18 m above sea level (Quinn et al., 2008; Bates et al., 2008). The sample line was partitioned to collect particles on filters located downstream of a 1 μm sharp-cut cyclone (SCC 2.229 PM1, BGI Inc.) in a temperature and humidity controlled enclosure. Samples were collected on 37 mm teflon filters (Pall Inc.) over 12 to 24 hours (short samples) with simultaneous 24 hour (duplicate and long samples) for offline FTIR spectroscopic and X-ray Fluorescence (XRF) analyses. Particle size distributions were measured with a Differential Mobility Particle Sizer (DMPS) from the shared sampling inlet.

4.2.2 Fourier Transform Infrared Spectrosocpy (FTIR) and X-Ray Fluorescence (XRF)

FTIR samples were kept at 0^oC prior to FTIR spectroscopic analysis to reduce evaporative losses of organic compounds and to reduce artifacts from condensed-phase chemical reactions. Infrared absorbance spectra of each sample and blank filter were measured non-destructively using a Bruker Tensor 27 spectrometer with RT-DLATGS detector (Gilardoni et al., 2007) and were interpreted using a revised algorithm (Russell et al., 2009) and calibration standards (Maria et al., 2002, 2003;

Maria and Russell, 2005; Gilardoni et al., 2007). Quantified organic functional groups include saturated aliphatic C-CH (alkane), non-acidic hydroxyl C-OH (alcohol), primary amine C-NH$_2$, carboxylic acid COOH, and organosulfate COSO$_3$ groups. Non-acidic carbonyl C=O, aromatic C=C-H, and unsaturated aliphatic C=C-H (alkene) groups were below detection limit in all samples and were not included in this analysis. X-ray fluorescence on the teflon filters was completed by Chester Labnet (Tigard, Oregon) and provided concentrations of elements heavier than neon (Maria et al., 2002, 2003; Gilardoni et al., 2007; Russell et al., 2009).

4.2.3 Quadrupole Aerosol Mass Spectrometry

The Aerodyne Quadrupole Aerosol Mass Spectrometer (Q-AMS) measures bulk non-refractory submicron aerosol chemistry and component-specific size distributions in real-time at 5-minute resolution (Jayne et al., 2000; Jimenez et al., 2003). The instrument comprises a Time-of-Flight (ToF) sizing inlet followed by a 600°C vaporizer and electron impact ionizer. From there the sample is analyzed using a quadrupole mass spectrometer with 1 amu resolution. Quantified components include SO$_4{}^{2-}$, NO$_3{}^-$, NH$_4{}^+$, and organic mass fragments.

4.2.4 Multi-Component Köhler Model for Calculating CCN at 0.3% SS

The Köhler equation (Seinfeld and Pandis, 1998) (Eq. 4.1) relates particle size and composition to the supersaturation at which droplet nucleation is thermodynamically favorable and consists of the Kelvin term, which accounts for the increased equilibrium vapor pressure over a curved surface relative to a flat plane, and the Raoult term, which accounts for the decreased equilibrium vapor pressure over salt solutions relative to pure water:

$$ln(\frac{p_w(D_p)}{p_o}) = \frac{4M_w\sigma_w}{RT\rho_wD_p} - \frac{6n_sM_w}{\pi\rho_wD_p^3} \qquad (4.1)$$

where ρ_w and ρ_o are the densities of pure water and the relevant solution, D_p is the particle diameter, M_w is the molecular weight of water, σ is the surface tension of

the solution, and n_s is the number of moles of solute. Using the general form of the Köhler equation it is not trivial to include multiple solutes, especially those with widely varying solubilities and surface tensions. For this application, a modified Köhler equation is necessary.

Predicted CCN concentrations are calculated using a multi component Köhler model (Roberts et al., 2002) for three case studies: (1) a 1-component NH_4HSO_4 only model, (2) a 3-component model including NH_4HSO_4, insoluble organics, and insoluble inorganics (dust), and (3) a 4-component model including NH_4HSO_4, insoluble organics, dust, and slightly soluble organics. AMS NH_4^+ and SO_4^{2-} were present at approximately a 1:1 molar ratio are treated as NH_4HSO_4 in all three cases for simplicity. AMS NO_3^- was very low and is not included in this analysis. Elemental components from sea salt (Na, Cl) were below detection limit in greater than 80% of the samples. Elements above detection limit in greater than 20% of samples include Sn, V, Fe, K, Br, Ca, Al, Cr, and Ni; these elements are treated as "dust" (completely insoluble) in the second and third model calculations for simplicity. This assumption is not likely to affect the model prediction given that the elements make up between 1% and 6% of the submicron particulate mass (PM_1). The organic fraction (from FTIR spectroscopy) is treated as "insoluble organic" in Case 2, then partitioned by functional group into two categories for Case 3. Alkane and amine groups are treated as "insoluble organic"; acid, alcohol, and organosulfate groups are treated as "soluble organic" (using the solubility of adipic acid, 0.06 g mL^{-1} water). The measured organic mass was approximately evenly split between soluble and insoluble groups. The DMPS size distributions were used to determine appropriate model inputs (geometric mean diameter, geometric standard deviation, and number concentration) for particles above 80 nm. Some periods were characterized by bimodal number distributions with a significant number fraction of total particles below 80 nm. Only the larger mode was included in the model input due to the model limitation of unimodal particle distribution and the low fraction of even completely soluble particles activating below 80 nm at 0.3% supersaturation. CCN concentrations are compared for the 3 conditions at 0.3% SS, in the range of (estimated) SS of southeast Pacific

marine stratocumulus (0.2% to 0.4%) (Hoppel et al., 1994; Tomlinson et al., 2007) and the SS of collated CCN measurements.

4.3 Predicted CCN concentrations for 3 Compositions at 0.3% SS

Table 4.1 shows the predicted CCN concentrations and activated fractions (CCN/CN) for each of the three cases ordered by distance from the coast. For the 1-component model (Case 1) that assumes 100% NH_4HSO_4, most samples were predicted to have over 90% of the particles activate at 0.3% SS. For the 3-component model (Case 2) that assumes all organics are insoluble, some samples have as low as 71% of the particles activating, which corresponds to a maximum drop in CCN from Case 1 of about 50 cm^{-3}. For the 4-component model (Case 3) that separates the organic fraction into slightly soluble and insoluble, the activated fractions are slightly higher than those of Case 2 but still significantly lower than those of Case 1.

Figure 4.1 shows the dependence of CCN concentration on distance from the coast. The small change in predicted CCN number between the 3 cases indicates that decrease in total particle concentration (through dilution) is driving the geographic distribution of CCN, though the absolute number of CCN at each location is sensitive to particle chemistry (Table 4.1). Figure 4.2 shows the spatial distribution of CCN for Case 3 in relation to satellite images of cloud drop effective radius and liquid water path and is discussed further in the next section. Figure 4.3 shows the dependence of activated fraction on mean particle size. The model calculations show that particle size is most important when the fraction of soluble material is lowest, as indicated by the steeper slope for Case 2. For sizes above 180 nm, the particle composition does not have a significant impact on predicted CCN.

Table 4.1: Predicted CCN (cm^{-3}) and activated fraction in each of the three cases for the 21 samples, in order of increasing distance from the coast.

Composition	Case 1 NH$_4$HSO$_4$		Case 2 NH$_4$HSO$_4$, Dust, and Insol. Organic		Case 3 NH$_4$HSO$_4$, Dust, Slightly sol. and Insol. Organic	
Distance (km)	CCN	CCN/CN	CCN	CCN/CN	CCN	CCN/CN
171	445	0.94	419	0.89	431	0.91
221	360	0.93	336	0.87	342	0.88
244	274	0.86	226	0.71	240	0.75
350	231	0.94	213	0.87	217	0.88
386	133	0.98	129	0.95	131	0.97
387	179	0.96	170	0.91	173	0.92
391	447	0.92	402	0.83	420	0.87
392	237	1.00	234	0.98	235	0.99
423	237	0.97	229	0.94	231	0.95
425	119	0.96	113	0.92	116	0.94
425	206	0.93	191	0.86	195	0.88
453	116	0.97	111	0.92	114	0.94
500	203	0.95	193	0.90	195	0.91
575	170	0.95	157	0.88	162	0.91
670	150	0.98	145	0.95	146	0.95
701	116	0.96	111	0.92	114	0.94
704	123	0.97	118	0.93	120	0.95
890	101	0.97	97	0.93	98	0.94
1061	85	0.97	81	0.92	83	0.94
1088	49	0.95	45	0.89	47	0.91
1162	65	0.88	54	0.74	58	0.78
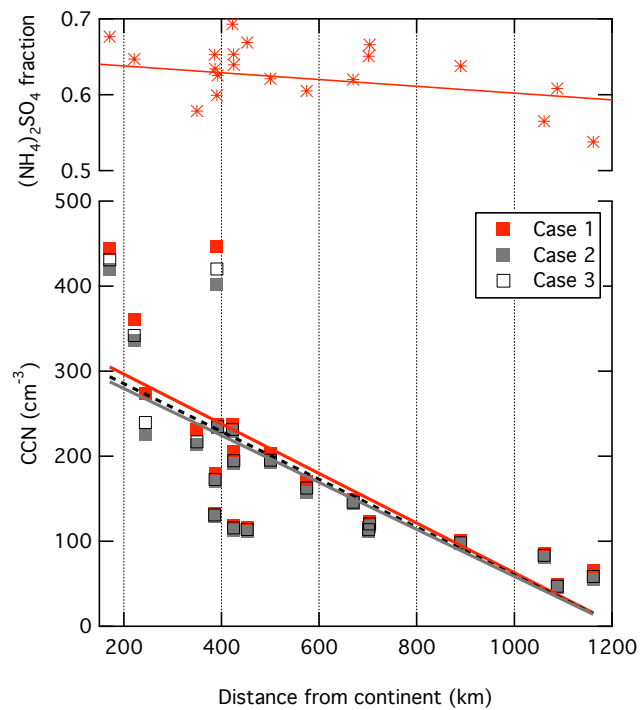
Figure 4.1: (a) Fraction of NH_4HSO_4 (Cases 2 and 3 only) and mean particle diameter compared with distance from the continent. (b) Predicted CCN concentration compared with distance from the continent.
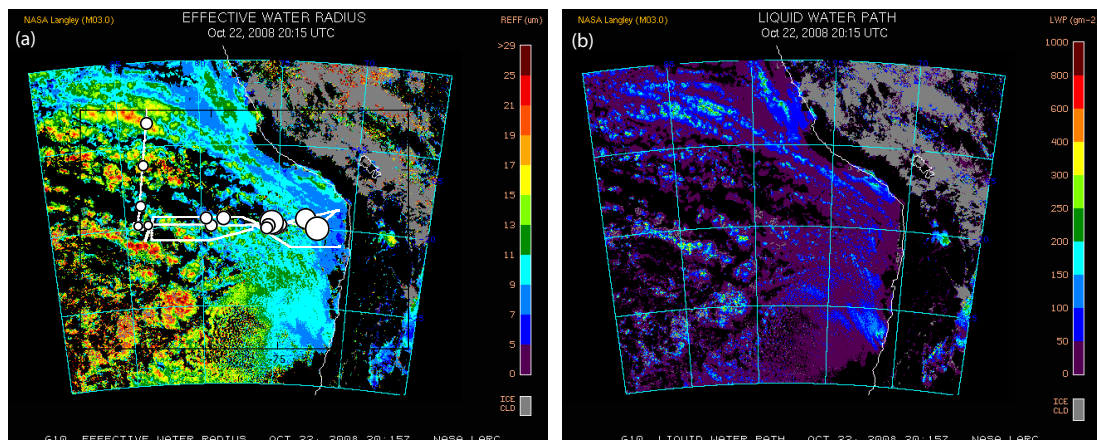
Figure 4.2: Images from the GOES-10 satellite showing (a) effective water radius (μm) and (b) liquid water path (g m^{-2} for 22 October 2008. The ship track and average location of filter samples are overlaid on the map of effective water radius to illustrate the qualitative relationship between CCN concentration (marker size) and droplet radius since droplet number concentrations are not available at this time [http : //catalog.eol.ucar.edu/cgi − bin/ vocals/imagewrap.nonav?file_url = /vocals/ops/goes − 10].

4.4   Discussion

At the smallest observed mean diameter (120 nm), including the organic fraction as completely insoluble lowers the predicted CCN by over 10% relative to a completely soluble particle. The fraction of soluble inorganic mass in the second case was approximately 50% and ranged from 41% to 67%; this is a large change in composition between Cases 1 and 2 and is the main cause of the observed change in activated fraction between the two cases. The effect of chemical composition among the three cases is most notable for particles below 160 nm. Because the mean diameter is below 160 nm only for particles less than 600 km away from the continent, the effect of chemistry is also most notable in the samples collected near shore (Fig. 4.1). Farther from shore, the particles are larger due to increased time for cloud processing and condensation of semi-volatile compounds. Above approximately 160 nm, treating the oxidized organic groups as soluble organic compounds does not produce a significant difference in predicted CCN concen-
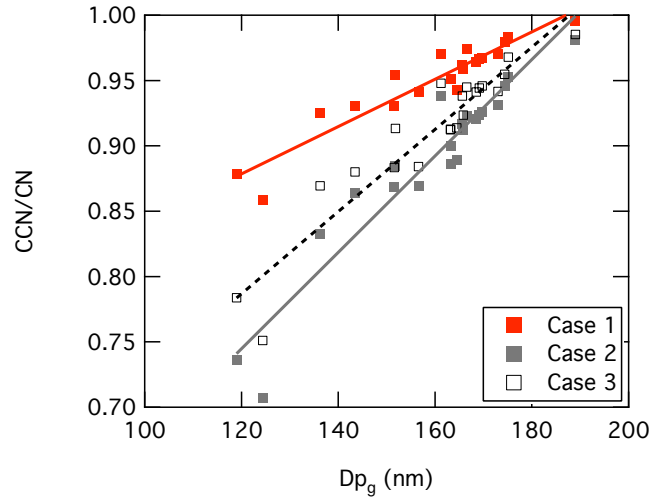
Figure 4.3: Predicted activated fraction (CCN/CN) compared with geometric mean diameter (Dpg) for all three cases.

tration. For all samples, including soluble organics lowers the predicted CCN at least a few percent though this is likely to be within the uncertainty associated with ambient organic surface tension and molecular weight. Accounting for these effects is beyond the scope of the current study but the expected result would be added variability in the predicted CCN concentration, especially close the continent where organic mass concentrations are higher. Above 55% soluble material, there is no observable change in activated fraction with increasing soluble fraction indicating a threshold for chemical influence on CCN applies to all three cases. The assumption of complete internal mixing among sulfate, dust, and organic components applied here is meant as a simplification to explore the potential role of organic components in controlling CCN activity in this region. However, chemical analyses showed that organic components were more strongly associated with dust than with sulfate. To determine what role the mixed organic and dust particles play in changing cloud drop number concentrations near the coast, a series of comparisons of predicted versus measured CCN concentration would be needed. Predicted CCN concentrations would need to account for separate particles composed of sulfate and organic components. Measured CCN concentrations, which are currently unavailable, would provide a necessary constraint on the modeled concentrations.

The Geostationary Operational Environmental Satellite (GOES-10) satellite shows effective cloud drop radius (R_{eff}) and liquid water path (LWP, Fig. 4.2) for 22 October 2008, approximately half-way into the VOCALS-REx sampling period. We have overlaid the ship track, average filter location, and predicted CCN from Case 3 as a guide for the eye. Consistent with predicted CCN concentrations and the Twomey effect (Twomey, 1977), drops are smaller (approx. 10 μm) near the coast, where CCN concentrations are highest. At the farthest sampling site (-85ºW), effective cloud drop radii are approximately 20 μm. Drop number concentrations are not directly available but the observed constant value for LWP (with increasing distance from the continent) can be used to infer an increase in cloud droplet number accompanying the decrease in droplet radius.

4.5   Conclusion

Predicted CCN concentrations in the southeast Pacific were found to be sensitive to organic composition and solubility for particles below 160 nm diameter. This is relevant in the region within 600 km of Peru and Chile where particle concentrations are highest and particles are smaller due to limited time for atmospheric processing, indicating that future changes in anthropogenic outflow may be important for coastal cloud optical properties. In these conditions, the number of predicted CCN dropped by as much as 10% when a more constrained solubility was assigned to the organic functional groups. Observations by the GOES-10 satellite of cloud drop effective radius and liquid water path are consistent with the geographic distribution predicted here from chemical and physical measurements of submicron aerosol particles. These results are specific to the supersaturations, particle size, number, and chemistry of the southeast Pacific MBL.

4.6   Acknowledgments

This work was completed by the dissertation using particle size distribution measurements collected by D. Coffman, P. K. Quinn, D. S. Covert, and T. S. Bates

and a model of modified Köhler theory developed by Greg Roberts.

References

Albrecht, B. A., 1989. Aerosols, cloud microphysics, and fractional cloudiness. Science 245 (4923), 1227.

Bates, T. S., Quinn, P. K., Coffman, D., Schulz, K., Covert, D. S., Johnson, J. E., Williams, E. J., Lerner, B. M., Angevine, W. M., Tucker, S. C., et al., 2008. Boundary layer aerosol chemistry during TexAQS/GoMACCS 2006: Insights into aerosol sources and transformation processes. J. Geophys. Res. 113.

Chan, M. N., Kreidenweis, S. M., Chan, C. K., 2008. Measurements of the hygroscopic and deliquescence properties of organic compounds of different solubilities in water and their relationship with cloud condensation nuclei activities. Environ. Sci. Technol 42 (10), 3602–3608.

Dusek, U., Frank, G. P., Hildebrandt, L., Curtius, J., Schneider, J., Walter, S., Chand, D., Drewnick, F., Hings, S., Jung, D., et al., 2006. Size matters more than chemistry for cloud-nucleating ability of aerosol particles. Science 312 (5778), 1375.

Ervens, B., Feingold, G., Kreidenweis, S. M., 2005. Influence of water-soluble organic carbon on cloud drop number concentration. J. Geophys. Res. 110.

Gilardoni, S., Russell, L. M., Sorooshian, A., Flagan, R. C., Seinfeld, J. H., Bates, T. S., Quinn, P. K., Allan, J. D., Williams, B., Goldstein, A. H., et al., 2007. Regional variation of organic functional groups in aerosol particles on four US east coast platforms during the International Consortium for Atmospheric Research on Transport and Transformation 2004 campaign. J. Geophys. Res. 112.

Hawkins, L. N., Russell, L. M., Covert, D. S., Quinn, P. K., Bates, T. S., 2010. Carboxylic Acids, Sulfates, and Organosulfates in Processed Continental Organic Aerosol over the Southeast Pacific Ocean during VOCALS-REx 2008. Journal of Geophysical Research in press., doi:10.1029/2009JD013276.

Hawkins, L. N., Russell, L. M., Twohy, C. H., Anderson, J. R., 2008. Uniform particle-droplet partitioning of 18 organic and elemental components measured in and below DYCOMS-II stratocumulus clouds. Journal of Geophysical Research–Atmospheres 113, doi:10.1029/2007JD009150.

Hoppel, W. A., Frick, G. M., Fitzgerald, J. W., Larson, R. E., 1994. Marine boundary layer measurements of new particle formation and the effects non-precipitating clouds have on aerosol size distribution. Journal of Geophysical Research 99, 14.

Jayne, J. T., Leard, D. C., Zhang, X., Davidovits, P., Smith, K. A., Kolb, C. E., Worsnop, D. R., 2000. Development of an aerosol mass spectrometer for size and composition analysis of submicron particles. Aerosol Sci. Technol. 33 (1), 49–70.

Jimenez, J. L., Jayne, J. T., Shi, Q., Kolb, C. E., Worsnop, D. R., Yourshaw, I., Seinfeld, J. H., Flagan, R. C., Zhang, X., Smith, K. A., et al., 2003. Ambient aerosol sampling using the aerodyne aerosol mass spectrometer. J. Geophys. Res. 108 (D7), 8425.

Köhler, H., 1936. The nucleus in and the growth of hygroscopic droplets. Transactions of the Faraday Society 32, 1152–1161.

Maria, S. F., Russell, L. M., 2005. Organic and inorganic aerosol below-cloud scavenging by suburban New Jersey precipitation. Environmental Science &Technology 39 (13), 4793–4800.

Maria, S. F., Russell, L. M., Turpin, B. J., Porcja, R. J., 2002. FTIR measurements of functional groups and organic mass in aerosol samples over the Caribbean. Atmos. Environ. 36 (33), 5185–5196.

Maria, S. F., Russell, L. M., Turpin, B. J., Porcja, R. J., Campos, T. L., Weber, R. J., Huebert, B. J., 2003. Source signatures of carbon monoxide and organic functional groups in Asian Pacific Regional Aerosol Characterization Experiment (ACE-Asia) submicron aerosol types. J. Geophys. Res. 108, 8637.

Martin, G. M., Johnson, D. W., Spice, A., 1994. The measurement and parameterization of effective radius of droplets in warm stratocumulus clouds. Journal of the Atmospheric Sciences 51 (13), 1823–1842.

Nenes, A., Charlson, R. J., Facchini, M. C., Kulmala, M., Laaksonen, A., Seinfeld, J. H., 2002. Can chemical effects on cloud droplet number rival the first indirect effect? Geophysical Research Letters 29 (17), 29–1.

O'Dowd, C. D., de Leeuw, G., 2007. Marine aerosol production: a review of the current knowledge. Philosophical Transactions A 365 (1856), 1753.

Quinn, P. K., Bates, T. S., Coffman, D. J., Covert, D. S., 2008. Influence of particle size and chemistry on the cloud nucleating properties of aerosols. Atmospheric Chemistry and Physics 8, 1029–1042.

Roberts, G. C., Artaxo, P., Zhou, J., Swietlicki, E., Andreae, M. O., 2002. Sensitivity of CCN spectra on chemical and physical properties of aerosol: A case study from the Amazon Basin. Journal of Geophysical Research 107 (D20), 8070.

Russell, L. M., Takahama, S., Liu, S., Hawkins, L. N., Covert, D. S., Quinn, P. K., Bates, T. S., 2009. Oxygenated fraction and mass of organic aerosol from direct emission and atmospheric processing measured on the R/V Ronald Brown during TEXAQS/GoMACCS 2006. J. Geophys. Res. 114 (null).

Seinfeld, J., Pandis, S., 1998. Atmospheric chemistry and physics: from air pollution to climate change. Wiley-Interscience.

Tomlinson, J. M., Li, R., Collins, D. R., 2007. Physical and chemical properties of the aerosol within the southeastern Pacific marine boundary layer. Journal of Geophysical Research 112 (D12), D12211.

Twomey, S., 1977. The influence of pollution on the shortwave albedo of clouds. Journal of the atmospheric sciences 34 (7), 1149–1152.

Chapter 5

Polysaccharides, Proteins, and Phytoplankton Fragments: Four Chemically Distinct Types of Marine Primary Organic Aerosol Classified by Single Particle Spectromicroscopy

Abstract. Carbon-containing aerosol particles collected in the Arctic and southeastern Pacific marine boundary layers show distinct chemical signatures of proteins, calcareous phytoplankton, and two types of polysaccharides in Near-Edge Absorption X-ray Fine Structure (NEXAFS) spectromicroscopy. Arctic samples contained mostly supermicron sea salt cuboids with a polysaccharide-like organic coating. Southeastern Pacific samples contained both continental and ma-

rine aerosol types; of the 28 analyzed marine particles, 19 were characterized by sharp alkane and inorganic carbonate peaks in NEXAFS spectra and are identified as fragments of calcareous phytoplankton. Submicron spherical particles with spectral similarities to carbohydrate-like marine sediments were also observed in Pacific samples. In both regions, supermicron amide and alkane-containing particles resembling marine proteinaceous material were observed. These four chemical types provide a framework that incorporates several independent reports of previous marine aerosol observations, showing the diversity of the composition and morphology of ocean-derived primary particles.

5.1   Introduction

The transfer of organic components from the ocean surface to marine aerosol through bubble bursting was shown over 40 years ago (Blanchard, 1964; Hoffman and Duce, 1976; Gagosian et al., 1982). These components, referred to as "marine primary organic aerosol" or marine POA (Kanakidou et al., 2005), have been observed to contribute to organic mass in remote and coastal marine locations (Gagosian et al., 1982; Crahan et al., 2004; Cavalli et al., 2004; Facchini et al., 2008; Russell et al., 2010b). Decreases projected for Arctic sea ice extent in response to climate warming may contribute an additional 40-200 ng m^{-3} of aerosol organic carbon (OC) by 2100 from a combination of increased surface ocean productivity and increased spatial extent of wave action (Ito and Kawamiya, 2010). This change in OC is significant considering background concentrations of less than 1 μg m^{-3} are common in the remote MBL (Murphy et al., 1998; Quinn et al., 1998; Middlebrook et al., 1998; Clarke et al., 2006; Russell et al., 2010b; Hawkins et al., 2010).

The potential for breaking waves to contribute organic mass to aerosol particles increases with the high concentration of surface active organic compounds and micro-organisms, which are enriched in the surface microlayer (SML) relative to the underlying water (Henrichs and Williams, 1985; Kuznetsova and Lee, 2002; Aller et al., 2005). Observed enrichment factors (EFs) are several orders of magnitude for dissolved and particulate organic carbon (OC) and for specific components like bacteria and viruses. The production of sea spray from bubble bursting results in further enrichment of OC (Kuznetsova et al., 2005; Aller et al., 2005; Russell et al., 2010b). EFs for organic components in marine aerosol particles have been reported from 5 (viruses and bacteria) to over 100 (organic carbon) from the SML (Aller et al., 2005; Russell et al., 2010b). Since the SML is the source of marine POA, the types and relative contributions of organic compounds are expected to be similar. Chemical characterization of the SML has revealed that carbohydrates constitute 80% of TOC (Aluwihare et al., 1997), although lipid and protein components have also been observed (Larsson et al., 1974; Aller et al., 2005). Investigations of the composition of airborne marine organic particles have shown multiple lines of evidence for carbohydrates (Crahan et al., 2004; Leck and

Bigg, 2005a,b; Kuznetsova et al., 2005; Leck and Bigg, 2008; Facchini et al., 2008; Russell et al., 2010b), amino acids (Leck and Bigg, 1999; Kuznetsova et al., 2005) and marine micro-organisms (Leck and Bigg, 2005a; Aller et al., 2005), confirming that many of the organic components found in the SML are transferred to the marine atmosphere. One important question that remains is how these marine organic components are mixed in airborne particles.

To better characterize marine POA in the remote marine boundary layer, aerosol particles were collected during research cruises in the Arctic and southeastern Pacific oceans in local springtime. Single particle x-ray spectromicroscopy was used to separate individual particles into four distinct types of marine POA using organic functional groups, particle morphology, and elemental composition. The findings of this analysis are compared in the context of previous marine POA observations using a variety of analytical techniques.

5.2   Methods

5.2.1   Sample Collection

Ambient aerosol particles for Scanning Transmission X-ray Microscopy with Near-Edge X-ray Absorption Fine Structure (STXM-NEXAFS) analysis were collected in 2008 as part of the International Chemistry Experiment in the Arctic LOwer Troposphere (ICEALOT) and VAMOS Ocean Cloud Atmosphere Land Study Regional Experiment (VOCALS-REx) research cruises, using nearly identical sample collection techniques. The ICEALOT cruise through the North Atlantic and Arctic Oceans was conducted in March and April 2008 on the UNOLS R/V *Knorr* to investigate the composition and sources of atmospheric aerosol and gas phase species to the northern polar region. Detailed descriptions of the ICEALOT cruise track, sampled air mass histories, and related aerosol measurements are described in Russell et al. (2010b). All ICEALOT single particles presented here were collected north of 63°N; most particles were collected within the Arctic Circle (north of 66.56°N). In October and November 2008, the NOAA R/V *Ronald Brown* traveled in the southeastern Pacific Ocean in the region along

20°S as part of VOCALS-REx, a multi-platform campaign designed to investigate ocean-atmosphere interface processes and to probe aerosol-cloud interactions in the stratocumulus-topped MBL (Wood et al., 2006). Details of the VOCALS-REx cruise track, sampled air mass histories, and aerosol chemistry are described in Hawkins et al. (2010). For simplicity, all ICEALOT particles will be referred to as "Arctic" and all VOCALS-REx particles will be referred to as "Pacific."

Particles were collected through a shared, isokinetic sampling inlet 18 m above sea level (Bates et al., 2008) and impacted onto silicon nitride windows (Si_3N_4, Silson, Ltd., Northampton, England) using a rotating impactor (Streaker, PIXE Internationl Corp., Tallahassee, FL) located in a humidity-controlled enclosure. The relative humidity was below 30% during ICEALOT and was controlled at 55% during VOCALS-REx. Windows were sealed and stored frozen until analysis.

5.2.2 Analysis

STXM-NEXAFS

Particles were analyzed on Beamline 5.3.2 at the Advanced Light Source in Lawrence Berkeley National Laboratory (Berkeley, CA) at atmospheric temperature and under dry He (1 atm). Details of STXM-NEXAFS analysis of atmospheric aerosol particles are described in Takahama et al. (2007) and Takahama et al. (2010), and a brief description is provided here. Image scans from 278 to 320 eV (with up to 0.2 eV resolution) of individual particles provide X-ray absorption spectra of the carbon K-edge, with characteristic peaks from various energy transitions of the bound carbon atoms. Organic and inorganic carbon-containing functional groups are identified by their specific absorption energy between 280 and 320 eV (Table 5.1). Potassium L-edge transitions also occur in this region. Only particles with measurable difference in absorbance between 280 and 292 eV (the carbon edge) are selected for image scans. Absorption spectra from each pixel within the two-dimensional particle image are averaged and normalized following the procedure described in Takahama et al. (2010). An automated algorithm for peak fitting (Takahama et al., 2010) provides relative absorption of aromatic/alkene R(C=C)R', ketone R(C=O)R', alkyl R(C-H)$_n$R', carboxylic carbonyl

R(C=O)OH, alcohol R-COH, and carbonate CO_3^{2-} carbon. Spherical-equivalent geometric diameter is used to approximate particle size and is equal to the diameter of a sphere having the same area as the sum of individual pixels with signal above the background level.

SEM-EDX

A subset of analyzed carbon-containing single particles (11 particles) were investigated for elemental composition using Scanning Electron Microscopy with Energy Dispersive X-rays (SEM-EDX) at the Scripps Institution of Oceanography Analytical Facility (La Jolla, CA) using a model FEI Quanta 600 microscope at 10 keV. Samples were uncoated and were analyzed under vacuum. All samples showed Si and N absorption due to the sample substrate. Identified elements include C, O, Ca, S, Na, Mg, and Cl.

5.3   Results and Discussion

Figure 5.1 shows the distribution of analyzed carbonaceous particles in Pacific and Arctic samples categorized by particle-average spectra. Non-marine particle types include soil dust, combustion, and secondary particles. These particle types have been observed in previous measurements in urban locations (e.g. Mexico City) and areas affected by urban outflow (e.g. offshore China, the Carribbean and the Pacific Northwest) (Takahama et al., 2007). Soil dust particles are characterized by carbonate, potassium and carboxylic acid-containing organic components (Type "f" in Takahama et al. (2007)) and are attributed to air masses passing near Santiago and other urban areas along the arid Chilean coast before reaching the ship (Hawkins et al., 2010)

Combustion particles show strong aromatic/alkene absorbance at 285 eV and broad alkyl carbon absorption at 292 eV (similar to Type "d" in Takahama et al. (2007)). With one exception, these particles were submicron, and four out of eight particles were below 300 nm spherical equivalent diameter. Secondary type particles are characterized by broad carbon absorption beyond 300 eV and

by carboxylic carbonyl absorption at 288.7 eV. These particles (Type "a" in Taka-hama et al. (2007)) typically have noisier spectra than purely organic particles. In previous studies in marine locations, these particles have been the most commonly observed type (Takahama et al., 2007). In Pacific samples, however, much of the carboxylic acid-containing organic mass is associated with soil dust particles, consistent with measurements reported in Sullivan and Prather (2007) of internal mixtures of oxalic and malonic acids with mineral dust.

All organic particles not included in the soil dust, combustion, or secondary particle types were identified as marine origin and fell into four types: carboxylic acid-containing polysaccharides (Arctic), low-solubility polysaccharides (Pacific), calcareous phytoplankton fragments (Pacific), and proteinaceous material (Arctic and Pacific) (Table 5.2). Marine particles were observed in both Pacific and Arctic samples; however, most of the particles collected in the Arctic region were supermicron. The features and interpretation of the NEXAFS spectra and STXM morphology of particles in each marine type are discussed in detail in the following sections. In addition, three Pacific particles were identified with carbonate and potassium absorption but without any signatures of organic carbon. Their spectra are very similar to type "E" particles found in ocean sediments in Brandes et al. (2004), which were identified as marine calcium carbonate. These particles are labeled "$CaCO_3$" in Figure 5.1 but are not included below since they lack organic components.

5.3.1 Carboxylic acid-containing polysaccharides on sea salt

Figure 5.2a shows single particle spectra (and category average) for the most commonly observed marine particle type. Spectra in this category have strong carboxylic carbonyl peaks and weak alcohol, carbonate, and potassium peaks. These particles were seen in Arctic samples and compose 43 of the 48 analyzed Arctic particles. Two particles collected at a coastal site in California, which is frequently influenced by marine air masses, also share these features (Liu et al., 2010). Filter measurements of submicron particles from the Arctic show a large contribution from alcohol (C-OH) groups to OM attributed to marine carbohydrate-like com-

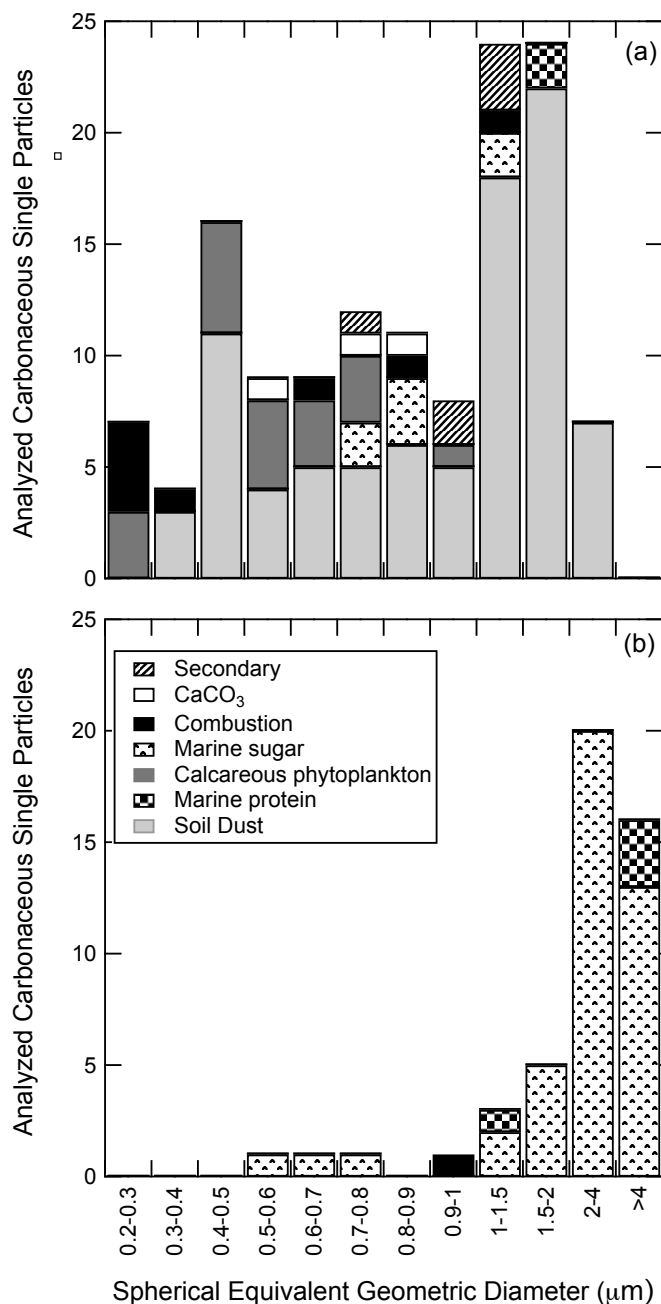Figure 5.1: Distribution of analyzed particles from (a) southeastern Pacific and (b) Arctic marine boundary layers. Particles labeled as "marine sugars" in Arctic samples correspond to Figure 5.2a (PsI) while those in southeastern Pacific samples correspond to Fig. 5.2b (PsII). Particle distribution for Arctic samples is a result of the shattered sampling windows and does not represent the observed particle size distribution.

pounds (Russell et al., 2010b), consistent with previous chemical characterization of the surface microlayer as 80% carbohydrate (Aluwihare et al., 1997) and with exopolymer secretions (EPS) repeatedly identified in submicron marine aerosol (Leck and Bigg, 2005a,b; Facchini et al., 2008; Leck and Bigg, 2008). Just under 90% of the observed Arctic supermicron particles do not show a significant peak at 289.5 eV (C-OH transition), which is different from most of the reported carbohydrate reference spectra (Solomon et al., 2009). A fraction of these observed spectra do have a shoulder located near 289.5 eV yet all spectra are dominated by a large peak near 288.7 eV (carboxylic carbonyl). Relative NEXAFS absorption of carboxylic carbonyl and alcohol groups can vary by 50% in acid-group-containing polysaccharides; for example, muramic acid and alginic acid show stronger carboxylic carbonyl (π^* transition) peaks than alcohol (σ^* transition) peaks (Solomon et al., 2009) despite the fact that the molar ratio of carboxylic acid to alcohol groups is 0.33 in muramic acid and 0.5 in alginic acid. These compounds are found in bacterial (muramic) and brown algae (alginic) cell walls as structural polysaccharides.

Alginic acid is relevant for marine POA since the brown algae family comprises giant kelp and seaweed found in cold, northern hemisphere oceans (Van Den Hoek, 1982). Figure 5.3 shows the similarities between the average spectrum of particles in this category and an alginic acid reference spectrum (Lawrence et al., 2003). Both spectra show a strong, narrow peak at 288.7 eV and a weaker, broad absorption at 293 eV, without any other organic carbon peaks. Carbonate and potassium absorbances in the average carboxylic acid-type spectrum can be attributed to the sea salt associated with these particles. In fact, many of the particles in this type were characterized by large fractions of inorganic cuboid structures with an uneven, organic coating (Fig. 5.4a). This small amount of organic relative to crystallized sea salt is consistent with the lower organic enrichment expected for supermicron particles relative to submicron particles. This morphology suggests that the organic components on these particles are more soluble than previously reported polysaccharides, which are generally colloidal spherules not associated with sea salt. The association with seawater components is also consistent with the assignment of these particles as carboxylic acid-containing polysaccharides like
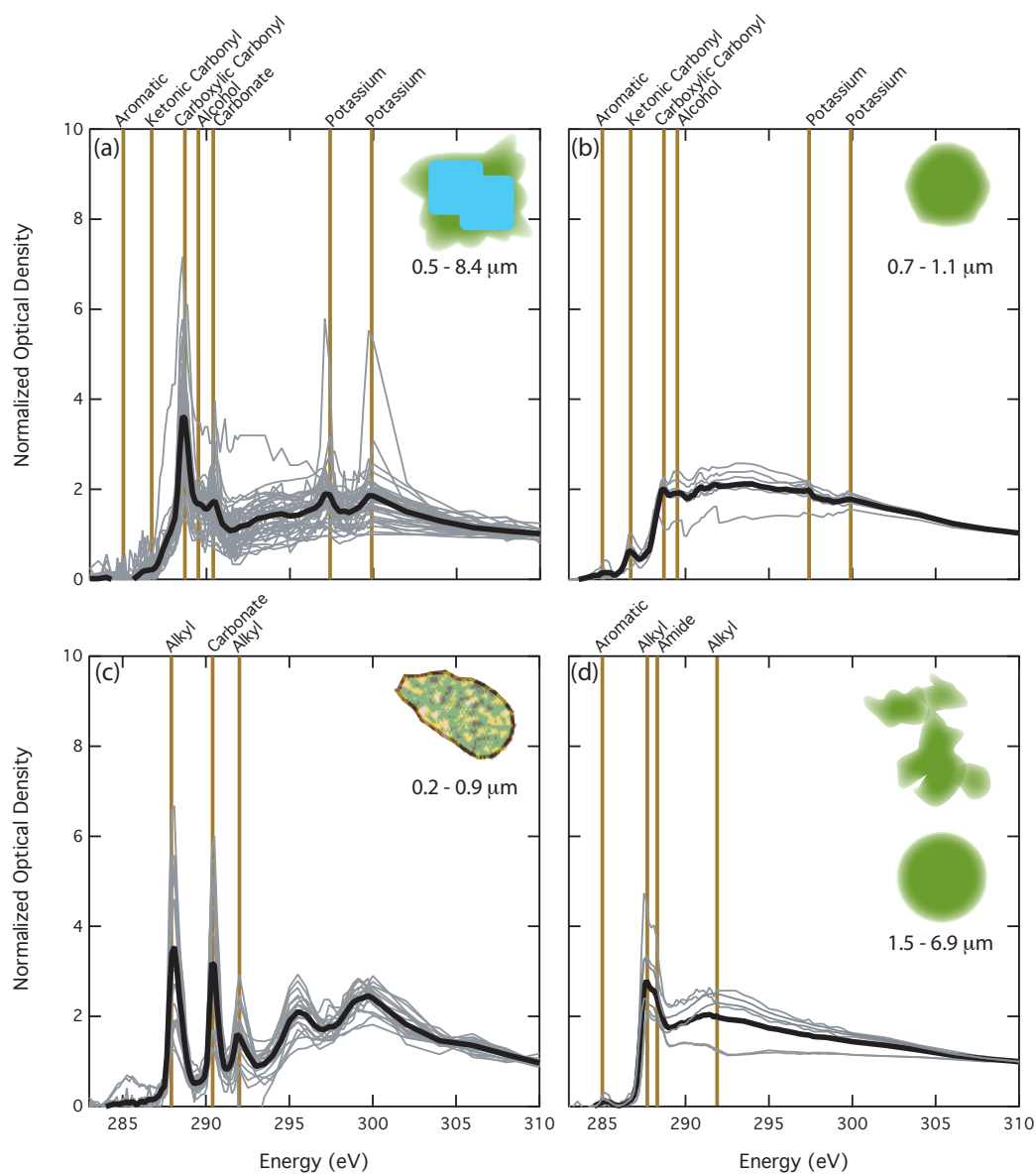
Figure 5.2: Individual (grey) and average (black) NEXAFS spectra of the four marine particle types including (a) PsI, (b) PsII, (c) calcareous phytoplankton fragments, and (d) proteinaceous particles. Illustrations in each panel represent commonly observed morphologies associated with each spectra type. The observed size range for each type is shown below the illustrations.

alginic acid, since it has a strong tendency to take up water. These particles are referred to as "Type I polysaccharides" or PsI.

5.3.2   Low-solubility polysaccharides

Figure 5.2b shows single particle spectra (and category average) for particles with visible alcohol C-OH absorption (289.5 eV) accompanied by aromatic, ketonic, and carboxylic carbonyl carbon peaks found only in Pacific samples. Here the carboxylic carbonyl absorption is approximately equal to the alcohol carbon absorption, indicating that these compounds have more than two or three alcohol C-OH groups per carboxylic C(=O)OH group. Reference polysaccharides with equivalent peak heights at or near 288.7 (carboxylic carbonyl) and 289.5 eV (alcohol) include chitin and L-rhamnose (Solomon et al., 2009). Chitin does not contain any carboxylic carbonyl groups but does contain amide carbonyl groups (monomers are N-acetylglucosamine) which may be responsible for the peak at 288.4 eV. Glucosamine is also present in a 1:1 ratio with muramic acid monomers in peptidoglycan, which has been shown to be a major constituent of marine dissolved organic matter (DOM) (Benner and Kaiser, 2003). Therefore, the observed peak in the average alcohol-type spectrum near 288.7 eV could be attributed to either carbonyl in amide groups or to a mixture with carboxylic carbonyl-containing polysaccharides. It is more probable that these particles contain a mixture of structural polysaccharides than isolated compounds, resulting in less pronounced spectral features than the reference spectra. In fact, the most similar spectrum to the category average comes from a sediment sample of marine particulate organic matter (POM, Brandes et al. (2004)) (Fig. 5.3). Brandes et al. (2004) used factor analysis to separate different biological compounds in marine POM, and one factor with significant C-OH absorption was identified as carbohydrate material. The carbohydrate-containing marine POM shares the aromatic and ketonic carbon absorbances with the spectra of these particles, while reference (pure) structural polysaccharide spectra in Solomon et al. (2009) do not. Particles of this type are referred to as "Type II polysaccharides" or PsII.

Filter-based FTIR spectroscopic measurements of Pacific submicron parti-
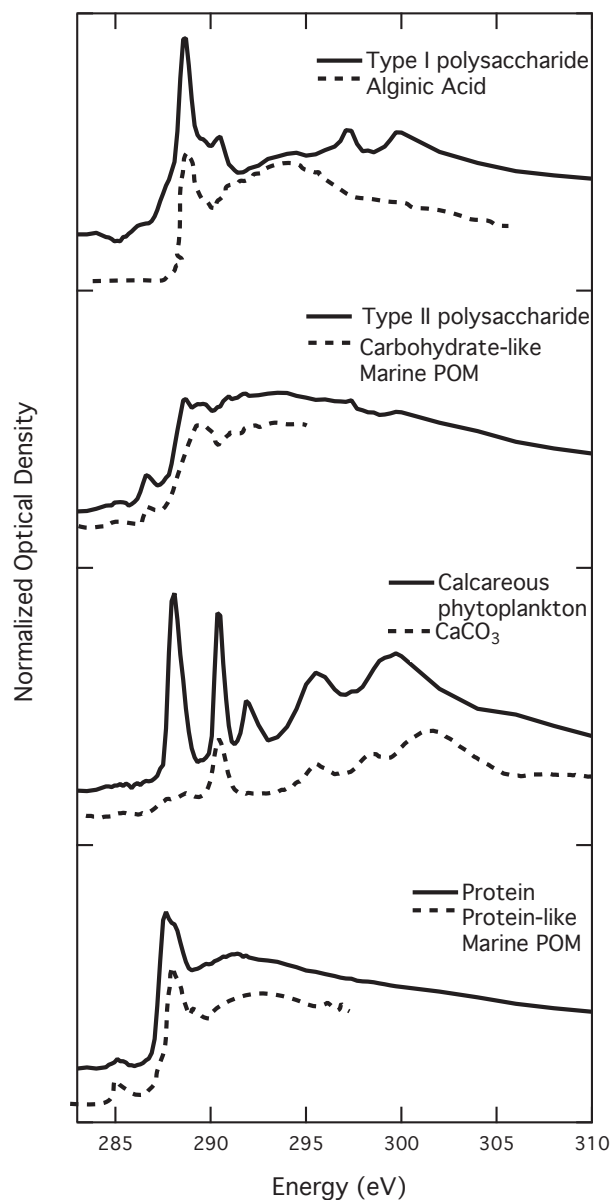
Figure 5.3: Normalized average spectra for each of the four marine particle types and corresponding reference spectra with similar features. Spectra were reproduced from Lawrence et al. (2003) (alginic acid), Brandes et al. (2004) (carbohydrate and protein-like marine POM), and http://xray1.physics.sunysb.edu/ micros/xas/xas.html, unpublished ($CaCO_3$).
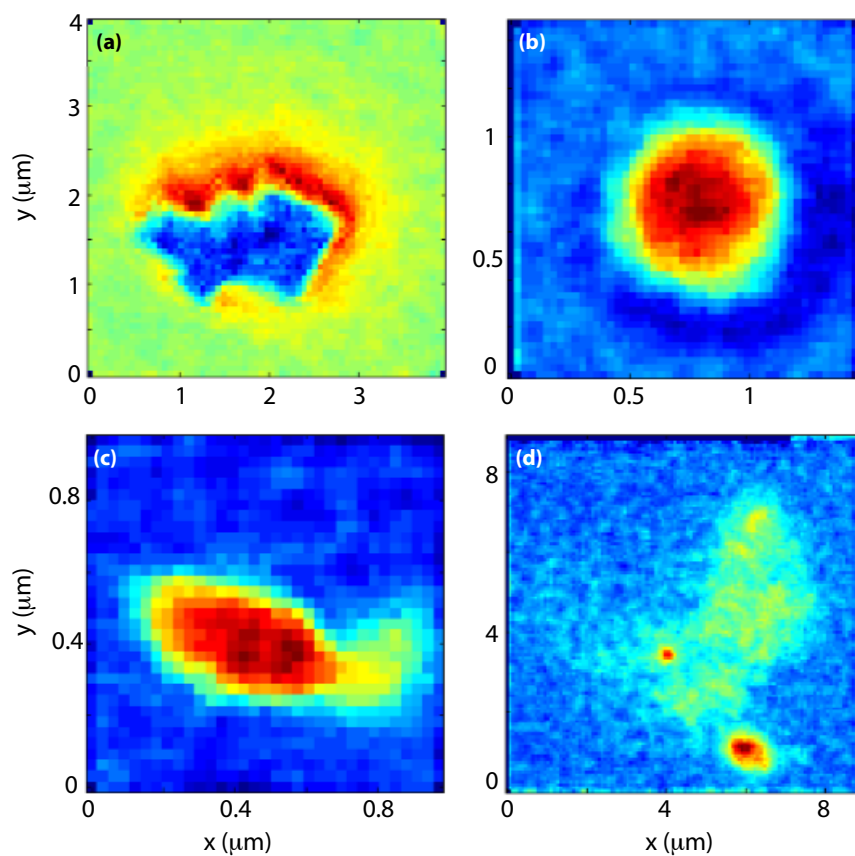
Figure 5.4: Relative carbon images of representative particles for (a) PsI, (b) PsII, (c) calcareous phytoplankton, and (d) proteinaceous particle types. For each image, the red-blue color scale is relative to individual particle carbon absorption.

cles show a significant contribution from marine OM (from factor analysis) that is most prominent in sampled air masses with low PM_1 particle mass (< 1 μg m^{-3}) and with low radon concentration (< 200 mBq m^{-3}), indicating little continental influence (Hawkins et al., 2010). Complementary ion chromatography (IC) measurements show low concentrations of submicron Na$^+$ (< 0.1 μg m^{-3}) or Cl$^-$ ($<$ 0.07 μg m^{-3}), which is consistent with the relatively calm seas encountered during the cruise. PsII particles are spherical, with no cuboidal inorganic core (Fig. 5.4b), similar to the spherical colloidal structures observed in TEM by Leck and Bigg (2005b). The lack of cuboids is consistent with the lower fraction of Na/OM expected in submicron particles.

5.3.3 Calcareous phytoplankton fragments

Figure 5.2c shows single particle spectra (and category average) for particles with three strong, narrow peaks at 288.1, 290.4, and 292 eV associated with alkyl R(C-H)$_n$R' (π*), inorganic carbonate CO$_3^{2-}$ (π*), and alkyl R(C-H)$_n$R' (σ*) transitions, respectively. These particles were strictly submicron and found in Pacific samples. A particle with this same characteristic signal was also found in a sample collected at a California coastal site (Liu et al., 2010). Compared with all other particle-average spectra, these spectra have much stronger signal-to-noise and have little particle-to-particle variability. These particles also have very little pre-edge absorbance indicating that they are entirely composed of the absorbing (carbonaceous) material, consistent with their strong signal. The narrow alkyl peaks indicate little variation in the neighbors of the absorbing alkyl carbon atoms (e.g. straight-chain alkane compounds) as does the absence of other organic carbon peaks.

The carbonate peak at 290.4 eV is also strong and narrow, indicating that other than the long-chain hydrocarbon compounds, the particle is mostly some form of carbonate. The reference spectrum for $CaCO_3$ is shown in Figure 5.3. $CaCO_3$ shares the sharp peak at 290.4 eV and the multiple, broad peaks to the right of 295 eV with the average spectrum. To determine the type of carbonate-based mineral, 6 of the 19 particles in this category were analyzed with SEM-

EDX; all particles showed strong C, O, and Ca signals while S, Na, Mg, and Cl were absent or weak(Fig. 5.5c). These particles show a variety of non-spherical shapes. Some particles appear elliptical with sharp points (Fig. 5.4c) and others are amorphous. Based on their appearance, the particles resemble small, dust-like fragments. However, their chemical composition is not consistent with aged or processed dust transported to the remote MBL. In addition, long-chain hydrocarbons are not typical of secondary organic aerosol (Zhang et al., 2007); the absence of S in EDX spectra also makes it unlikely that atmospheric processing is responsible for the majority of organic mass in these particles.

Previous observations of excess Ca^{2+}, relative to sea salt ratios, in marine aerosol have been attributed to fragments of calcium carbonate-producing phytoplankton (coccolithophores) emitted to the atmosphere during bubble bursting (Sievering et al., 2004). These single-celled phytoplankton produce delicate, calcium carbonate scales (coccoliths) that continually slough off the organisms during their growth and that are released during predation (Godoi et al., 2009). These scales are oval-shaped and are typically 500-3000 nm in length, resulting in fragments that are consistent with the observed size range of these alkane/carbonate particles. Coccolithophores (especially Emiliania huxleyi) are abundant in both high and low latitude oceans and are responsible for about half of the total oceanic carbonate production (Beaufort et al., 2008). Their blooms are so large and persistent that they can been seen from space in satellite images of ocean color as patches of light green against the dark blue ocean. A recent study measuring whole coccolithophores, detached scales, and calcite fragments in surface waters in the same region as the VOCALS-REx cruise has documented their abundance in the Peru-Chile Upwelling (PCU) and the South Pacific Gyre (SPG) (Beaufort et al., 2008). The measured seawater carbonate particle surface area distribution in their work showed a large peak between 2 and 3 μm (corresponding to whole coccoliths with diameters between 1.6 and 2 μm) and a smaller peak at 250 nm (corresponding to coccolith fragments with diameters around 560 nm). This smaller mode is consistent with the size range of observed particles in this category.

In addition to producing a large fraction of oceanic carbonate, coccol-

ithophores are known to produce extremely stable, lipid-like compounds called alkenones (nC$_{37}$-C$_{39}$), which contain one ketone group and two or three degrees of unsaturation (Jordan and Kleijne, 1994). Although the exact function of these compounds is unknown, an investigation of alkenones in various organelles and membranes of Emiliania huxleyi has shown that they are predominantly located in the coccolith-producing compartment (CPC) of the cell and are most likely membrane-unbound lipids associated with the function of the CPC (Sawada and Shiraiwa, 2004). The co-production of these long-chain alkanes with calcite coccoliths is consistent with the strong, sharp alkyl peaks present in our alkane/carbonate particle spectra and with the absence of other groups, such as carboxylic acids. Co-production would also result in a similar ratio of the two species (alkane and carbonate) over the particle, rather than separate carbonate and alkane-dominated regions. Figure 5.5b shows the pixel-by-pixel normalized alkane absorption compared with normalized carbonate absorption for each of the 19 alkane/carbonate-type particles. Correlations between these two groups are strong (12 of the 19 particles have r > 0.75). These strong correlations demonstrate the uniformity of the two groups over individual particles, though the relative amounts of alkane and carbonate groups (i.e. the fitted slopes) vary among particles. Given these observations, the alkane/carbonate particles will be referred to as "Calcareous phytoplankton fragments" in the remaining sections.

5.3.4   Proteinaceous particles

Figure 5.2d shows single particle spectra (and category average) for particles with aromatic/alkene, alkyl, and amide carbon absorptions at 285, 287.7, and 288.2 eV, respectively. The aromatic/alkene peak at 285 eV has a shoulder at 285.4 eV in all 6 particles indicating the presence of multiple unsaturated carbon environments. These spectra, like the calcareous phytoplankton spectra, have low noise and are quite similar to one another in terms of peak locations, shapes, and relative peak heights. Unlike the other categories, particles with this signature are found in both Arctic and Pacific samples but with slightly different morphologies. The two Pacific particles are spherical and all four of the Arctic particles are loose agglomerations
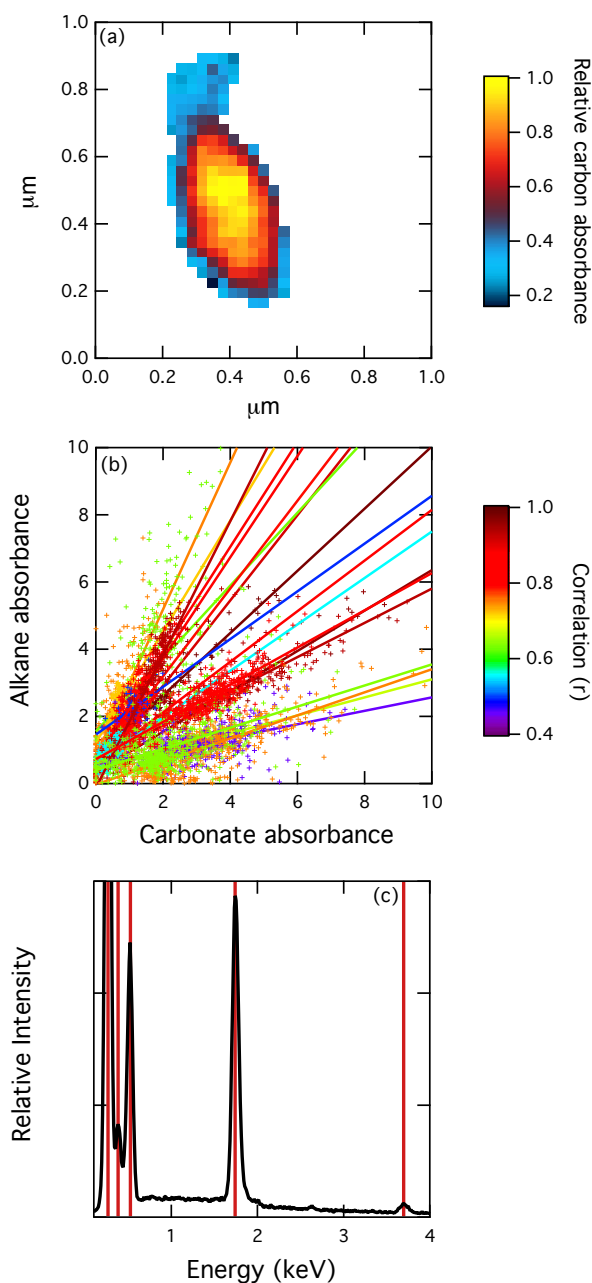
Figure 5.5: (a) Relative carbon absorbance per pixel from integrated NEXAFS particle-average spectrum for a calcareous phytoplankton fragments. (b) Alkane absorbance compared with carbonate absorbance for pixel-by-pixel fit of NEXAFS spectra of all calcareous phytoplankton type particles. Markers are colored by the correlation coefficient for each least-squares linear regression (one color per particle). (c) EDX spectrum of the same particle at 10 keV accelerating voltage. Vertical red lines mark the C, N, O, Si, and Ca absorbances from left to right. N and Si absorbances are from the sample substrate.

of carbonaceous material (Fig. 5.4d). The most unique feature of these spectra is the shoulder at 288.2 eV, corresponding to carbonyl carbon in an amide group (Myneni, 2002; Solomon et al., 2009). Amide groups have also been identified from the CNH σ^* transition at 289.5 eV (Russell et al., 2002; Myneni, 2002). Amide groups (known as peptide bonds when found in proteins) are formed from dehydration reactions of the carboxylic acid group of one amino acid monomer and the amine group of another. Therefore, reference spectra for amino acids that have strong carboxyl carbonyl absorption (Solomon et al., 2009) are not representative of bound amino acid monomers in proteins. The broad alkyl absorption near 292 eV indicates that a variety of alkyl carbon environments exist in these particles, contrasting the sharp peak at 292 eV in the calcareous phytoplankton fragments. In addition, the presence of two alkyl carbon peaks and the absence of the carboxylic carbonyl peak indicate that these proteinaceous compounds may be related to lipoproteins that are found in the membranes of chloroplasts. Lipoproteins contain both lipid and protein components and could be responsible for the significant alkyl absorption seen here. Aromatic and alkene groups are found in proteins as well. Phenylalanine, tyrosine, histidine, and tryptophan are all amino acids with aromatic or alkene side groups.

The fourth pair of spectra in Figure 5.3 show the spectral similarities between the average amide-type particle spectrum and the protein-like component of marine POM identified in Brandes et al. (2004). The two spectra share the small shoulder at 285.4 eV and the amide and broad alkyl absorption regions. However, the amide-type average spectrum has more π^* alkyl absorption (287.7 eV) (which is associated with long-chain hydrocarbons such as lipids) than the protein-like marine POM. The lipid component may give the these particles more surface active properties and may result in preferential concentration in the surface microlayer. If this is the case, lipid-containing proteinaceous material would be preferentially transferred to the atmosphere during bubble bursting over non-lipid proteinaceous compounds. The particle images in this type, both spherical and agglomerative, show little evidence of sea salt, which is consistent with hydrophobic organic material. In collocated filter measurements of both Pacific and Arctic MBL air masses,

primary amines composed 8% of marine OM (from factor analysis). In fact, primary amine groups have been identified in marine OM factors from all ambient measurements where marine factors were identified (Russell et al., 2010a). That the Pacific and Arctic proteinaceous POA spectra are indistinguishable reflects the apparent chemical similarity of the protein components in marine POA.

5.3.5 Reconciling marine POA observations

Over 10 years of measurements of marine POA are summarized in Table 5.3; although the collection encompasses particle properties determined from diverse techniques from TEM-EDX to HNMR, most observations can be assigned to one of three main types: 1) polysaccharides, 2) proteins and amino acids, or 3) micro-organisms and their fragments. Figure 5.6 illustrates the three main types their surface ocean counterparts using the four types of marine POA particles observed in this study. The chemical characterization of single marine POA particles suggests that biogenic organic components and micro-organisms observed in this and previous studies are present as an external mixture including–but not limited to–polysaccharides, proteins, and micro-organisms.

Using TEM images of colloidal spherules, x-ray backscatter of elemental components, and tests for solubility, Leck and Bigg (2005a,b) deduced that the hydrated, heat-resistant, hydrophobic organic substance present in submicron marine aerosol was related to exopolymer secretions (EPS), which are high molecular weight, hydrated polysaccharides. Although the attributes of their measurements of particle shape, size, and solubility were consistent with EPS characteristics, little chemical evidence was available to confirm their composition as polysaccharides. Near the same time, ambient marine particles from the Mediterranean and Atlantic oceans were shown to contain polysaccharide-rich gels using Alcian blue dye, a stain sensitive to all types of polysaccharides (Kuznetsova et al., 2005). EI-MS measurements of marine aerosol in the western Pacific also showed substantial contributions from carbohydrates (i.e. levoglucosan and glucose) partially attributed to organics from the ocean surface (Crahan et al., 2004). A subsequent HNMR study of laboratory generated aerosol (using North Atlantic seawater) cor-

roborated the presence of polysaccharide-like organic components in marine POA by reporting aliphatic and hydroxylated functional groups in addition to lipid-like signatures (Facchini et al., 2008). The authors proposed lipopolysaccharides as a possible explanation for the observed groups. Evidence that polysaccharides accounted for 44-61% of marine submicron OM was provided in Russell et al. (2010b) using FTIR spectroscopy. Their work used the chemical similarity of alcohol C-OH groups in ambient marine submicron aerosol with reference FTIR spectra of 11 different polysaccharides (e.g. pectin, glucose, and xylose). That study was the first to report large quantities of specific signatures of polysaccharides associated with sea salt in submicron ambient marine aerosol, consistent with both the physical attributes reported in Leck and Bigg (2005a) and Leck and Bigg (2008), and the chemical signatures of simulated marine aerosol in Facchini et al. (2008). Using single particle spectromicroscopy, we have observed that polysaccharide-containing particles make up a majority of the measured carbonaceous single particles in two marine regions. From these single particle measurements we have also estimated the mass distribution of Arctic and Pacific marine particles, using the spherical equivalent diameter approximated for each particle and an average density of 1 μg m^{-3} (for simplicity). Figure 5.7 shows the combined, approximate mass distribution of Arctic and Pacific marine POA. Together, Type I and II polysaccharides compose 57% of measured submicron particle mass (and 83% of total particle mass), consistent with the observations of Russell et al. (2010b). We also show that multiple types of polysaccharides, including water-insoluble compounds resembling chitin, exist in airborne marine particles.

Prior to the discovery of polysaccharides in marine aerosol, TEM analysis of Arctic submicron aerosol particles indicated that the spherical, hydrophobic organic particles could be related to amino acids (i.e. L-methionine) based on the surface active nature of the aerosol particles and on measurements of surface active proteins being scavenged by bubbles in seawater (Leck and Bigg, 1999). However, the same properties attributed to proteins in Leck and Bigg (1999) could also be attributed to EPS (Leck and Bigg, 2005a,b, 2008). More recently, Kuznetsova et al. (2005) used Coomassie blue dye to confirm that some of the colloidal gel-
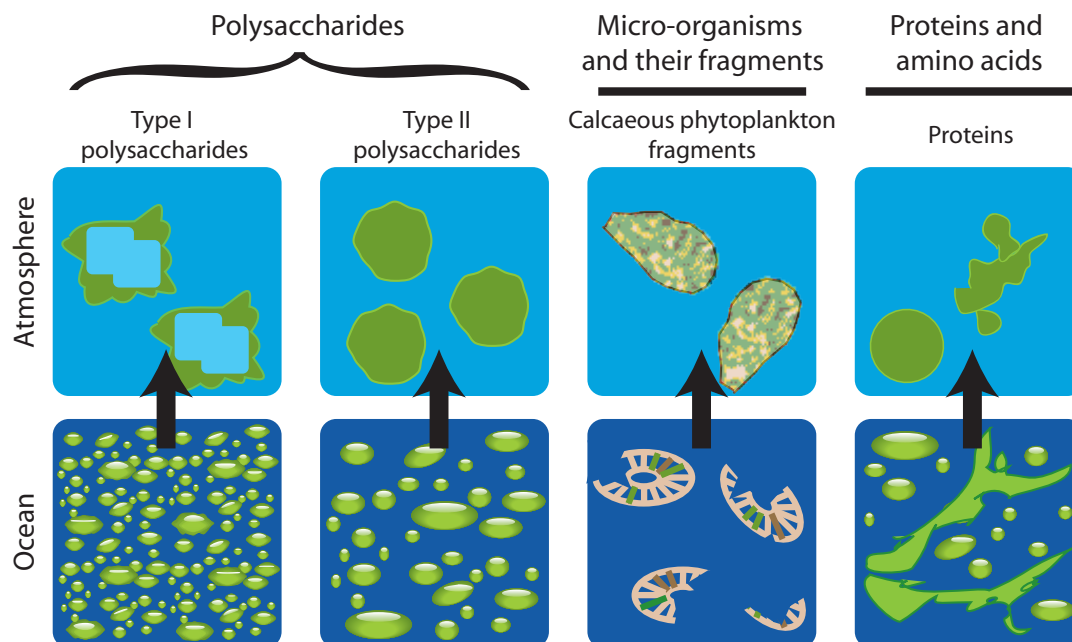
Figure 5.6: Illustration of the four observed marine particle types in the ocean and atmosphere.

like material surrounding bacteria and virus in Mediterranean and Atlantic marine aerosol samples was indeed proteinaceous. Here we report observations of amide-containing hydrophobic marine aerosol particles from two distant ocean environments that match the characteristic spectral signatures of proteinaceous marine POM, indicating that protein-like organic compounds also contribute to marine POA in many parts of the marine atmosphere.

Marine micro-organisms clearly play a large role in marine aerosol formation and composition. In addition to secreting non-volatile organic components (e.g. polysaccharides, lipids, and proteins) and emitting gas phase precursors to marine aerosol (e.g. dimethyl sulfide, DMS), they can themselves be lofted to the atmosphere where they can serve as surfaces for heterogeneous reactions and as cloud condensation nuclei (Blanchard, 1964; Leck and Bigg, 1999, 2005a; Aller et al., 2005). Most observations of airborne micro-organisms have reported bacteria or diatom fragments, mostly because these particles have distinct shapes easily discernible from other particles in TEM images. Submicron fragments, especially
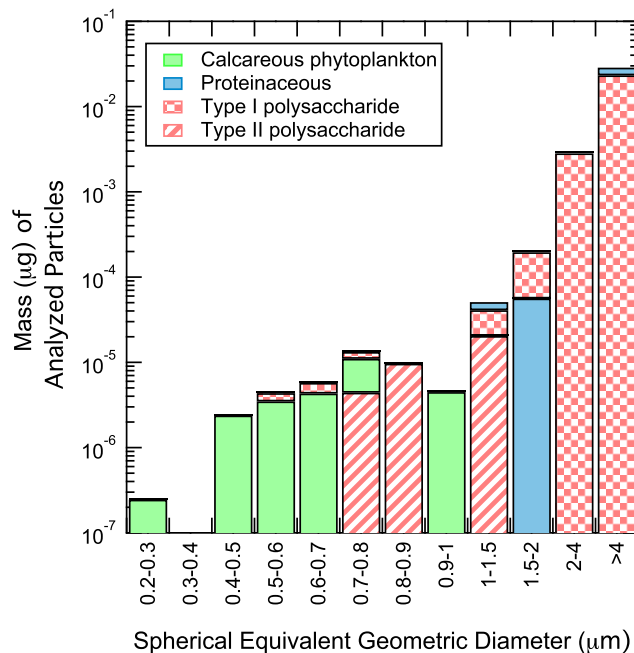
Figure 5.7: Estimated mass of marine particle types from both Arctic and Pacific samples.

if mixed with gel-like organic material concentrated in the surface microlayer, are extremely difficult to identify based solely on morphology. SEM coupled with EDX can confirm the presence of C, O, and nutrient-affiliated elements like N, and P but cannot provide the chemical specificity needed to identify the components of intact cell walls, chloroplasts, or other organelles. For this, x-ray spectromicroscopy is well-suited (Lawrence et al., 2003; Brandes et al., 2004). Using STXM-NEXAFS we have identified submicron fragments of calcareous phytoplankton (coccolithophores) previously suggested to contribute significant quantities of nss-Ca in MBL aerosol (Sievering et al., 2004). The unique signature of $CaCO_3$ couple with straight-chain alkane groups in the average spectra was combined with sub-particle resolution spectra–confirming the uniform distribution of the two components–to support the classification of these particles as biological.

5.4   Conclusion

Ambient sub- and supermicron marine aerosol particles were collected in Pacific and Arctic marine boundary layers and subsequently analyzed using single particle STXM-NEXAFS, revealing four distinct types of marine POA. Although two-thirds of marine particles were characterized as polysaccharides, important differences exist even among those seemingly similar biogenic compounds, including the association with sea salt and the inferred differences in hygroscopicity. We also report evidence of proteinaceous compounds and the first observation of calcifying phytoplankton in marine POA.

In previous chemical characterizations of marine aerosol, most observations of marine POA show either hydrophobic, polysaccharide-like material or morphologically distinct micro-organisms (i.e. bacteria and diatoms). The particles presented here, while consistent with those observations, provide a more detailed, chemically specific picture of marine aerosol that resolves some of the uncertainties associated with previous observations. These observations also confirm that multiple, distinct types of marine particles are emitted to the atmosphere as external mixtures.

5.5   Acknowledgments

Table 5.1: X-ray spectra carbon K-edge, near-edge, and post-edge features

Component	Transition	Energy (eV)
Aromatic/alkene, R(C = C)R'	C 1s-$\pi^*_{C=C}$	285 ± 0.2^a
Ketone, R(C = O)R'	C 1s-$\pi^*_{C=O}$	286.7 ± 0.2^a
Alkyl, R(C-H)$_n$R'	C 1s-$\pi^*_{C=H}$	287.7 ± 0.7^a
Amide carbonyl, R-NH(C = O)R'	C 1s-$\pi^*_{C=O}$	288.3 ± 0.2^b
Carboxylic carbonyl, R(C = O)OH	C 1s-$\pi^*_{C=O}$	288.7 ± 0.3^a
Alcohol, R-COH	C 1s-3p/σ^*_{C-OH}	289.5 ± 0.3^b
Inorganic carbonate, CO_3^{2-}	C 1s-$\pi^*_{C=O}$	290.4 ± 0.2^a
Alkyl, R(C-H)$_n$R'	C 1s-σ^*_{C-C}	292 ± 0.5^c
Potassium, K	$L_{2,3}$ edges	297.4 ± 0.2 and 299 ± 0.2^a

[a]Russell et al. (2002), [b]Solomon et al. (2009), [c]Myneni (2002)

Table 5.2: Summary of observed marine particle types in southeast Pacific and Arctic samples.

	No. of Marine Particles	
Type	Pacific	Arctic
Polysaccharide		
with carboxylic acid (PsI)	0	43
without carboxylic acid (PsII)	7	0
Protein	2	4
Phytoplankton	19	0
Total	28	47

Table 5.3: Observed types of marine primary organic aerosol and the suggested biological relevance of specific particle types.

Location	Method(s)	Particle Size	Dominant Component(s) or Spectral Feature	Biological Relevance
Polysaccharides				
Arctic[a]	TEM,	< 100 nm	Colloidal spherules	EPS gels
Various[b]	TEM, X-ray backscatter, and solubility	< 1 μm	Colloidal spherules	EPS gels
Mediterranean Sea and Long Island Sound[c]	Alcian blue dye	1-50 μm	Semi-transparent colloids	Polysaccharides
W. Pacific[d]	TEM, SEM with X-ray backscatter, and solubility	< 50 nm	Colloidal spherules	EPS gels
North Atlantic[e,*]	HNMR (WSOC and WIOC)	60-1000 nm	Hydroxylate aliphatics Lipid-like aliphatics	Lipopolysaccharides
Arctic[f]	FTIR spectroscopy	< 1 μm	Organic hydroxyl groups Alkane groups	Polysaccharides
SE Pacific[g]	FTIR spectroscopy	< 1 μm	Organic hydroxyl groups	Polysaccharides
SE Pacific[h]	STXM-NEXAFS	< 1 μm	Organic hydroxyl groups	Polysaccharides
Arctic[h]	STXM-NEXAFS	> 1 μm	Carboxylic acid groups	Polysaccharides

*HNMR characterized aerosol was generated in a laboratory setting from collected seawater.

[a]Leck and Bigg (2005a), [b]Leck and Bigg (2005b), [c]Kuznetsova et al. (2005), [d]Leck and Bigg (2008), [e]Facchini et al. (2008), [f]Russell et al. (2010b), [g]Hawkins et al. (2010), [h]This work, [i]Leck and Bigg (1999), [j]Middlebrook et al. (1998), [k]Bigg and Leek (2001), [l]Cavalli et al. (2004)

Table 5.3: cont'd

Location	Method(s)	Particle Size	Dominant Component(s) or Spectral Feature	Biological Relevance
Protein and amino acid compounds				
Arctic[i]	TEM and Extraction	> 50 nm	Hydrophobic organic aggregates	Amino acids
Mediterranean Sea and Long Island Sound[c]	HPLC and Coomassie Blue dye	not provided	Asp, Glu, Ser, Ala	Amino acids
		1-50 μm	Semi-transparent colloids	Proteins
Arctic[h]	STXM-NEXAFS	> 1 μm	Alkane and amide groups	Protein
SE Pacific[h]	STXM-NEXAFS	> 1 μm	Alkane and amide groups	Protein

*HNMR characterized aerosol was generated in a laboratory setting from collected seawater.

[a]Leck and Bigg (2005a), [b]Leck and Bigg (2005b), [c]Kuznetsova et al. (2005), [d]Leck and Bigg (2008), [e]Facchini et al. (2008), [f]Russell et al. (2010b), [g]Hawkins et al. (2010), [h]This work, [i]Leck and Bigg (1999), [j]Middlebrook et al. (1998), [k]Bigg and Leek (2001), [l]Cavalli et al. (2004)

Table 5.3: cont'd

Location	Method(s)	Particle Size	Dominant Component(s) or Spectral Feature	Biological Relevance
		Micro-organisms and their fragments		
Arctic[i]	TEM and Extraction	400 nm		Bacteria and diatoms
Arctic[a]	TEM, X-ray backscatter, and solubility	200-5000 nm		Micro-organisms and fragments
W. Pacific[d]	TEM, SEM with X-ray backscatter, and solubility	> 400 nm, 3.7 to 7.5 μm	$CaCO_3$	Coral-related Bacteria
SE Pacific[h]	STXM-NEXAFS	< 1 μm	$CaCO_3$ and alkane groups	Calcareous phytoplankton fragments
		None listed		
Tasmania[j]	PALMS	> 160 nm	Organic mass fragments	
Arctic[k]	TEM	> 100 nm	Organic liquid	Proteins
Ireland[l]	IC, EGA, HNMR, and TOC	< 1.5 μm	WIOC (not characterized) WSOC (aliphatic groups near heteroatoms, HULIS, and partially oxidized species)	

*HNMR characterized aerosol was generated in a laboratory setting from collected seawater.

[a]Leck and Bigg (2005a), [b]Leck and Bigg (2005b), [c]Kuznetsova et al. (2005), [d]Leck and Bigg (2008), [e]Facchini et al. (2008), [f]Russell et al. (2010b), [g]Hawkins et al. (2010), [h]This work, [i]Leck and Bigg (1999), [j]Middlebrook et al. (1998), [k]Bigg and Leek (2001), [l]Cavalli et al. (2004)

References

Aller, J. Y., Kuznetsova, M. R., Jahns, C. J., Kemp, P. F., 2005. The sea surface microlayer as a source of viral and bacterial enrichment in marine aerosols. Journal of Aerosol Science 36 (5-6), 801–812.

Aluwihare, L. I., Repeta, D. J., Chen, R. F., 1997. A major biopolymeric component to dissolved organic carbon in surface sea water. Nature 387 (6629), 166–169.

Bates, T. S., Quinn, P. K., Coffman, D., Schulz, K., Covert, D. S., Johnson, J. E., Williams, E. J., Lerner, B. M., Angevine, W. M., Tucker, S. C., et al., 2008. Boundary layer aerosol chemistry during TexAQS/GoMACCS 2006: Insights into aerosol sources and transformation processes. Journal of Geophysical Research 113, doi:10.1029/2008JD010023.

Beaufort, L., Couapel, M., Buchet, N., Claustre, H., Goyet, C., 2008. Calcite production by coccolithophores in the south east Pacific Ocean. Biogeosciences 5 (4), 1101–1117.

Benner, R., Kaiser, K., 2003. Abundance of amino sugars and peptidoglycan in marine particulate and dissolved organic matter. Limnology and Oceanography 48 (1), 118–128.

Bigg, E., Leek, C., 2001. Properties of the aerosol over the central Arctic Ocean. Journal of Geophysical Research-Atmospheres 106 (D23), 32,101–32,109.

Blanchard, D., 1964. Sea-to-Air Transport of Surface Active Material. Science 146 (3642), 396.

Brandes, J. A., Lee, C., Wakeham, S., Peterson, M., Jacobsen, C., Wirick, S., Cody, G., 2004. Examining marine particulate organic matter at sub-micron scales using scanning transmission X-ray microscopy and carbon X-ray absorption near edge structure spectroscopy. Marine Chemistry 92 (1-4), 107–121.

Cavalli, F., Facchini, M. C., Decesari, S., Mircea, M., Emblico, L., Fuzzi, S., Ceburnis, D., Yoon, Y. J., ODowd, C. D., Putaud, J. P., et al., 2004. Advances in characterization of size-resolved organic matter in marine aerosol over the North Atlantic. Journal of Geophysical Research 109, 1–14.

Clarke, A. D., Owens, S. R., Zhou, J., 2006. An ultrafine sea-salt flux from breaking waves: Implications for cloud condensation nuclei in the remote marine atmosphere. J. Geophys. Res 111, 1–2.

Crahan, K., Hegg, D., Covert, D., Jonsson, H., Reid, J., Khelif, D., Brooks, B., 2004. Speciation of organic aerosols in the tropical mid-Pacific and their relationship to light scattering. Journal of the Atmospheric Sciences 61 (21), 2544–2558.

Facchini, M. C., Rinaldi, M., Decesari, S., Carbone, C., Finessi, E., Mircea, M., Fuzzi, S., Ceburnis, D., Flanagan, R., Nilsson, E. D., et al., 2008. Primary submicron marine aerosol dominated by insoluble organic colloids and aggregates. Geophysical Research Letters 35 (17), doi:10.1029/2008GL034210.

Gagosian, R. B., Zafiriou, O. C., Peltzer, E. T., Alford, J. B., 1982. Lipids in aerosols from the tropical North Pacific- Temporal variability. Journal of Geophysical Research 87, 11133–11144.

Godoi, R. H. M., Aerts, K., Harlay, J., Kaegi, R., Ro, C. U., Chou, L., Van Grieken, R., 2009. Organic surface coating on Coccolithophores-Emiliania huxleyi: Its determination and implication in the marine carbon cycle. Microchemical Journal 91 (2), 266–271.

Hawkins, L. N., Russell, L. M., Covert, D. S., Quinn, P. K., Bates, T. S., 2010. Carboxylic Acids, Sulfates, and Organosulfates in Processed Continental Organic Aerosol over the Southeast Pacific Ocean during VOCALS-REx 2008. Journal of Geophysical Research in press., doi:10.1029/2009JD013276.

Henrichs, S. M., Williams, P. M., 1985. Dissolved and particulate amino acids and carbohydrates in the sea surface microlayer. Marine chemistry 17 (2), 141–163.

Hoffman, E. J., Duce, R. A., 1976. Factors influencing the organic carbon content of marine aerosols: A laboratory study. Journal of Geophysical Research 81 (21), 3667–3670.

Ito, A., Kawamiya, M., 2010. Potential impact of ocean ecosystem changes due to global warming on marine organic carbon aerosols. Global Biogeochemical Cycles 24, doi:10.1029/2009GB003559.

Jordan, R. W., Kleijne, A., 1994. A classification system for living coccolithophores. Coccolithophores. Cambridge University Press, Cambridge, 83–105.

Kanakidou, M., Seinfeld, J. H., Pandis, S. N., Barnes, I., Dentener, F., Facchini, M. C., Van Dingenen, R., Ervens, B., Nenes, A., Nielsen, C. J., et al., 2005. Organic aerosol and global climate modelling: a review. Atmospheric Chemistry and Physics 5 (4), 1053–1123.

Kuznetsova, M., Lee, C., Aller, J., 2005. Characterization of the proteinaceous matter in marine aerosols. Marine Chemistry 96 (3-4), 359–377.

Kuznetsova, M. R., Lee, C., 2002. Dissolved free and combined amino acids in nearshore seawater, sea surface microlayers and foams: Influence of extracellular hydrolysis. Aquatic Sciences-Research Across Boundaries 64 (3), 252–268.

Larsson, K., Odham, G., Södergren, A., 1974. On lipid surface films on the Sea. 1. A simple method for sampling andstudies of composition. Marine Chemistry 2 (1), 49–57.

Lawrence, J. R., Swerhone, G. D. W., Leppard, G. G., Araki, T., Zhang, X., West, M. M., Hitchcock, A. P., 2003. Scanning transmission X-ray, laser scanning, and transmission electron microscopy mapping of the exopolymeric matrix of microbial biofilms. Applied and Environmental Microbiology 69 (9), 5543.

Leck, C., Bigg, E., 2008. Comparison of sources and nature of the tropical aerosol with the summer high Arctic aerosol. Tellus. Series B, Chemical and Physical Meteorology 60 (1), 118–126.

Leck, C., Bigg, E. K., 1999. Aerosol production over remote marine areas-A new route. Geophysical Research Letters 26, 3577–3580.

Leck, C., Bigg, E. K., 2005a. Biogenic particles in the surface microlayer and overlaying atmosphere in the central Arctic Ocean during summer. Tellus B 57 (4), 305–316.

Leck, C., Bigg, E. K., 2005b. Source and evolution of the marine aerosolA new perspective. Geophysical Research Letters 32 (19), doi:10.1029/2005GL023651.

Liu, S., Day, D. A., Russell, L. M., 2010. Afternoon Increase of Oxygenated Organic Functional Groups at a Coastal Site in Southern California. *submitted*.

Middlebrook, A. M., Murphy, D. M., Thomson, D. S., 1998. Observations of organic material in individual marine particles at Cape Grim during the First Aerosol Characterization Experiment (ACE 1). Journal of Geophysical Research 103, 16475–16484.

Murphy, D. M., Anderson, J. R., Quinn, P. K., McInnes, L. M., Brechtel, F. J., Kreidenweis, S. M., Middlebrook, A. M., Posfai, M., Thomson, D. S., Buseck, P. R., 1998. Influence of sea-salt on aerosol radiative properties in the Southern Ocean marine boundary layer. Nature 392 (6671), 62–65.

Myneni, S. C. B., 2002. Soft X-ray spectroscopy and spectromicroscopy studies of organic molecules in the environment. Reviews in Mineralogy and Geochemistry 49 (1), 485.

Quinn, P. K., Coffman, D. J., Kapustin, V. N., Bates, T. S., Covert, D. S., 1998. Aerosol optical properties in the marine boundary layer during the First Aerosol Characterization Experiment(ACE 1) and the underlying chemical and physical aerosol properties. Journal of Geophysical Research 103, 16.

Russell, L. M., Bahadur, R., Ziemann, P. J., 2010a. Reframing the Organic Aerosol Debate by Reconciling Functional Group Composition in Chamber and Atmospheric Particles. submitted.

Russell, L. M., Hawkins, L. N., Frossard, A. A., Quinn, P. K., Bates, T. S., 2010b. Carbohydrate-Like Composition of Submicron Atmospheric Particles and their Production from Ocean Bubble Bursting. Proceedings of the National Academy of Sciences, doi:10.1073/pnas.0908905107.

Russell, L. M., Maria, S. F., Myneni, S. C. B., 2002. Mapping organic coatings on atmospheric particles. Geophysical Research Letters 29 (16), 26–1.

Sawada, K., Shiraiwa, Y., 2004. Alkenone and alkenoic acid compositions of the membrane fractions of Emiliania huxleyi. Phytochemistry 65 (9), 1299–1307.

Sievering, H., Cainey, J., Harvey, M., McGregor, J., Nichol, S., Quinn, P., 2004. Aerosol non-sea-salt sulfate in the remote marine boundary layer under clear-sky and normal cloudiness conditions: Ocean-derived biogenic alkalinity enhances sea-salt sulfate production by ozone oxidation. Journal of Geophysical Research 109 (D18), 19317.

Solomon, D., Lehmann, J., Kinyangi, J., Liang, B., Heymann, K., Dathe, L., Hanley, K., Wirick, S., Jacobsen, C., 2009. Carbon (1s) NEXAFS Spectroscopy of Biogeochemically Relevant Reference Organic Compounds. Soil Science Society of America Journal 73 (6), 1817.

Sullivan, R. C., Prather, K. A., 2007. Investigations of the diurnal cycle and mixing state of oxalic acid in individual particles in Asian aerosol outflow. Environmental Science Technology 41 (23), 8062–8069.

Takahama, S., Gilardoni, S., Russell, L. M., Kilcoyne, A. L. D., 2007. Classification of multiple types of organic carbon composition in atmospheric particles by scanning transmission X-ray microscopy analysis. Atmospheric Environment 41 (40), 9435–9451.

Takahama, S., Liu, S., Russell, L. M., 2010. Coatings and clusters of carboxylic acids in carbon-containing atmospheric particles from spectromicroscopy and their implications for cloud-nucleating and optical properties. Journal of Geophysical Research 115 (D1), D01202.

Van Den Hoek, C., 1982. Phytogeographic distribution groups of benthic marine algae in the North Atlantic Ocean. A review of experimental evidence from life history studies. Helgoland Marine Research 35 (2), 153–214.

Wood, R., Bretherton, C., Huebert, B., Mechoso, C. R., Weller, R., 2006. VOCALS-SouthEast Pacific Regional Experiment (REx). *Scientific program overview* http://www.usclivar.org/science_status/VOCALS_SPO_Revised_Complete.pdf.

Zhang, Q., Jimenez, J. L., Canagaratna, M. R., Allan, J. D., Coe, H., Ulbrich, I., Alfarra, M. R., Takami, A., Middlebrook, A. M., Sun, Y. L., et al., 2007. Ubiquity and dominance of oxygenated species in organic aerosols in anthropogenically-influenced Northern Hemisphere midlatitudes. Geophysical Research Letters 34, doi:10.1029/2007GL029979.

Conclusion

Atmospheric aerosol particles collected over three field studies and including natural and anthropogenic emissions were characterized for organic composition and accompanying inorganic components. Factor analyses allowed mixtures of multiple types of organic components to be separated and compared across multiple locations. Observed organic components included fossil fuel combustion (fresh and processed), biomass burning, and primary marine biogenic emissions. In-cloud particles in the California marine boundary layer were internal mixtures of soluble inorganic and organic components and showed consistent droplet scavenging across all measured components. Near-shore measurements of aged biomass burning particles and transported diesel emissions illustrated the important role of large wildfires in generating organic aerosol and allowed investigation of the role of photochemistry in changing the organic composition. Carboxylic acid groups showed an increased contribution to OM in smoke particles aged more than 4 days in the atmosphere, whereas ketone groups, commonly observed in chamber studies of biogenic SOA, decreased from 2-day to 4-day aged particles. Some of the signatures of primary and secondary organic components were resolved in smoke particle measurements and were observed to change over time, illustrating the chemical complexity of aging and dilution associated with large biomass burning plumes. Processed particles transported from South America to the southeastern Pacific marine boundary layer were internal mixtures of mineral dust and organic components, while sulfate remained mostly in separate particles. Mass concentrations of components associated with anthropogenic emissions were correlated to radon concentrations and were greatest close to the coast, addressing one of the main hypotheses of the VOCALS-REx study regarding the cause of the elevated

droplet number concentrations near shore. This result indicates that multiple types of particles with different hygroscopic properties could contribute to the enhancement in cloud droplet number near the South American shore. Finally, detailed measurements at single-particle resolution revealed four distinct types of marine primary organic aerosol with quite different morphologies and composition. The four marine POA types were consistent with many previous observations of marine particles, but were characterized in greater detail with respect to their organic composition. In this way, even components as prevalent as polysaccharides were shown to comprise multiple types of compounds with varied hygroscopicity. The measurements presented here contribute to a better characterization of organic aerosol composition in the eastern Pacific marine boundary layer, and can provide a better constraint on modeling aerosol-cloud interactions in this climatically-relevant region.

Several future projects using these measurements would add to the understanding of organic-containing particles as CCN. One study that would address the questions raised by this work would be to quantify types of primary marine particles at the Scripps pier. A coastal (permanent) site such as this has the added benefit of being in close proximity to sporadic phytoplankton blooms of a variety of species. Sea spray particles from such blooms would be more similar to particles characterized in the northeast Atlantic than to particles collected in the southeastern Pacific (during lower biological activity). These bloom particles would provide a more direct chemical comparison to the marine POA during blooms from the Atlantic. Targeting periods of low particle concentration and on-shore flow, the influence of local and regional pollution could be reduced. Single particle spectromicroscopy of marine POA during background and bloom conditions might reveal important differences in the organic composition (e.g. solubility) and organic mass-to-salt ratio, which may be relevant for models that are currently using bloom conditions to parameterize the marine OC flux to the atmosphere. Given that phytoplankton blooms do not reach global scale and do not persist year-round, it may be important to know if the organic fraction is sufficiently different during those times so more accurate conditions can be included in marine

particle emission models.